Computational Studies on Sulfur Chemistry

By

VOLGA KOJASOY
DISSERTATION

Submitted in partial satisfaction of the requirements for the degree of

DOCTOR OF PHILOSOPHY

in

Chemistry and Chemical Biology

in the

OFFICE OF GRADUATE STUDIES

of the

UNIVERSITY OF CALIFORNIA

DAVIS

Approved:

Dean J. Tantillo, Chair

Lee-Ping Wang

Alexei A. Stuchebrukhov

Committee in Charge

2023

Dedicated to my beloved family members (Ipek, Simo, Cici, and Fugen)

and

my fiancé Burak

for their endless love, support, and encouragement.

CONTENTS

ABSTRACT

This dissertation covers a range of computational studies on noncovalent interactions in biological systems and mechanistic investigations of synthetically and biosynthetically relevant reactions. Chapter 1 introduces the main concepts (i.e., basics of quantum mechanics, analysis of noncovalent interactions and modeling organic reactions) behind quantum chemical calculations discussed (in the order they appear) in this report.

Chapter 2 details the roles of noncovalent interactions involving sulfur atoms in biological systems, where computational approaches for modelling noncovalent interactions were described and examples of their applications were provided.

Chapter 3 homes elucidation of organic reaction mechanisms involving sulfur atoms: (1) a collaborative effort with the research groups of Prof. John P. Toscano, Prof. Adrian J. Hobbs, and Prof. Jon M. Fukuto which explored the reaction mechanism of hydropersulfides with S-nitrosothiols, and revealed that S-nitrosothiols can be degraded by hydropersulfides to release nitric oxide which results in the regulation of vascular tone; (2) mechanistic investigation of the formation of zwiebelanes which are bioactive natural products isolated from onion extracts (ongoing).

Chapter 4 details a collaboration with Prof. Uttam K. Tambar's group. Our study discussed the catalyst-controlled regiodivergence in rearrangements of indole-based onium ylides and the mechanistic investigation of rhodium- and copper-catalyzed reactions showed divergent pathways favoring [2,3]-rearrangement involving a metal-free ylide and [1,2]-rearrangement involving a metal-coordinated ion pair in a solvent-cage.

Lastly, Chapter 5 of this dissertation (in collaboration with the groups of Prof. Ikuro Abe, Prof. John A. Porco Jr., and Prof. Makoto Fujita) focuses on the evaluation of the potential of meroterpenoid cyclases to expand the chemical space of fungal meroterpenoids. Our study shed light on their catalytic activity and could pave the way to create unnatural pathways towards second generation meroterpenoids.

PUBLICATIONS

(1) Kojasoy, V.; Tantillo, D. J. Importance of Noncovalent Interactions Involving Sulfur Atoms in Thiopeptide Antibiotics–Glycothiohexide α and Nocathiacin I. *J. Phys. Chem. A* **2023**, *127*, 2081–2090.

(2) Li, Z.; Xu, B.; **Kojasoy, V.**; Ortega, T.; Adpressa, D. A.; Ning, W.; Wei, X.; Liu, J.; Tantillo, D. J.; Loesgen, S.; Rudolf, J. D. First trans-Eunicellane Terpene Synthase in Bacteria. *Chem* **2023**, *9*, 1-11.

(3) Kojasoy, V.; Tantillo, D. J. Impacts of Noncovalent Interactions Involving Sulfur Atoms on Protein Stability, Structure, Folding, and Bioactivity. *Org. Biomol. Chem.* **2023**, *21*, 11–23.

(4) Zarenkiewicz, J.[#]; Perez-Ternero, C.[#]; **Kojasoy, V.[#]**; McGinty, C.; Khodade, V. S.; Lin, J.; Tantillo, D. J.; Toscano, J. P.; Hobbs, A. J.; Fukuto, J. M. The Reaction of Hydropersulfides (RSSH) with S-Nitrosothiols (RS-NO) and the Biological/Physiological Implications. *Free Radic. Biol. Med.* **2022**, *188*, 459-467 ([#] equal contribution).

(5) Nair, V. N.; **Kojasoy, V.**; Laconsay, C. J.; Kong, W.; Tantillo, D. J.; Tambar, U. K. Catalyst-Controlled Regiodivergence in Rearrangements of Indole-Based Onium Ylides. *J. Am. Chem. Soc.* **2021**, *143*, 9016-9025.

(6) Mitsuhashi, T. [#]; Barra, L. [#]; Powers, Z. [#]; **Kojasoy, V.[#]**; Cheng, A.; Yang, F.; Taniguchi, Y.; Kikuchi, T.; Fujita, M.; Tantillo, D. J.; Porco, J. A., Jr.; Abe, I. Exploiting the Potential of Meroterpenoid Cyclases to Expand the Chemical Space of Fungal Meroterpenoids. *Angew. Chem. Int. Ed.* **2020**, *59*, 23772-23781 ([#] equal contribution).

(7) Kocasoy, V.; Dedeoglu, B.; Demir-Ordu, O.; Aviyente, V. Influence of Odd‑Even Effect and Intermolecular Interactions in 2D Molecular Layers of Bisamide Organogelators. *RSC Adv.* **2018**, *8*, 35195-35204.

ACKNOWLEDGEMENTS

I will forever be grateful to my family, friends, and advisors for supporting me throughout graduate school. Without them, I could not have undertaken this journey.

I would like to start by expressing my deepest gratitude to my Ph.D. advisor, Dean J. Tantillo, for being the best advisor I could have imagined. Thank you, Dean, for inspiring me to explore the science I am passionate about. I am grateful for what you have taught me over the past 5 years. I could not have made it this far without your continuous support and guidance.

I would like to extend my sincere thanks to my dissertation committee members Lee-Ping Wang and Alexei Stuchebrukhov. Thank you, Lee-Ping and Alexei for always being kind and supportive throughout the years. I appreciate your helpful feedback regarding my research and your willingness to teach me.

Many thanks to my collaborators whom I had the pleasure to work with: Prof. Uttam K. Tambar (University of Texas Southwestern Medical Center), Prof. John A. Porco, Jr. (Boston University), Prof. Ikuro Abe (The University of Tokyo), Prof. Jon M. Fukuto (Sonoma State University), Prof. John P. Toscano (John Hopkins University), Prof. Adrian J. Hobbs (The William Harvey Research Institute), Prof. Jeffrey D. Rudolf (University of Florida), Prof. Daniel Romo (Baylor University), Prof. Tobias Dick (The German Cancer Research Center-Heidelberg), and Prof. David E. Olson (UC Davis). And I would like to thank all members of the Tantillo group for their support and friendship. Special thanks to Dr. Croix J. Laconsay, Wang Yeuk Kong, Jesi Lee, Teresa Ortega, Wentao Guo, and Zhitao Feng for their collaborations and helpful discussions.

Finally, I am deeply indebted to my entire family for supporting me throughout my life and always encouraging me to follow my dreams. I have so much love for all of you. And my fiancé Burak, thank you for standing by me through it all. None of this would have been possible without your love and support. Thank you.

Chapter 1. Modern Applied Quantum Chemistry

1.1 Introduction to Quantum Mechanics

Computational chemistry is an ever-growing field of chemistry that aims to solve chemical problems by calculations. Given a set of nuclei and electrons, computational chemistry can attempt to simulate chemical reactions at an atomic level and provide useful insights. The predictive power of computational chemistry helps rationalize experimental data and paves the way for new experimental designs. The primary tool used to solve the mechanistic and structural problems described in this dissertation is quantum mechanics. The purpose of quantum mechanics calculations is to study the interactions of nuclei and electrons in particular positions. In the quantum description of the motion of a particle, one describes a system using a wavefunction (Ψ). The energy of a particular arrangement of nuclei and electrons can be calculated by solving the time-independent Schrödinger equation within the Born-Oppenheimer approximation:

$$\mathbf{H\Psi} = E\mathbf{\Psi}$$

In the above equation, the Hamiltonian operator (H) operates on Ψ to generate the associated energy (E) of a particular arrangement of nuclei and electrons. The Born-Oppenheimer approximation separates the motion of nuclei and electrons based on the fact that nuclei are much heavier than electrons. Hence, the electronic part of the Schrödinger equation is solved in the field of fixed nuclei and the resulting potential energy surface (PES) accounts for the nuclear motion.

The Schrödinger equation can only be solved exactly for the simplest of systems (i.e., the hydrogen atom). Methods "intend" to solve the Schrödinger equation for many-electron systems are broadly referred to as electronic structure calculations. The commonly used electronic structure methodologies for studying organic systems are based on either *ab initio* wavefunction-based approaches or density functional theory (DFT). Whereas the wavefunction-based methods (such as Hartree-Fock) depend on the wavefunction, DFT (such as Kohn-Sham DFT[1]) is based on electron density.

In the Hartree-Fock theory, each electron is described by an orbital and the wavefunction is constructed by the arrangement of the *best* set of orbitals that give the lowest energy (by the variational principle) in a single Slater determinant. The motion of the single electron is independent of all other electrons (i.e., the electron-electron interactions are taken into account in an average fashion) and therefore, the correlation between electrons is neglected. Hartree-Fock model can be systematically improved by adding more determinants and additional approximations (post-Hartree-Fock methods) which may bring along an increase in computational cost.

DFT is considered as an advancement on the Hartree-Fock theory by including an approximate treatment of electron correlation and often giving the best compromise between the computational cost and accuracy in relative energies (chemical accuracy $\leq$ 1 kcal mol^{-1}). The most popular DFT approach −Kohn-Sham DFT− calculates the kinetic energy as a function of density by assuming that the density corresponds to a wavefunction that consists of a single Slater determinant (just like Hartree-Fock theory). The mathematical equations are similar to Hartree-Fock except for the additional exchange correlation term in the Kohn-Sham DFT. The cost benefit of DFT outweighs the post-Hartree-Fock methods such as configuration interaction (CI), coupled cluster (CC) etc. Nevertheless, one can always use these high level post-Hartree-Fock methods for single point calculations in which the energies are recalculated for given geometries. Overall, DFT is good at predicting geometries but often not as good for predicting energies. The main pitfall of DFT is that the results can't be systematically improved towards the exact solution. To this end, benchmark studies against higher levels of theories could be conducted for the selection of the reliable DFT method that accurately simulates the experimental data. In this dissertation, DFT is the method of choice for modeling organic reaction mechanisms at reconciled computational cost and accuracy.

1.2 Noncovalent Interactions Analysis (NCI) and Applications in Biological Systems

Noncovalent interactions such as electrostatic interactions, van der Waals interactions, π-π interactions and hydrophobic interactions are ubiquitous in Nature and critical for the function of biological systems.[23] In general, intra- and intermolecular noncovalent interactions are considered weak compared to regular

covalent bonds and contribute only a few kcal mol^{-1}. Nevertheless, these seemingly weak interactions cooperatively play fundamental roles in molecular recognition.[4,5]

Understanding the nature and magnitude of noncovalent interactions is important for the design and synthesis of future drugs and materials. Modern computational chemistry offers various techniques for the analysis of noncovalent interactions. Note that each technique will have its own limitations and choosing the appropriate approach highly depends on the system size and whether the interaction of interest is intra- or intermolecular. After obtaining a valid geometry, pairwise interactions between the two non-bonded fragments can be characterized and visualized through reduced density gradient isosurfaces[6–8] and the stabilization energies can be calculated (and decomposed) into physical energy components.[9–12] An overview of the commonly used approaches for noncovalent interactions analysis is provided in Chapter 2.

Sulfur atoms are highly polarizable atoms with filled 3p and empty 3d orbitals which can participate in many types of noncovalent interactions. Often, however, they do not receive the same attention as oxygen and nitrogen. Chapter 2 of this dissertation focuses on the significance of noncovalent interactions involving specifically sulfur atoms in biological systems and provides representative examples of the applications of the analysis methods.

1.3 Modeling Organic Reactions

Mechanistic modeling of an organic reaction often starts with the thought process of possible pathways that transform a reactant to a product. Some of these possibilities may be eliminated by experimental evidence (if exist). For each of the remaining ones, the energies of the stationary points (reactants, transition state structures (TSSs), intermediates and products) on the multidimensional potential energy surface (PES) need to be calculated to find the *most likely* reaction mechanism that aligns with experimental observations.

Geometry optimization of the structures along the reaction path is necessary to obtain the stationary points in which the bonds, angles and torsional angles are all at their best possible positions. Whereas a reactant, an intermediate, or a product optimizes to a minimum on the PES (zero potential energy gradient

in all directions) a transition state structure (TSS) optimizes to a first-order saddle point (zero potential energy gradient in all directions except a maximum in one direction). Intrinsic reaction coordinate (IRC) is defined as the minimum energy reaction path in the mass-weighted coordinates on a PES.[13] IRC analysis is the standard method to verify that the first-order saddle point (i.e., TSS) interconnects the reactant (or intermediate) and the product (or intermediate).

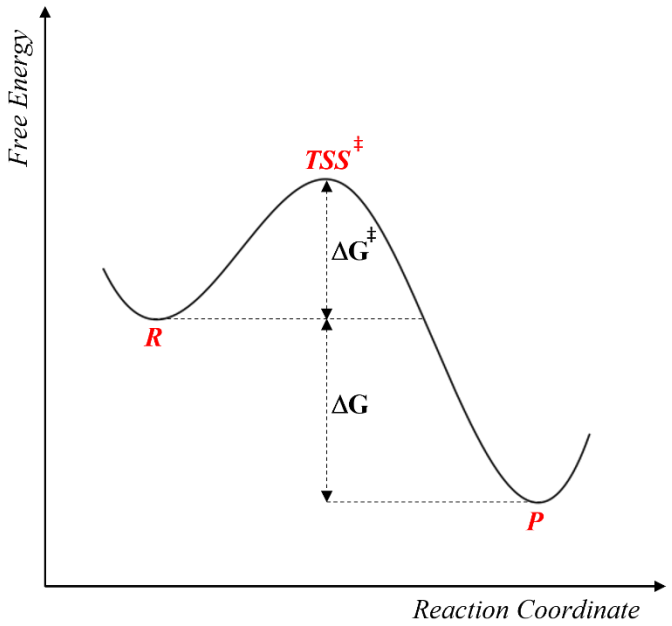

Figure 1.1. Free energy profile along the reaction coordinate (R: reactants, TSS: transition state structure, P: products, $\Delta G^{\ddagger}$: free energy barrier, ΔG: free energy released by the reaction).

According to transition state theory (TST), the free energy barrier of a reaction ($\Delta G^{\ddagger}$ in Figure 1.1) is related to its rate (and the rate constant (k_{rate})) which can be expressed as:

$$k_{\text{rate}} = \kappa \frac{k_B T}{h} e^{-\Delta G^{\ddagger}/RT}$$

This is called the Eyring equation (κ: transmission coefficient; k_B: Boltzmann's constant; T: temperature; h: Planck's constant; $\Delta G^{\ddagger}$: free energy barrier; R: gas constant).[14] In conventional transition state theory, there is a dividing surface that separates reactants from products and it can only be crossed once. Due to

this non-recrossing assumption the rate constant is overestimated. In variational transition state theory (VTST), the rate constant can be variationally optimized by varying the position of the dividing surface until reaching the point at where there is minimum recrossing.[15] This point will correspond to the maximum on the free energy surface known as the variational transition state.

TST works successfully for bimolecular reactions under the assumption that the transition state is in quasi-equilibrium with the reactants. However, this assumption may not apply to gas phase unimolecular reactions. The microcanonical formulation of transition theory in terms of total energy when applied to unimolecular reactions is known as the Rice–Ramsperger–Kassel–Marcus (RRKM)[16,17] theory.[18]

TST and its variants (i.e., VTST, RRKM) are statistical theories that are valid for most organic reactions. However, there are some reactions involving "non-statistical dynamic effects" that cannot be adequately explained by the transition state theory.[19–21] Non-statistical dynamic effects can occur in several scenarios where the assumptions associated with TST cannot be applied. TST assumes that the intramolecular (internal) vibrational energy redistribution (IVR) is significantly fast at a minimum. In reactions having a flat potential energy surface, the timescale of IVR might be comparable or even longer than that for the progression along the reaction coordinate toward product where the selectivity is governed by the momentum. This phenomenon is called "dynamic-matching".[22] Another non-statistical dynamic effect is observed in reactions involving "post-transition state bifurcation (PTSB)" in which a single transition state structure can lead to more than one products without intervening minima.[23,24] Moreover, some recrossing that cannot be treated statistically by VTST also considered as a non-statistical dynamic effect.[25] A common approach for proper description of such effects is performing *ab initio* molecular dynamics (AIMD) simulations.[26] This dissertation provides representative examples of organic reactions that could be modeled by conventional TST (Chapter 3.1, 4 and 5) as well as one that may involve dynamic effects (Chapter 3.2, ongoing).

1.4 References

(1) Kohn, W.; Sham, L. J. Self-Consistent Equations Including Exchange and Correlation Effects. *Phys. Rev.* **1965**, *140*, A1133–A1138.

(2) Schneider, H. J. Noncovalent Interactions: A Brief Account of a Long History. *J. Phys. Org. Chem.* **2022**, *35*, e4340.

(3) Wagner, J. P.; Schreiner, P. R. London Dispersion in Molecular Chemistry - Reconsidering Steric Effects. *Angew. Chem. Int. Ed.* **2015**, *54*, 12274–12296.

(4) Persch, E.; Dumele, O.; Diederich, F. Molecular Recognition in Chemical and Biological Systems. *Angew. Chem. Int. Ed.* **2015**, *54*, 3290–3327.

(5) Bissantz, C.; Kuhn, B.; Stahl, M. A Medicinal Chemist's Guide to Molecular Interactions. *J. Med. Chem.* **2010**, *53*, 5061–5084.

(6) Johnson, E. R.; Keinan, S.; Mori-Sánchez, P.; Contreras-García, J.; Cohen, A. J.; Yang, W. Revealing Noncovalent Interactions. *J. Am. Chem. Soc.* **2010**, *132*, 6498–6506.

(7) Laplaza, R.; Peccati, F.; A. Boto, R.; Quan, C.; Carbone, A.; Piquemal, J. P.; Maday, Y.; Contreras-García, J. NCIPLOT and the Analysis of Noncovalent Interactions Using the Reduced Density Gradient. *Wiley Interdiscip. Rev. Comput. Mol. Sci.* **2021**, *11*, e1497.

(8) Contreras-García, J.; Boto, R. A.; Izquierdo-Ruiz, F.; Reva, I.; Woller, T.; Alonso, M. A Benchmark for the Non-Covalent Interaction (NCI) Index Or… Is It Really All in the Geometry? *Theor. Chem. Acc.* **2016**, *135*, 1–14.

(9) Bader, R. F. W. A Quantum Theory of Molecular Structure and Its Applications. *Chem. Rev.* **1991**, *91*, 893–928.

(10) Weinhold, F.; Landis, C. R.; Glendening, E. D. What Is NBO Analysis and How Is It Useful? *Int. Rev. Phys. Chem.* **2016**, *35*, 399–440.

(11) Phipps, M. J. S.; Fox, T.; Tautermann, C. S.; Skylaris, C. K. Energy Decomposition Analysis Approaches and Their Evaluation on Prototypical Protein–Drug Interaction Patterns. *Chem. Soc. Rev.* **2015**, *44*, 3177–3211.

(12) Patkowski, K. Recent Developments in Symmetry-Adapted Perturbation Theory. *Wiley Interdiscip. Rev. Comput. Mol. Sci.* **2020**, *10*, e1452.

(13) Fukui, K. The Path of Chemical Reactions - the IRC Approach. *Acc. Chem. Res.* **1981**, *14*, 363–368.

(14) Eyring, H. The Activated Complex in Chemical Reactions. *J. Chem. Phys.* **1935**, *3*, 107–115.

(15) Truhlar, D. G.; Garrett, B. C. Variational Transition-State Theory. *Acc. Chem. Res.* **1980**, *13*, 440–448.

(16) Rice, O. K.; Ramsperger, H. C. Theories of Unimolecular Gas Reactions at Low Pressures. *J. Am. Chem. Soc.* **1927**, *49*, 1617–1629.

(17) Marcus, R. A. Unimolecular Dissociations and Free Radical Recombination Reactions. *J. Chem. Phys.* **1952**, *20*, 359–364.

(18) Kreevoy, M. M.; Truhlar, D. G. Transition State Theory. In *Investigation of Rates and Mechanisms of Reactions*; Bernasconi, C. F., Ed.; John Wiley & Sons, Inc., 1986; pp 13–95.

(19) Jayee, B.; Hase, W. L. Nonstatistical Reaction Dynamics. *Annu. Rev. Phys. Chem.* **2020**, *71*, 289–313.

(20) Tantillo, D. J. Dynamic Effects on Organic Reactivity—Pathways to (and from) Discomfort. *J. Phys. Org. Chem.* **2021**, *34*, 1-9.

(21) Tantillo, D. J. *Beyond Transition State Theory—Non-Statistical Dynamic Effects for Organic Reactions*, 1st ed.; Elsevier Ltd., 2021.

(22) Carpenter, B. K. Dynamic Behavior of Organic Reactive Intermediates. *Angew. Chem. Int. Ed. Engl.* **1998**, *37*, 3340–3350.

(23) Ess, D. H.; Wheeler, S. E.; Iafe, R. G.; Xu, L.; Çelebi-Ölçüm, N.; Houk, K. N. Bifurcations on Potential Energy Surfaces of Organic Reactions. *Angew. Chem. Int. Ed.* **2008**, *47*, 7592–7601.

(24) Hare, S. R.; Tantillo, D. J. Post-Transition State Bifurcations Gain Momentum-Current State of the

Field. *Pure Appl. Chem.* **2017**, *89*, 679–698.
(25) Ussing, B. R.; Hang, C.; Singleton, D. A. Dynamic Effects on the Periselectivity, Rate, Isotope Effects, and Mechanism of Cycloadditions of Ketenes with Cyclopentadiene. *J. Am. Chem. Soc.* **2006**, *128*, 7594–7607.
(26) Ma, X.; Hase, W. L. Perspective: Chemical Dynamics Simulations of Non-Statistical Reaction Dynamics. *Philos. Trans. R. Soc. A* **2017**, *375*, 20160204.

Chapter 2. Importance of Noncovalent Interactions Involving Sulfur Atoms in Biological Systems

2.1 Impacts of Noncovalent Interactions Involving Sulfur Atoms on Protein Stability, Structure, Folding, and Bioactivity

This chapter is a slightly modified version of the following publication: Kojasoy, V.; Tantillo, D. J. Impacts of Noncovalent Interactions Involving Sulfur Atoms on Protein Stability, Structure, Folding, and Bioactivity. *Org. Biomol. Chem.* **2023**, *21*, 11–23 with permission from the Royal Society of Chemistry.

2.1.1 Abstract

This review discusses the various types of noncovalent interactions in which sulfur atoms participate and their effects on protein stability, structure, folding and bioactivity. Current approaches and recommendations for modelling these noncovalent interactions (in terms of both geometries and interaction energies) are highlighted.

2.1.2 Introduction

How does the presence of sulfur atoms in proteins affect structure, stability, and bioactivity? The conformational stability of a protein is characterized as the free energy change between its folded and unfolded states, which generally amounts to 5–15 kcal mol^{-1}.[1–5] A balance (sometimes compromise) between many individual (but often interdependent) noncovalent interactions generates each unique folded structure.[2,4,6,7] Noncovalent interactions involving sulfur atoms (S), although generally receiving less attention than those involving oxygen and nitrogen, play essential roles in protein structure and, as a result, stability, and function.[8–11]

Many examples of interactions involving sulfur have been shown to have important biological consequences. For example, the attractive electrostatic interaction between sulfur and oxygen atoms in thiazole nucleoside analogues was found to be important for their antitumor activity.[12] Sulfur, being a highly polarizable atom, is able to participate in strong dispersion interactions that allow the sulfur containing

amino acids methionine (Met) and cysteine (Cys) to make large contributions to the overall 3 dimensional structure and function of membrane proteins.[13] While the formation of disulfide bonds between Cys residues is a key means of stabilizing the tertiary structure of a protein, Brandt et al. revealed that the cleavage of disulfide bonds promoted by sulfur–oxygen interactions can play a critical role in receptor activation.[14] It also was suggested that the reduction of disulfide bonds to thiols—a reaction that modifies that types of noncovalent interactions available for the Cys residues involved—impairs the binding affinity of SARS-CoV/CoV-2 spike protein to the angiotensin converting enzyme 2, which is the receptor that enables entering the host cells.[15]

There have been many excellent reviews on the importance of noncovalent interactions in biological systems, for example, those by Diederich,[10,16,17] Meanwell,[18] Stahl,[19] Schreiner,[9] and Raines.[11] Of particular note is Meanwell and co-workers' review on applications of noncovalent interactions involving sulfur in drug design. Here we provide a catalog of types of noncovalent interactions involving sulfur atoms, along with details of from computational studies on their physical nature and examples of their occurrence specifically in proteins. On the basis of this data, we also provide recommendations for computational chemists modelling systems containing such interactions.

2.1.3 Computational approaches for modelling noncovalent interactions

2.1.3.1 Geometries

The initial step of a computational study on noncovalent interactions generally involves determining a reasonable geometry for the system of interest. Strengths of noncovalent interactions, and contributions to these strengths from different physical factors, are geometry (distance, angle, etc.) dependent.[20,21] In general, one is interested in the lowest energy conformer on a multidimensional potential energy surface (PES). While the lowest energy conformers often correspond to bioactive conformers, one should keep in mind that that need not always be the case. There are many conformational sampling algorithms that vary in accuracy and required computational time (cost).[22–29] A systematic search would explore the whole

potential energy surface for each degree of freedom; that completeness comes at a high computational cost, however. In contrast, a knowledge-based approach would be faster, since it would cover only a portion of the conformational space, but if it covers the relevant portion then all is well. Random searches (e.g., Monte Carlo) and simulated annealing (artificially applying a high temperature to get over barriers) can be used to attempt to sample multiple regions of a PES. Molecular dynamics (MD) can be used to sample conformational changes over time. If one is interested in aqueous solution, then implicit or explicit solvent must be included as well. Detailed descriptions of these (and many other) techniques are beyond the scope of this review, but ref. 24–31 provide good starting points for interested readers. Sometimes the validity of a computed structure is assessed through comparison with experimental data (crystallography, NMR, circular dichroism, etc.).[29] However, the limits of these experimental methods should always be kept in mind, e.g., NMR shifts could represent contributions from several interconverting conformers, the geometric parameters obtained from an X-ray crystal structure may be influenced by crystal packing forces, etc.

2.1.3.2 Interaction Energies

Prediction of protein–ligand binding affinity is an indispensable tool in drug discovery.[32–42] Here we are concerned, however, with the strengths of interactions between two protein substructures. Estimating such interaction energies is difficult. Often, what is done is to "cut" the groups of interest out of the protein context to arrive at a complex of two small molecules whose interaction energy can then be evaluated by comparing the energy of the complex with the energy of the two separate molecules. Such an estimate, of course, comes with caveats, the most significant being that the effects of the surrounding protein environment are not taken into account. That is okay, though, if one wishes to assess the inherent strength of an interaction.

2.1.3.3 Origins of Attraction

The 3-dimensional structure of a protein is maintained through the interplay of multiple noncovalent interactions. Here we describe the commonly used theoretical approaches for assessing the origins of attraction (and repulsion) in noncovalent interactions. Note that these tools may provide numbers, but the results should be treated as qualitative in nature, given the issues described below.[32]

Noncovalent interaction (NCI) analysis[33] is a popular method for visualizing the noncovalent interaction regions in molecules. Users can generate color-coded reduced density gradient isosurfaces (NCI plots) in which blue, green and red represent strong attraction, weak (typically, van der Waals) attraction, and strong repulsion, respectively (Figure 2.1.1). For large, complex systems, it is not convenient to use routine NCI analysis. One solution is to apply NCI analysis based on promolecular density in which predetermined electron density of the atoms in their free-states is used. Alternatively, independent gradient model (IGM) analysis based on promolecular density can also be applied to large systems at a reduced computational time and cost.[34] Also, with the IGM method, one can visualize interactions at a specific region of interest rather than visualizing all the interactions present within the system. Program packages such as Multiwfn support these types of wavefunction analysis.[35]

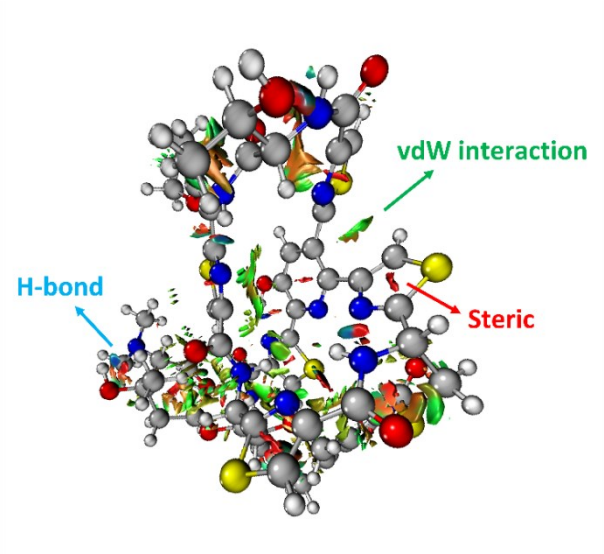

Figure 2.1.1. An NCI plot for glycothiohexide α.[46]

Another approach, the quantum theory of atoms in molecules (QTAIM),[36,37] is used to characterize the properties of chemical bonds via a topological analysis of electron density. In QTAIM, the presence of a bond critical point (BCP) is often used to argue for bonding between atoms. It has been argued that at a BCP, for some cases, the sign of the energy density may correspond to the nature of the bond, positive and negative values representing noncovalent and covalent interactions, respectively.[38] This argument has been extended to a point where a positive value of energy density per unit electron at a BCP (also defined as bond degree) represents a noncovalent bond and hence, a weak interaction.[39] While the exact connections between the quantities computed with QTAIM and the bonding concepts used by organic and bioorganic chemists are still argued about, this tool can still prove useful for comparing interactions to each other.

Natural bond orbital (NBO)[40] calculations allow for the computation of orbital interaction energies between NBOs that correspond to localized (2-center 2-electron, Lewis-like) bonds. Second-order perturbation NBO energies provide estimates of contributions from donor–acceptor (filled-empty) and donor-donor (filled-filled) orbital interactions.

Another approach is energy decomposition analysis (EDA).[41] This widely used tool partitions interaction energies between two moieties into physically meaningful components such as exchange-repulsion, electrostatics, polarization and charge-transfer. Since there are many possible ways of partitioning energy, there exist different types of EDA approaches that can be classified into two main groups: variational and perturbation-based methods. Variational methods such as Kitaura–Morokuma analysis,[42,43] and absolutely localized molecular orbital EDA (ALMO EDA)[44] use intermediate wavefunctions (which provide expression for the monomers) to decompose interaction energy. On the other hand, in perturbation-based methods such as symmetry-adapted perturbation theory (SAPT),[45] the interaction energy is constructed as perturbative corrections to the isolated fragments. We direct our readers to Phipps et al.'s review for detailed descriptions and comments on limitations of the EDA methods used in biomolecular systems.[41]

2.1.4 Noncovalent interactions involving sulfur atoms

We catalogue different types of sulfur noncovalent interactions present in biological systems below. Both experimental and computational studies that address energetic and geometric contributions of sulfur-based noncovalent interactions to stability and bioactivity are reviewed.

2.1.4.1 Hydrogen bonds involving sulfur atoms

Whereas the thioether-containing Met sidechain can accept hydrogen bonds, the thiol-containing Cys can both accept and donate hydrogen bonds.[47] Furthermore, the sulfur atoms in disulfide bonds can form bifurcated hydrogen bonds, i.e., hydrogen bonding motifs that include both sulfur atoms acting as hydrogen bond acceptors.[48,49] While the majority of hydrogen bond lengths observed in proteins range from 2.7 to 3.3 Å,[50] sulfur containing hydrogen bonds are longer compared to hydrogen bonds where oxygen and nitrogen atoms are involved, since sulfur is a highly polarizable atom with a comparatively large atomic radius. In addition, electronegativity is key to the strength of hydrogen bonds, and sulfur is less electronegative (2.58 on the Pauling scale) than oxygen (3.44) and nitrogen (3.04), suggesting that its hydrogens bonds might be weaker. Nonetheless, these weak interactions can be important contributors to the overall shapes of proteins.[51,52]

2.1.4.1.1 S···H–O type hydrogen bonds

The origin of the stability of S···H–O type hydrogen bonds comes, at least in part, from the charge on the acidic hydrogen of the OH group interacting with sulfur.[49] Wennmohs et al. calculated the S···H–O interaction energy (at the coupled cluster level) for the dimethylsulfide–methanol complex, in which dimethylsulfide acts as hydrogen bond acceptor and methanol acts as hydrogen bond donor, to be ∼−5.5 kcal mol^{-1}.[53] NBO analysis suggested that a major source of stabilization was the interaction of the sulfur 3p lone pair and the H–O σ* antibonding orbital.

While O···H–O type hydrogen bonds are generally dominated by electrostatic effects, which are smaller for S···H–O type hydrogen bonds, the contribution of dispersion interactions is larger in S···H–O type hydrogen bonds due to the high polarizability of sulfur.[47,53] Biswal et al. used complexes between thioethers and para-cresol to mimic S···H–O interactions between Met and tyrosine (Tyr). Their experimental and computational results show that O···H–O hydrogen bonding is stronger than that of S···H–O hydrogen bonding, but, for S···H–O interactions, the longer the alkyl chain in the acceptor, stronger the binding of the complex,[47] hinting at effects beyond direct hydrogen bonding. A representative example of an S···H–O type hydrogen bond in a protein, here a Met–Tyr interaction of the type examined by Biswal et al., is shown in Figure 2.1.2.[47,54]

Gregoret et al. surveyed 85 protein structures for hydrogen bonds involving sulfur atoms.[48] They found that hydrogen bonding is not common for Met residues, which could be attributed to the hydrophobic nature of Met. On the other hand, they observed that deprotonated Cys can act as an acceptor of hydrogen bonds from hydroxyl groups. Their study revealed that Cys residues participate in hydrogen bonding more abundantly. Thus, they suggest that Cys's propensity for participating in hydrogen bonding between the thiol group of a Cys (*i*) and the carbonyl oxygen of residue *i*-4 may have a direct influence on helical conformational preferences.[48]

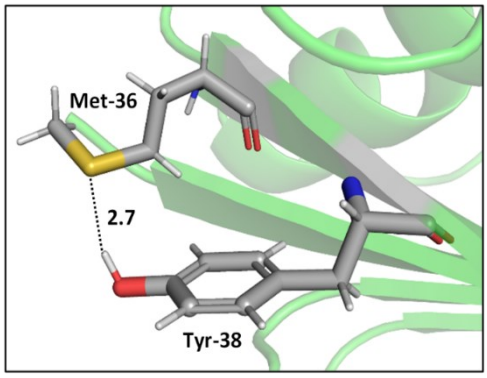

Figure 2.1.2. S···H–O hydrogen bonding interaction between the S of Met-36 and O–H of Tyr-38 (PDB ID: 1A2Z[54]). Distances shown in Å.

In addition, a statistical analysis conducted on >500 protein structures by Zhou et al. suggested that bifurcated hydrogen bonds involving sulfur contacts are prevalent in proteins.[49] For instance, Figure 2.1.3 shows a bifurcated hydrogen bond between two sulfur atoms of a disulfide bond (Cys-58 and Cys-63 residues) acting as acceptors and Thr-339 acting as donor. This interaction unites two α helices.[55]

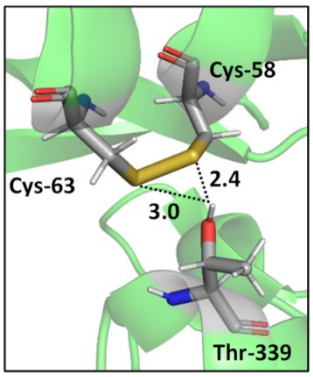

Figure 2.1.3. A bifurcated hydrogen bond formed between the hydroxyl group in Thr-339 and the two sulfur atoms in disulfide bond Cys-58–Cys-63 (PDB ID: 3GRS). Distances shown in Å.[49,55]

2.1.4.1.2 S···H–N type hydrogen bonds

Kjaergaard and coworkers analyzed O···H–N and S···H–N interactions in dimethylamine–dimethyl ether (DMA–DME) and dimethylamine–dimethylsulfide (DMA–DMS) complexes and found that both complexes have similar binding energies.[56] However, based on NCI analyses, the interactions in the DMA–DME complex appeared to be more localized, which was taken as an indication of the larger dispersion interactions in the DMA–DMS complex.[56]

Mons and co-workers reported a combined gas-phase spectroscopy and quantum chemistry study on S···H–N backbone hydrogen bonds in N-acetyl-L-phenylalaninyl-L-methionineamide and N-acetyl-L-methioninyl-L-phenylalanine-amide dipeptides in solvent-free environments created using a supersonic expansion.[57] Both systems showed a local folding of the Met side-chains associated with hydrogen bonds between the sulfur and the neighboring NH(i) or NH(i + 1) amides of the backbone. At 300° K the stability brought by the Met side-chain folding was predicted to be ∼2 kcal mol^{-1} (at the RI-B97-D/QZVPP level).

An example of the local folding of Met residues via hydrogen bonding in the context of a protein is shown in Figure 2.1.4.[58]

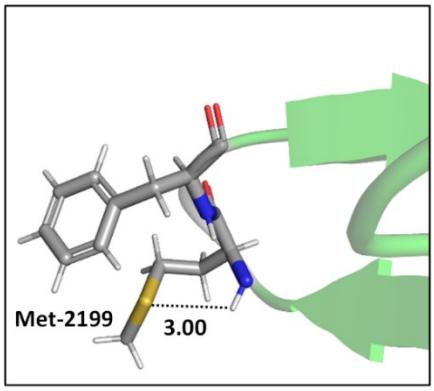

Figure 2.1.4. The local folding of Met-2199 via S···H–N hydrogen bonding interaction (PDB ID: 1D7P[58]). Distances shown in Å.

Lampkin and VanVeller, studied the influence of geometry and dielectric properties on the strength of S···H–N hydrogen bonding in thioamides and showed that hydrogen bonds involving thioamides as hydrogen bond donors range in strength from 1.0–1.5 kcal mol^{-1}.[59] They reported that hydrogen bonding contact angle (Table 2.1.1) is strongly affected by the nature of the hydrogen bond donor and acceptor. For instance, they calculated an optimized hydrogen bonding contact angle of 116° when the thioamide and amide are hydrogen bond donor and acceptor, respectively (Table 2.1.1, entry 2). However, an optimized hydrogen bonding contact angle of 97° was found when the hydrogen bond acceptor and donor are thioamide and amide, respectively (Table 2.1.1, entry 3), which is consistent with the involvement of a σ-hole in the thioamide electrostatic potential map (Table 2.1.1, top right). Overall, they showed that the thioamides act as good hydrogen bond acceptors when the hydrogen bond contact angle is between 90° and 100°, whereas amides can tolerate different angles.[59] The geometry of these hydrogen bonds appears to be determined mainly by dipole–dipole interactions.[60]

Table 2.1.1. Geometry dependence of hydrogen bonding interaction of thioamide and amide isosteres. [a]Numbers in parentheses are the relative energies with respect to entry 1. Interaction energies are calculated at CCSD(T)-SMD/aug-cc-pVDZ//ωB97XD-SMD/aug-cc-pVDZ level of theory. Electrostatic potential maps generated at B3LYP/6-311+g(d,p) with an isovalue of 0.04. Adapted with permission from B. J. Lampkin and B. VanVeller, *J. Org. Chem.*, 2021, **86**, 18287–18291. Copyright 2021 American Chemical Society.

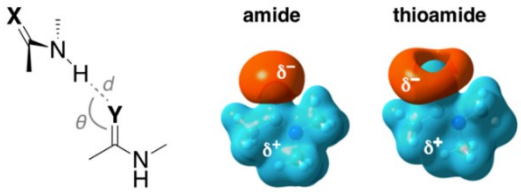

			Geometry		Interaction energy (ΔH, kcal mol^{-1})	
Entry	X	Y	d (Å)	θ (°)	Gas phase	Water (SMD)
1	O	O	1.92	116	-7.27	-3.06
2	S	O	1.89	116	-8.86 (-1.58)[a]	-4.00 (-0.93)[a]
3	O	S	2.45	97	-6.89 (+0.38)[a]	-3.30 (-0.23)[a]

The energy associated with hydrogen bonds is sensitive to the environment. Hydrogen bonds in vacuum and hydrophobic environments are generally much stronger than hydrogen bonds in polar environments like water. This reduction in the strength can be attributed in part to screening of attractive electrostatic interactions and to entropic effects. Lampkin and VanVeller's study exemplifies the effect of solvent as well.[59] They tested the strength of S···H–N hydrogen bonds in implicit water solvent and found weaker interactions than in the gas phase. Moreover, they found that thioamides are slightly stronger hydrogen bond acceptors compared to amides in polar media. With regard to entropy, in vacuum, peptide side-chains fold back to form internal hydrogen bonds, whereas in water they have other options.[60–62]

2.1.4.1.3 S–H···O type hydrogen bonds

The statistical analysis conducted by Zhou et al. mentioned above also suggests that it is more likely for Cys to act as a hydrogen bond donor than a hydrogen bond acceptor (donor–acceptor ratio 5 : 1).[49] Paul and

Thomas studied S–H···O hydrogen bonds using local energy decomposition (LED)[63] analysis on different thiol–water complexes and showed that the binding energy of the resulting hydrogen bonds ranges from −2.1 to −3.6 kcal mol^{-1} and the dominant source of stabilization in these complexes was electrostatic attraction.[64] NBO analysis on these systems also pointed to the importance of $O_{lp} \leftrightarrow \sigma^*_{S-H}$ orbital interactions (the natural orbital interaction energies for selected thiol– water complexes varied from ∼3–5.5 kcal mol^{-1} at the B3LYP/cc-pVTZ level of theory).

2.1.4.1.4 S–H···N type hydrogen bonds

Mielke and coworkers studied O–H···N and S–H···N interactions in $CH_3OH\cdots NH_3$ and $CH_3SH\cdots NH_3$ complexes.[65] They reported a larger interaction energy for $CH_3OH\cdots NH_3$, inconsistent with the stronger aqueous acidity of CH_3SH compared to CH_3OH. Jaju et al. calculated the S–H···N hydrogen bonding stabilization energy in the [C_5H_5–N···H–SH] complex to be ∼3 kcal mol^{-1}, which is ∼1 kcal mol^{-1} larger than the S–H···O interaction in the $SH_2\cdots CH_3OH$ complex (at the MP2/aug-cc-pVTZ level),[66] perhaps due simply to the higher basicity of the N atom than the O atom. The distances for the S–H···N and S–H···O hydrogen bonds in these complexes are predicted to be 2.08 Å and 2.10 Å, respectively. Although the major source of stability of the S–H···N hydrogen bond is predicted to come from donor–acceptor interactions ($N_{lp} \leftrightarrow \sigma^*_{H-S}$), electrostatic and dispersion interactions are also important contributors.

2.1.4.2 S···O and S···N interactions

Although sometimes overlooked, S···O and S···N interactions are common in biological systems. For example, more than two decades ago, Nagao et al. revealed that an S···O interaction (∼2.5 Å) was present in the (acylimino)thiadiazoline moiety of a class of angiotensin II receptor antagonists.[67] In general, an interatomic S···O distance shorter than the sum of sulfur and oxygen van der Waals radii (3.32 Å) is taken as an indication of the presence of a favorable S···O interaction. While there is some debate over the origins of close S···O and S···N contacts,[68] both electrostatic and dispersion interactions are known to contribute and these can be comparable in strength.[69] The electrostatic stabilization comes from attraction between

partially positively charged sulfur (note that sulfur is not very electronegative and is frequently found near to electron-withdrawing groups in biological settings) and partially negatively charged oxygen or nitrogen.[12] In addition to electrostatic and dispersion interactions, donor–acceptor orbital interactions (e.g., $O_{lp} \leftrightarrow \sigma^*_{S-X}$) also are significant for the directional preference of S···O and S···N contacts,[70] even if these are counterbalanced by S lone pair/O or N lone pair repulsion.[68] Recently, Biswal et al. found that interaction energies associated with donor–acceptor orbital interactions ($O_{lp} \leftrightarrow \sigma^*_{S-C}$) are typically ∼2 kcal mol^{-1} and ∼1 kcal mol^{-1} for small molecules obtained from the Cambridge Structural Database (CSD) and the Protein Data Bank (PDB), respectively.[71]

2.1.4.3 Interactions involving π-systems

A statistical analysis on sulfur–aromatic interactions was carried out by Zauhar et al. by collecting all crystal structures that contain at least one divalent sulfur atom and a phenyl ring from the Cambridge Crystallographic Database.[72] The results suggest that, for an ideal interaction the sulfur–aromatic distance should be ∼5 Å and the sulfur should be placed in the plane of the ring as opposed to the trend observed for proteins, which places sulfur above the ring plane. This contradiction may be attributed to the stacking interactions present in small planar molecules that favor edge-on interactions or to the crystal packing forces that play crucial roles in controlling overall geometries, especially when weak interactions are involved. Energy analysis showed that a single sulfur–aromatic interaction contributes ∼1–2 kcal mol^{-1} to the stability of a protein and involves both van der Waals and electrostatic components, with their relative contributions varying with structure. There are several common structural motifs in which sulfur atoms are ∼5 Å away from aromatic rings, differing by which, if any, groups shield the sulfur atom from the π-electrons of the aromatic system.

2.1.4.3.1 SC–H···π interactions

One important sulfur-based interaction that contributes to protein structure is the SC–H···π interaction, which is mainly observed in the hydrophobic cores of proteins.[16,17,73] SC–H···π interactions were first analyzed by Morgan et al. in the 1970s.[74] The analysis of eight small globular proteins revealed the presence of SC–H···π contacts between sidechains. A follow up study by Reid et al. showed that, in contrast to OC–H and NC–H groups, SC–H groups tend to interact away from the center of the aromatic rings.[75] Compared to a hydrophobic interaction with sulfur traded for an alkyl group, SC–H···π interactions are more stable at greater distances, which can be attributed to dispersion interactions involving the polarizable sulfur atom.[69,76] While SC–H···π interactions are largely dispersive in nature, electrostatics do influence orientational preferences.[17,72,77]

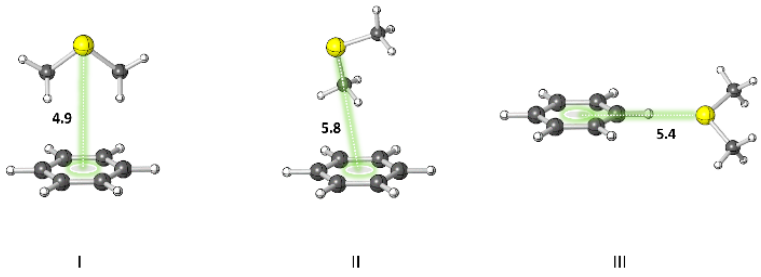

Figure 2.1.5. Three different orientations of DMS–benzene complexes. (I) The sulfur atom is placed on the symmetry axis of the benzene ring and the two methyl groups are directed towards the face of the benzene ring. (II) One of the methyl groups is oriented towards the face of the benzene ring. (III) The sulfur atom is pointed towards the edge of the benzene ring. Distances shown in Å.[78]

Pranata investigated dimethyl sulfide (DMS)–benzene complexes, models of a Met sidechain and an aromatic residue, in detail.[78] Three different orientations of DMS–benzene complexes were studied (Figure 2.1.5). Ab initio calculations based on isolated molecules (not necessarily PES minima) predicted that complex I (Figure 2.1.5) had the largest interaction energy (−2.9 kcal mol^{-1} at the MP2/6-31G* level) and the shortest contact distance from the sulfur atom to the center of the benzene ring (4.9 Å) (compared to complex II and complex III). Note that upon full optimization of complex II at the MP2/6-31G* level, a

structure similar to complex I, but with the DMS horizontally displaced, was generated, which also was predicted to have an interaction energy of −2.9 kcal mol^{-1}. This study also suggested that the molecular mechanics force fields AMBER95 and OPLS-AA can reproduce the MP2/6-31G* results.

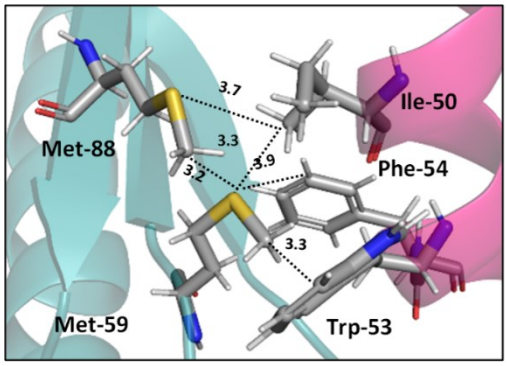

Figure 2.1.6. Crystal structure of Tfb1 (green)/p53 (orange) complex (PDB ID:2GS0) showing Tfb1-Met/p53-Ile, Tfb1-Met/p53-Phe and Tfb1-Met/p53-Trp interactions. Distances shown in Å.[79]

Interactions analogous to those in complex II (Figure 2.1.5) are found in protein structures. For example, Di Lello et al. determined the structure of a complex formed by the interaction between the amino-terminal transactivation domain of p53 and the pleckstrin homology domain of transcription factor b1 (Tfb1) by high-resolution NMR.[79] In the Tfb1/p53 binding interface (shown in Figure 2.1.6) the Met-59 residue participates in sulfur–π interactions with Trp-53. Additional contacts present between the isoleucine (Ile) and phenylalanine (Phe) residues of p53 and the Met residues of Tfb1 contribute to the overall stability of the complex.

2.1.4.3.2 S–H···π interactions

Sherrill and co-workers studied the interaction of H_2S with benzene, which can be considered to be a small model of Cys interacting with an aromatic sidechain.[77] They found that the electrostatic interaction (−2.4 kcal mol^{-1}) arising from the partial positive charge on the H_2S hydrogens and the partial negative charge in the benzene π-cloud leads to substantial attraction, while the dispersion energy (−4.2 kcal mol^{-1}) provides an even larger attractive component.

The S–H···π interactions in indole·H_2S (IND·H_2S) and 3-methylindole·H_2S (3-MI·H_2S) complexes, models of Cys interacting with the sidechain of tryptophan (Trp), were studied by Biswal and Wategaonkar.[80] Both σ-type (S···H–O and S···H–N; see sections 2.1.4.1.1–2) and π-type (S–H···π; Figure 2.1.7) complexes were investigated. Computations at the MP2/aug-cc-pVDZ level of theory suggested that the binding energies for π-type and σ-type IND·H_2S complexes are −4.9 and −2.7 kcal mol^{-1}, respectively. Similarly, the binding energies for π-type and σ-type 3-MI·H_2S complexes are −5.2 and −2.7 kcal mol^{-1}, respectively. In contrast, for IND·H_2O and 3-MI·H_2O complexes, σ-type complexes are preferred. Moreover, they found that the S–H···π interaction was stronger than other X–H···π (X = C, N, O) interactions.

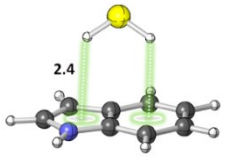

Figure 2.1.7. π-type IND·H_2S complex. Distances shown in Å.[80]

2.1.4.3.3 S···π interactions

Dougherty and co-workers suggested that direct S···π interactions are functionally important in the maintenance of a tightly packed microdomain functioning as a unit in the dopamine D2 receptor (although S–H···π interactions could not be ruled out).[81] They used the crystal structure of the dopamine D3 receptor[82] as a model (Figure 2.1.8) and located a highly conserved microdomain. Mutant cycle analysis and unnatural amino acid mutagenesis on the residues in this microdomain in the related D2 receptor suggested that the strong interaction between Trp and Cys residues in which the sulfur containing side chain of a Cys residue points to the face of the aromatic ring of a Trp contributes to the rigidity of the microdomain.

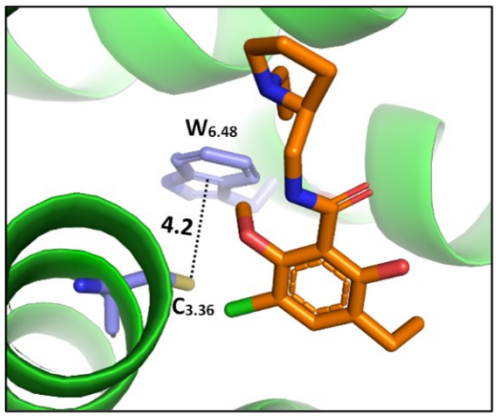

Figure 2.1.8. The cocrystal structure (PDB ID: 3PBL) of the dopamine D3 receptor bound to antagonist eticlopride (in orange). Distances shown in Å.[82]

To compare the strengths of direct interactions between the π-faces of aromatic rings with oxygen and sulfur, Motherwell et al. prepared the series of oxathiolanes shown in Figure 2.1.9 (and others), which can adopt conformations with either an oxygen or sulfur atom proximal to an aromatic ring.[83] Based on their results, it appears that (a) oxygen atoms do not like to be near the π-faces of electron-rich aromatics, (b) sulfur atoms do not mind being near the π-faces of electron-rich aromatics, (c) oxygen atoms do not mind being near the π-faces of electron poor aromatics. While it is difficult to pin down the relative contributions of attraction and repulsion in such systems, it is clear that sulfur can reside near the π-face of aromatics, even electron-rich ones, likely a consequence of its polarizability.

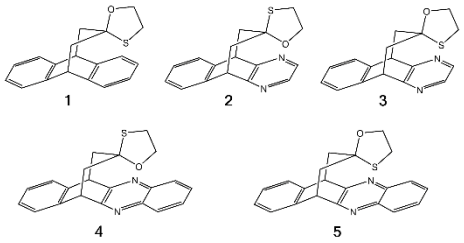

Figure 2.1.9. π systems studied by Motherwell et al. to compare S···π versus O···π noncovalent interactions.[83]

Viguera and Serrano's work on sidechain interactions between sulfur containing amino acids (Cys and Met) and phenylalanine (Phe) residues—the first experimental analysis probing helix stability mediated

by Phe and Cys/Met interactions—showed that these interactions are related directly to the stability of α helices.[84,85] The origins of this α helix stability appears to come from both the hydrophobic nature of the aromatic rings and the electrostatic interactions between the S and the aromatic ring (primarily dispersion).

Two tumor necrosis factor (TNF) ligand–receptor complexes TRAIL-DR5 and LTα-TNFR1 were examined both experimentally via vitro cellular experiments and computationally to probe the role of the Met–aromatic binding motif.[76] DR5-Met/TRAIL-Tyr (left) and TNFR1-Trp/LTα-Met (right) interactions are shown in Figure 2.1.10. Molecular dynamics simulations were used to obtain bioactive conformers that match with those in the Protein Data Bank (PDB). The results from quantum mechanical calculations suggested that dispersive sulfur–aromatic interactions at around 5 Å separation provide extra stability (~1–1.5 kcal mol^{-1}) to the protein compared to interactions within their analogues where sulfur was replaced with CH_2. Note that SC–H···π interactions (section 2.1.4.3.1) may also contribute here (and in the following cases).

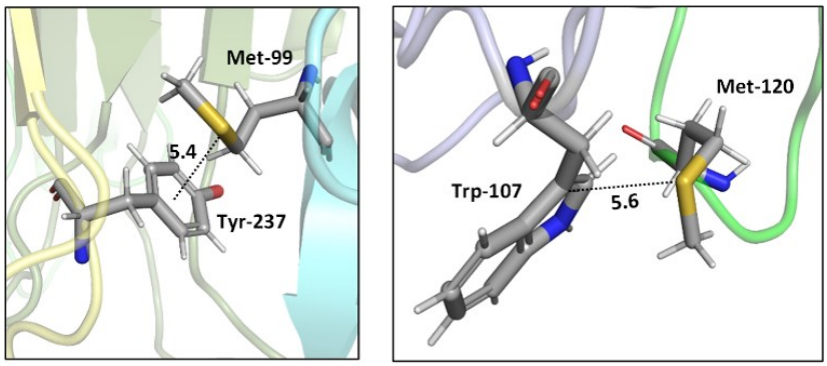

Figure 2.1.10. Crystal structures of TRAIL-DR5 showing DR5-Met/TRAIL-Tyr interaction (left, PDB ID: 1D0G) and LTα-TNFR1 showing TNFR1-Trp/LTα-Met interaction (right, PDB ID: 1TNR). Both Met–aromatic contacts are at around 5 Å separation. Distances shown in Å.[76]

Tatko and Waters investigated the nature of sulfur-π interactions in a β-hairpin by putting a Met residue diagonal to an aromatic ring (Trp or Phe) (Figure 2.1.11).[86] The proximity between Met and the aromatic ring provides a suitable geometry for sulfur-π contacts to occur. They found that the Met

significantly contributes to β-hairpin stability with a hydrophobic driving force (for instance, as determined by double-mutant cycles, Met–Phe interaction contributes −0.31 kcal mol^{-1}).

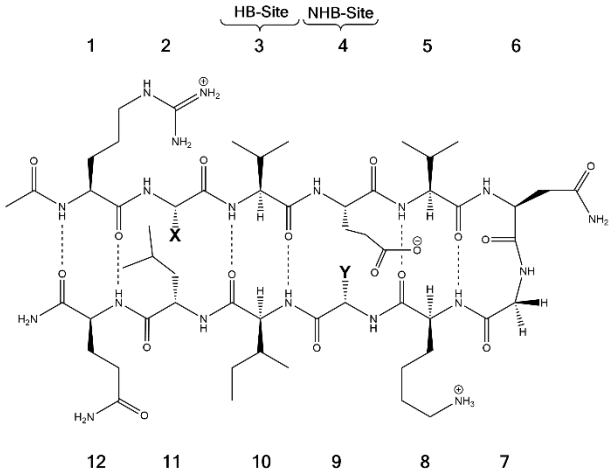

Figure 2.1.11. The model system consisting of 12 amino acids. X (= Phe, Trp, Cha) and Y (= Lys, Nle, Met) are the diagonal interacting residues. The hydrogen bonded and nonhydrogen-bonded sites are abbreviated as HB-site and NHB-site, respectively.[86]

Albanese and Waters examined the role of sulfur in the Met residues in the binding of a gene expression regulator trimethyllysine (Kme3).[87] They probed the recognition of Kme3 by the Met containing aromatic cage in the reader proteins DIDO1 and TAF3 by systematic mutational studies (Figure 2.1.12). For both systems, they observed a change in the NMR chemical shifts of the Met residue upon binding histone 3 K4me3 (H3K4me3), which indicated the presence of a binding interaction. Linear free energy relationships suggested that the origin of this Met–Kme3 binding was dispersive, which again could be attributed to the high polarizability of sulfur. They also found that the charge on Kme3 did not alter the interaction with the Met, which suggested that the electrostatic interactions (sulfur–cation) do not contribute significantly to binding.[87]

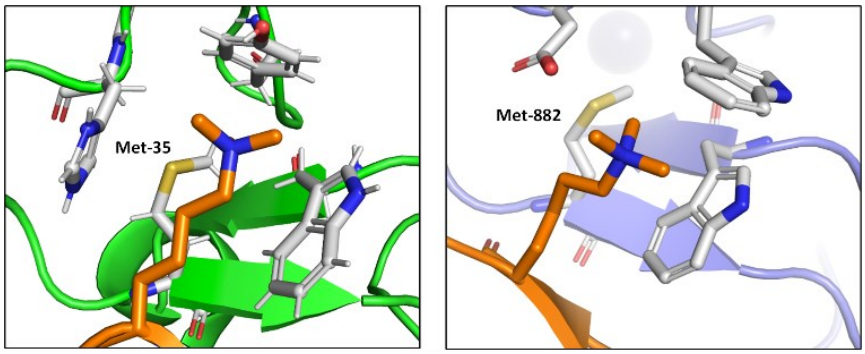

Figure 2.1.12. The molecular recognition of H3K4me3 (in orange) by DIDO1 (in green, PDB ID: 4L7X) and TAF3 (in purple, PDB ID: 5WXH).[87]

A study on a cisplatin–(1,3-GTG) cross-link within DNA polymerase η revealed that the Met residue in the DNA polymerase η participates in sulfur–arene interactions, which helps maintain the folded geometry of the protein complex and blocks the movement of the polymerase along the DNA strand (Figure 2.1.13).[88] In this complex, both S···π and SC–H···π interactions are present.

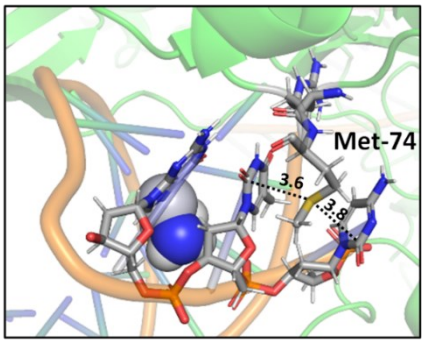

Figure 2.1.13. Crystal structure of cisplatin–(1,3-GTG) lesion in complex with DNA polymerase η (PDB ID: 2WTF). The Met residue surrounded by nucleobases blocks the movement of the polymerase along the DNA strand. Distances shown in Å.[88]

Recently, Waters and coworkers compared the strength of the sulfonium···π, S···π and ammonium···π interactions in a β-hairpin peptide model system via a combination of computational studies and analysis of structures in the PDB.[89] They found that, presumably due to sulfur's higher polarizability, sulfonium···π interactions are stronger than ammonium···π interactions. Further comparison of sulfonium···π and S···π interaction energies by the analysis of S-adenosylmethionine (SAM) and S-

adenosylhomocysteine (SAH)-bound proteins in the PDB highlighted the importance of charge. They found similar aromatic interactions between SAM and SAH except for the methyl···π interaction that is only present in SAM, which highly influences the bioactivity of SAM-dependent methyltransferases (Figure 2.1.14).[89] This interaction is an example of a SC–H···π interaction (section 2.1.4.3.1) enhanced by charge.

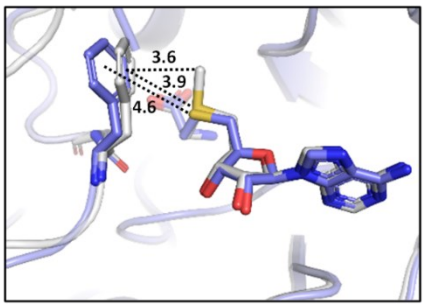

Figure 2.1.14. Aromatic interactions of *T. thermophilus* ribosomal protein L11 methyltransferase with SAM (PDB ID: 2NXE, in gray) and SAH (PDB ID: 3EGV, in plum).[89]

2.1.4.3.4 S···$\pi^*_{C=O}$ interactions

$n \rightarrow \pi^*$ interactions resulting from the overlap of lone pairs (n) and π^* antibonding orbitals along the Bürgi–Dunitz trajectory play an important role in maintaining the conformational stability of proteins (Figure 2.1.15).[90,91] Similar to the observations of Bürgi and Dunitz for other lone pair donors (Figure 2.1.15B, θ angle), Chakrabarti and Pal found that the preferred S···C–O angle for the $n_S \rightarrow \pi^*_{C=O}$ interaction is 109° (± 15°).[92]

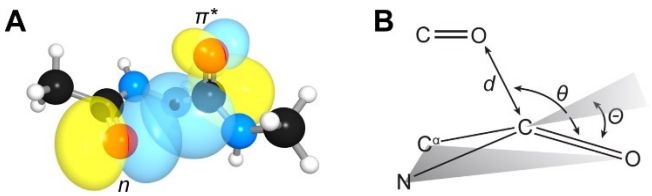

Figure 2.1.15. (A) $n \rightarrow \pi^*$ orbital interaction in the backbone of bitter gourd trypsin inhibitor (PDB: 1VBW), residues 5–7. **(B)** Geometric parameters characterizing $n \rightarrow \pi^*$ interaction (d: distance between the nucleophile and carbonyl; θ: angle of the nucleophilic attack; Θ: degree of pyramidalization). Adapted

with permission from R. W. Newberry, G. J. Bartlett, B. VanVeller, D. N. Woolfson and R. T. Raines, Protein Sci., 2014, 23, 284–288. Copyright 2014 John Wiley & Sons, Inc.

Many experimental and computational studies by Raines and co-workers have revealed the intricacies of stereoelectronic effects in tuning the secondary structures of proteins, including the importance of $n \rightarrow \pi^*$ interactions.[11,93–100] For instance, Choudhary et al. explored the origin of carbonyl–carbonyl interaction in proteins and found that thioamides are better electron-pair donors compared to their amide counterparts.[93] Newberry et al. reported that the $n \rightarrow \pi^*$ interaction between amide carbonyl groups in proteins contributes ≥0.27 kcal mol^{-1}, and this magnitude triples when the interaction is between two thioamides due to better orbital overlap and a lower energy gap between donor and acceptor orbitals.[95] They also observed an increase in the pyramidalization of the acceptor C atom as the $n \rightarrow \pi^*$ interaction strengthens, consistent with work on related systems.[93,95,100–102] The stability of the collagen triple helix – which is highly affected by hydrogen bonds and $n \rightarrow \pi^*$ interactions[103] – was also shown to be increased upon replacement of backbone amides with thioamides.[94] Later, Kilgore at al. probed the importance of $n_S \rightarrow \pi^*_{C=O}$ interactions in Cys residues and disulfide bonds in proteins.[98] They found that $n_S \rightarrow \pi^*$ interactions provided enhanced stability and led to lowered pKa values of N-terminal Cys residues of the CXXC motifs[104] (shown in Figure 2.1.16), which are critical for redox functions. In addition, the strong $n_S \rightarrow \pi^*_{C=O}$ interactions present in vicinal disulfide bonds led to an electropositive (and hydrophobic site) for ligand binding.[98]

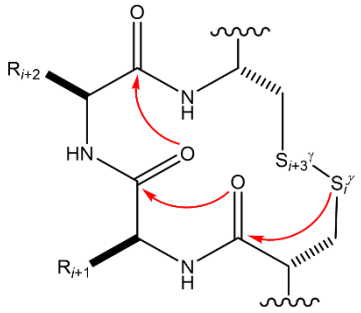

Figure 2.1.16. The map of n → π* interactions inside the CXXC motif.[98]

2.1.4.4 Generalizations

Table 2.1.2 represents the typical magnitudes and the major sources of stabilization for the sulfur noncovalent interactions reviewed here. However, we would like to warn our readers that the magnitude of stabilization may vary, since it highly depends on the system of interest and its environment.

Table 2.1.2. Current best estimates of typical magnitudes and the major sources of stabilization for the sulfur noncovalent interactions reviewed in this contribution.

Interaction Type	Typical Magnitude (kcal mol^{-1})	Major Sources of Stabilization
S-H•••O	~ 2-6	Electrostatics > Donor-Acceptor > Dispersion
S-H•••N	~ 3	Donor-Acceptor > Electrostatics > Dispersion
S•••H-O	~ 2-5	Dispersion > Electrostatics > Donor-Acceptor
S•••H-N	~ 2	Dispersion > Electrostatics > Donor-Acceptor
S•••O	~ 2-3	Dispersion ≈ Electrostatics > Donor-Acceptor
S•••N	~ 2-3	Dispersion ≈ Electrostatics > Donor-Acceptor
SC-H•••π	~ 3	Dispersion > Electrostatics > Donor-Acceptor
S-H•••π	~ 2-5	Dispersion > Electrostatics > Donor-Acceptor
S•••π	~ 0.3-3	Dispersion > Electrostatics ≈ Donor-Acceptor
S•••$\pi^*_{C=O}$	~ 0.25-3	Donor-Acceptor > Dispersion ≈ Electrostatics

2.1.5 Recommendations for Modelers

Computational chemistry is an indispensable tool to study noncovalent interactions in biological systems. With the aid of quantum chemical calculations, one can investigate these interactions both qualitatively and quantitatively. Nowadays, most computational studies on noncovalent interactions are carried out using density functional theory (DFT),[105] a versatile computational modelling method for calculating the electronic structure of atoms and molecules. However, the choice of which method to use – DFT or a more expensive but more accurate method – depends on the system of interest. One generally faces a compromise between accuracy and computational cost (i.e., time for calculations to finish with available computer

resources). Here, we recommend a few methods that have been found useful for studying noncovalent interactions involving sulfur atoms. The DFT functionals that account for dispersion correction such as ωB97X-D,[106] M06-2X,[107–109] PBE0-D3,[110,111] B3LYP-D3(BJ)[105,112–114] have been commonly used in geometry optimizations and provided reasonable results.[53,56,64,71,115–118] Due to issues with DFT in describing dispersion interactions, many have chosen second-order Møller–Plesset perturbation theory (i.e., MP2) or coupled cluster (CC) theory with single, double and perturbative triple excitations (i.e. CCSD(T)).[47,53,65,66,77,116,117,119–121,122] For small systems, these methods can be affordable. A study by Rothlisberger and co-workers showed that dispersion corrected atom centered potentials (DCACPs)[123,124] significantly improve the DFT description of the weak interactions of sulfur-containing molecules and the resulting DFT method correctly reproduces MP2 or CCSD(T) binding energies.[120] For basis sets, double-ζ or triple-ζ Pople type basis sets that include diffuse and polarization functions, Weigend's def2-TZVP[125,126] basis set, and Dunning's correlation-consistent cc-pVnZ or augmented correlation-consistent aug-cc-pVnZ (where n = D, T, or Q) basis sets[127–131] are commonly used in calculations on sulfur-based noncovalent interactions.[53,56,64–66,71,77,115–117,119–121] To obtain reliable interaction energies, the counterpoise correction for basis set superposition error (BSSE)[132] and corrections for zero-point vibrational energies are recommended, especially when small basis sets are used.[133–135]

If one wishes to include solvent in one's modelling, there are three general approaches: implicit solvation, explicit solvation, and a hybrid of the two. In implicit solvation, the solvent is treated as a continuum with a certain dielectric constant (and other properties). In explicit solvation, the solvent is treated as discrete molecules. Hybrid solvation modelling involves using a few explicit solvent molecules with an implicit solvent model on top. Using an implicit model is the most affordable approach, but a hybrid approach can be used as a balancing act between a realistic and a cost-efficient treatment of solvent, especially if noncovalent interactions between solute and solvent are important.[136–138]

If one wishes to include a whole protein in one's modelling, the Quantum Mechanics/Molecular Mechanics (QM/MM) approach is the way to go. This approach was introduced by Warshel and Levitt in

the 1970s.[139,140] The QM/MM method is an efficient way of studying large systems in which a small region of the system—that where the key chemical processes take place—is treated quantum-mechanically, while the remainder of the system is treated classically, e.g., using molecular mechanics or a force field. Recently, Jorgensen and co-workers developed a new force field that improved the representation of sulfur charge anisotropy and directional noncovalent interactions via the addition of off-atom charged sites,[141] a welcome development for those modelling systems with sulfur-based noncovalent interactions. In the popular multilayer approach known as ONIOM, a large biomolecule is divided into "n" number of layers and each layer is treated with a different model chemistry (i.e, ab initio, semi-empirical and molecular mechanics) at a reduced cost.[142,143] We recommend a careful consideration in choosing suitable QM and MM methods, how one partitions a system into QM and MM regions, and how one treats the interactions between QM and MM regions. Along these lines, we direct readers to recent reviews for a deeper dive into QM/MM modelling.[144,145]

2.1.6 Conclusion and Outlook

While sulfur may not receive the same attention as carbon, hydrogen, nitrogen, and oxygen, it plays many important roles in biology. Here we have summarized the variety of types of noncovalent interactions in which it participates, illustrated with examples from protein structures and accompanied by accounts of theoretical studies on preferred geometries and interaction energies. We hope that bringing these examples together will inspire readers not only to consider noncovalent interactions involving sulfur when examining structures of biological molecules that have captured their interest, but also to make use of them in designing new molecules of biological relevance.

2.1.7 Acknowledgements

We gratefully acknowledge continued financial and computational support from the US National Science Foundation.

2.1.8 References

(1) Dill, K. A. Dominant Forces in Protein Folding. *Biochemistry* **1990**, *29*, 7133–7155.
(2) Pace, C. N.; CN, P. Measuring and Increasing Protein Stability. *Trends Biotechnol.* **1990**, *8*, 93–98.
(3) Pace, C. N. Conformational Stability of Globular Proteins. *Trends Biochem. Sci.* **1990**, *15*, 14–17.
(4) Trevino, S. R.; Schaefer, S.; Scholtz, J. M.; Pace, C. N. Increasing Protein Conformational Stability by Optimizing β-Turn Sequence. *J. Mol. Biol.* **2007**, *373*, 211.
(5) Deller, M. C.; Kong, L.; Rupp, B. Protein Stability: A Crystallographer's Perspective. *Acta Crystallogr. Sect. F, Struct. Biol. Commun.* **2016**, *72*, 72.
(6) Waters, M. L. Aromatic Interactions in Peptides: Impact on Structure and Function. *Pept. Sci.* **2004**, *76*, 435–445.
(7) Jena, S.; Dutta, J.; Tulsiyan, K. D.; Sahu, A. K.; Choudhury, S. S.; Biswal, H. S. Noncovalent Interactions in Proteins and Nucleic Acids: Beyond Hydrogen Bonding and π-Stacking. *Chem. Soc. Rev.* **2022**, *51*, 4261–4286.
(8) Cockroft, S. L.; Hunter, C. A. Chemical Double-Mutant Cycles: Dissecting Non-Covalent Interactions. *Chem. Soc. Rev.* **2007**, *36*, 172.
(9) Wagner, J. P.; Schreiner, P. R. London Dispersion in Molecular Chemistry - Reconsidering Steric Effects. *Angew. Chem. Int. Ed.* **2015**, *54*, 12274–12296.
(10) Persch, E.; Dumele, O.; Diederich, F. Molecular Recognition in Chemical and Biological Systems. *Angew. Chem. Int. Ed.* **2015**, *54*, 3290–3327.
(11) Newberry, R. W.; Raines, R. T. Secondary Forces in Protein Folding. *ACS Chem. Biol.* **2019**, *14*, 1677–1686.
(12) Burling, F. T.; Goldstein, B. M. Computational Studies of Nonbonded Sulfur-Oxygen and Selenium-Oxygen Interactions in the Thiazole and Selenazole Nucleosides. *J. Am. Chem. Soc.* **1992**, *114*, 2313–2320.
(13) Gómez-Tamayo, J. C.; Cordomí, A.; Olivella, M.; Mayol, E.; Fourmy, D.; Pardo, L. Analysis of the Interactions of Sulfur-Containing Amino Acids in Membrane Proteins. *Protein Sci.* **2016**, *25*, 1517–1524.
(14) Brandt, W.; Golbraikh, A.; Täger, M.; Lendeckel, U. A Molecular Mechanism for the Cleavage of a Disulfide Bond as the Primary Function of Agonist Binding to G-Protein-Coupled Receptors Based on Theoretical Calculations Supported by Experiments. *Eur. J. Biochem.* **1999**, *261*, 89–97.
(15) Hati, S.; Bhattacharyya, S. Impact of Thiol-Disulfide Balance on the Binding of Covid-19 Spike Protein with Angiotensin-Converting Enzyme 2 Receptor. *ACS Omega* **2020**, *5*, 16292–16298.
(16) Meyer, E. A.; Castellano, R. K.; Diederich, F. Interactions with Aromatic Rings in Chemical and Biological Recognition. *Angew. Chem. Int. Ed.* **2003**, *42*, 1210–1250.
(17) Salonen, L. M.; Ellermann, M.; Diederich, F. Aromatic Rings in Chemical and Biological Recognition: Energetics and Structures. *Angew. Chem. Int. Ed.* **2011**, *50*, 4808–4842.
(18) Beno, B. R.; Yeung, K. S.; Bartberger, M. D.; Pennington, L. D.; Meanwell, N. A. A Survey of the Role of Noncovalent Sulfur Interactions in Drug Design. *J. Med. Chem.* **2015**, *58*, 4383–4438.
(19) Bissantz, C.; Kuhn, B.; Stahl, M. A Medicinal Chemist's Guide to Molecular Interactions. *J. Med. Chem.* **2010**, *53*, 5061–5084.
(20) Vitek, A. K.; Jugovic, T. M. E.; Zimmerman, P. M. Revealing the Strong Relationships between Ligand Conformers and Activation Barriers: A Case Study of Bisphosphine Reductive Elimination. *ACS Catal.* **2020**, *10*, 7136–7145.
(21) Brethomé, A. V.; Fletcher, S. P.; Paton, R. S. Conformational Effects on Physical-Organic Descriptors: The Case of Sterimol Steric Parameters. *ACS Catal.* **2019**, *9*, 2313–2323.
(22) Olanders, G.; Alogheli, H.; Brandt, P.; Karlén, A. Conformational Analysis of Macrocycles: Comparing General and Specialized Methods. *J. Comput. Aided. Mol. Des.* **2020**, *34*, 231–252.
(23) Lewis-Atwell, T.; Townsend, P. A.; Grayson, M. N. Comparisons of Different Force Fields in Conformational Analysis and Searching of Organic Molecules: A Review. *Tetrahedron* **2021**, *79*,

131865.
(24) Cole, J. C.; Korb, O.; McCabe, P.; Read, M. G.; Taylor, R. Knowledge-Based Conformer Generation Using the Cambridge Structural Database. *J. Chem. Inf. Model.* **2018**, *58*, 615–629.
(25) Klebe, G. Toward a More Efficient Handling of Conformational Flexibility in Computer-Assisted Modelling of Drug Molecules. *Perspect. Drug Discov. Des.* **1995**, *3*, 85–105.
(26) Sliwoski, G.; Kothiwale, S.; Meiler, J.; Lowe, E. W. Computational Methods in Drug Discovery. *Pharmacol. Rev.* **2014**, *66*, 334.
(27) Liao, C.; Sitzmann, M.; Pugliese, A.; Nicklaus, M. C. Software and Resources for Computational Medicinal Chemistry. *Future Med. Chem.* **2011**, *3*, 1057.
(28) Liwo, A.; Czaplewski, C.; Ołdziej, S.; Scheraga, H. A. Computational Techniques for Efficient Conformational Sampling of Proteins. *Curr. Opin. Struct. Biol.* **2008**, *18*, 134.
(29) Foloppe, N.; Chen, I.-J. Conformational Sampling and Energetics of Drug-like Molecules. *Curr. Med. Chem.* **2009**, *16*, 3381–3413.
(30) Houk, K. N.; Leach, A. G.; Kim, S. P.; Zhang, X. Binding Affinities of Host–Guest, Protein–Ligand, and Protein–Transition-State Complexes. *Angew. Chem. Int. Ed.* **2003**, *42*, 4872–4897.
(31) Williams, D. H.; Stephens, E.; O'Brien, D. P.; Zhou, M. Understanding Noncovalent Interactions: Ligand Binding Energy and Catalytic Efficiency from Ligand-Induced Reductions in Motion within Receptors and Enzymes. *Angew. Chem. Int. Ed.* **2004**, *43*, 6596–6616.
(32) Scheiner, S. On the Reliability of Atoms in Molecules, Noncovalent Index, and Natural Bond Orbital to Identify and Quantify Noncovalent Bonds. *J. Comput. Chem.* **2022**, *43*, 1814–1824.
(33) Johnson, E. R.; Keinan, S.; Mori-Sánchez, P.; Contreras-García, J.; Cohen, A. J.; Yang, W. Revealing Noncovalent Interactions. *J. Am. Chem. Soc.* **2010**, *132*, 6498–6506.
(34) Lefebvre, C.; Khartabil, H.; Boisson, J. C.; Contreras-García, J.; Piquemal, J. P.; Hénon, E. The Independent Gradient Model: A New Approach for Probing Strong and Weak Interactions in Molecules from Wave Function Calculations. *ChemPhysChem* **2018**, *19*, 724–735.
(35) Lu, T.; Chen, F. Multiwfn: A Multifunctional Wavefunction Analyzer. *J. Comput. Chem.* **2012**, *33*, 580–592.
(36) Bader, R. F. W. A Quantum Theory of Molecular Structure and Its Applications. *Chem. Rev.* **1991**, *91*, 893–928.
(37) Bader, R. F. W. Atoms in Molecules. *Acc. Chem. Res.* **1985**, *18*, 9–15.
(38) Cremer, D.; Kraka, E. Chemical Bonds without Bonding Electron Density — Does the Difference Electron-Density Analysis Suffice for a Description of the Chemical Bond? *Angew. Chem. Int. Ed.* **1984**, *23*, 627–628.
(39) Espinosa, E.; Alkorta, I.; Elguero, J.; Molins, E. From Weak to Strong Interactions: A Comprehensive Analysis of the Topological and Energetic Properties of the Electron Density Distribution Involving X–H···F–Y Systems. *J. Chem. Phys.* **2002**, *117*, 5529.
(40) Weinhold, F.; Landis, C. R.; Glendening, E. D. What Is NBO Analysis and How Is It Useful? *Int. Rev. Phys. Chem.* **2016**, *35*, 399–440.
(41) Phipps, M. J. S.; Fox, T.; Tautermann, C. S.; Skylaris, C. K. Energy Decomposition Analysis Approaches and Their Evaluation on Prototypical Protein–Drug Interaction Patterns. *Chem. Soc. Rev.* **2015**, *44*, 3177–3211.
(42) Kitaura, K.; Morokuma, K. A New Energy Decomposition Scheme for Molecular Interactions within the Hartree-Fock Approximation. *Int. J. Quantum Chem.* **1976**, *10*, 325–340.
(43) Morokuma, K. Why Do Molecules Interact? The Origin of Electron Donor-Acceptor Complexes, Hydrogen Bonding, and Proton Affinity. *Acc. Chem. Res.* **1977**, *10*, 294–300.
(44) Khaliullin, R. Z.; Cobar, E. A.; Lochan, R. C.; Bell, A. T.; Head-Gordon, M. Unravelling the Origin of Intermolecular Interactions Using Absolutely Localized Molecular Orbitals. *J. Phys. Chem. A* **2007**, *111*, 8753–8765.
(45) Jeziorski, B.; Moszynski, R.; Szalewicz, K. Perturbation Theory Approach to Intermolecular Potential Energy Surfaces of van Der Waals Complexes. *Chem. Rev.* **1994**, *94*, 1887–1930.
(46) Kojasoy, V.; Tantillo, D. J. Importance of Noncovalent Interactions Involving Sulfur Atoms in

Thiopeptide Antibiotics–Glycothiohexide α and Nocathiacin I. *J. Phys. Chem. A* **2023**, *127*, 2081–2090.
(47) Biswal, H. S. Hydrogen Bonds Involving Sulfur: New Insights from Ab Initio Calculations and Gas Phase Laser Spectroscopy. *Challenges Adv. Comput. Chem. Phys.* **2015**, *19*, 15–45.
(48) Gregoret, L. M.; Rader, S. D.; Fletterick, R. J.; Cohen, F. E. Hydrogen Bonds Involving Sulfur Atoms in Proteins. *Proteins Struct. Funct. Bioinf.* **1991**, *9*, 99–107.
(49) Zhou, P.; Tian, F.; Lv, F.; Shang, Z. Geometric Characteristics of Hydrogen Bonds Involving Sulfur Atoms in Proteins. *Proteins Struct. Funct. Bioinf.* **2009**, *76*, 151–163.
(50) Sticke, D. F.; Presta, L. G.; Dill, K. A.; Rose, G. D. Hydrogen Bonding in Globular Proteins. *J. Mol. Biol.* **1992**, *226*, 1143–1159.
(51) Kamphuis, I. G.; Drenth, J.; Baker, E. N. Thiol Proteases. Comparative Studies Based on the High-Resolution Structures of Papain and Actinidin, and on Amino Acid Sequence Information for Cathepsins B and H, and Stem Bromelain. *J. Mol. Biol.* **1985**, *182*, 317–329.
(52) Bazan, J. F.; Fletterick, R. J. Viral Cysteine Proteases Are Homologous to the Trypsin-like Family of Serine Proteases: Structural and Functional Implications. *Proc. Natl. Acad. Sci. U. S. A.* **1988**, *85*, 7872.
(53) Wennmohs, F.; Staemmler, V.; Schindler, M. Theoretical Investigation of Weak Hydrogen Bonds to Sulfur. *J. Chem. Phys.* **2003**, *119*, 3208–3218.
(54) Singleton, M.; Isupov, M.; Littlechild, J. X-Ray Structure of Pyrrolidone Carboxyl Peptidase from the Hyperthermophilic Archaeon Thermococcus Litoralis. *Structure* **1999**, *7*, 237–244.
(55) Karplus, P. A.; Schulz, G. E. Refined Structure of Glutathione Reductase at 134 A Resolution. *J. Mol. Biol.* **1987**, *195*, 701–729.
(56) Andersen, C. L.; Jensen, C. S.; Mackeprang, K.; Du, L.; Jørgensen, S.; Kjaergaard, H. G. Similar Strength of the NH···O and NH···S Hydrogen Bonds in Binary Complexes. *J. Phys. Chem. A* **2014**, *118*, 11074–11082.
(57) Biswal, H. S.; Gloaguen, E.; Loquais, Y.; Tardivel, B.; Mons, M. Strength of NH···S Hydrogen Bonds in Methionine Residues Revealed by Gas-Phase IR/UV Spectroscopy. *J. Phys. Chem. Lett.* **2012**, *3*, 755–759.
(58) Pratt, K. P.; Shen, B. W.; Takeshima, K.; Davie, E. W.; Fujikawat, K.; Stoddard, B. L. Structure of the C2 Domain of Human Factor VIII at 1.5 Å Resolution. *Nature* **1999**, *402*, 439–442.
(59) Lampkin, B. J.; VanVeller, B. Hydrogen Bond and Geometry Effects of Thioamide Backbone Modifications. *J. Org. Chem.* **2021**, *86*, 18287–18291.
(60) Feldblum, E. S.; Arkin, I. T. Strength of a Bifurcated H Bond. *Proc. Natl. Acad. Sci. U. S. A.* **2014**, *111*, 4085–4090.
(61) Sheu, S. Y.; Yang, D. Y.; Selzle, H. L.; Schlag, E. W. Energetics of Hydrogen Bonds in Peptides. *Proc. Natl. Acad. Sci. U. S. A.* **2003**, *100*, 12683–12687.
(62) Gao, J.; Bosco, D. A.; Powers, E. T.; Kelly, J. W. Localized Thermodynamic Coupling between Hydrogen Bonding and Microenvironment Polarity Substantially Stabilizes Proteins. *Nat. Struct. Mol. Biol.* **2009**, *16*, 684–690.
(63) Schneider, W. B.; Bistoni, G.; Sparta, M.; Saitow, M.; Riplinger, C.; Auer, A. A.; Neese, F. Decomposition of Intermolecular Interaction Energies within the Local Pair Natural Orbital Coupled Cluster Framework. *J. Chem. Theory Comput.* **2016**, *12*, 4778–4792.
(64) Paul, A.; Thomas, R. Evidences for Sulfur Centered Hydrogen Bond with Sulfur Atoms as a Donor in Aromatic Thiols and Aliphatic Thiols in Aqueous Solution. *J. Mol. Liq.* **2021**, 118078.
(65) Grzechnik, K.; Rutkowski, K.; Mielke, Z. The S-H···N versus O-H···N Hydrogen Bonding in the Ammonia Complexes with CH 3OH and CH 3SH. *J. Mol. Struct.* **2012**, *1009*, 96–102.
(66) Jaju, K.; Pal, D.; Chakraborty, A.; Chakraborty, S. Electronic Substituent Effect on Se-H···N Hydrogen Bond: A Computational Study of Para-Substituted Pyridine-SeH2 Complexes. *Chem. Phys. Lett. X* **2019**, *4*, 100031.
(67) Nagao, Y.; Hirata, T.; Goto, S.; Sano, S.; Kakehi, A.; Iizuka, K.; Shiro, M. Intramolecular Nonbonded S···O Interaction Recognized in (Acylimino)Thiadiazoline Derivatives as Angiotensin

II Receptor Antagonists and Related Compounds. *J. Am. Chem. Soc.* **1998**, *120*, 3104–3110.
(68) Hudson, B. M.; Nguyen, E.; Tantillo, D. J. The Influence of Intramolecular Sulfur–Lone Pair Interactions on Small-Molecule Drug Design and Receptor Binding. *Org. Biomol. Chem.* **2016**, *14*, 3975–3980.
(69) Zhou, F.; Liu, R.; Li, P.; Zhang, H. On the Properties of S···O and S···π Noncovalent Interactions: The Analysis of Geometry, Interaction Energy and Electron Density. *New J. Chem.* **2015**, *39*, 1611–1618.
(70) Xiao, Y. N.; Zhang, C. X. Weak Nonbonded S···X (X = O, N, and S) Interactions in Proteins. Statistical and Theoretical Studies. *Bull. Chem. Soc. Jpn.* **2002**, *75*, 1611–1625.
(71) Biswal, H. S.; Sahu, A. K.; Galmés, B.; Frontera, A.; Chopra, D. Se···O/S and S···O Chalcogen Bonds in Small Molecules and Proteins: A Combined CSD and PDB Study. *ChemBioChem* **2022**, *23*, e202100498.
(72) Zauhar, R. J.; Colbert, C. L.; Morgan, R. S.; Welsh, W. J. Evidence for a Strong Sulfur-Aromatic Interaction Derived from Crystallographic Data. *Biopolymers* **2000**, *53*, 233–248.
(73) Ringer, A. L.; Senenko, A.; Sherrill, C. D. Models of S/π Interactions in Protein Structures: Comparison of the H2S–Benzene Complex with PDB Data. *Protein Sci.* **2007**, *16*, 2216.
(74) Morgan, R. S.; Tatsch, C. E.; Gushard, R. H.; Warme, P. K. Chains of Alternating Sulfur and pi-Bonded Atoms in Eight Small Proteins. *Int. J. Pept. Protein Res.* **1978**, *11*, 209–217.
(75) Reid, C.; Lindley, P. F.; Thornton, J. M. Sulphur-Aromatic Interactions in Proteins. *FEBS Lett.* **1985**, *190*, 209–213.
(76) Valley, C. C.; Cembran, A.; Perlmutter, J. D.; Lewis, A. K.; Labello, N. P.; Gao, J.; Sachs, J. N. The Methionine-Aromatic Motif Plays a Unique Role in Stabilizing Protein Structure. *J. Biol. Chem.* **2012**, *287*, 34979–34991.
(77) Tauer, T. P.; Derrick, M. E.; Sherrill, C. D. Estimates of the Ab Initio Limit for Sulfur-π Interactions: The H 2S-Benzene Dimer. *J. Phys. Chem. A* **2005**, *109*, 191–196.
(78) Pranata, J. Sulfur-Aromatic Interactions: A Computational Study of the Dimethyl Sulfide-Benzene Complex. *Bioorg. Chem.* **1997**, *25*, 213–219.
(79) Di Lello, P.; Jenkins, L. M. M.; Jones, T. N.; Nguyen, B. D.; Hara, T.; Yamaguchi, H.; Dikeakos, J. D.; Appella, E.; Legault, P.; Omichinski, J. G. Structure of the Tfb1/P53 Complex: Insights into the Interaction between the P62/Tfb1 Subunit of TFIIH and the Activation Domain of P53. *Mol. Cell* **2006**, *22*, 731–740.
(80) Biswal, H. S.; Wategaonkar, S. Sulfur, Not Too Far behind O, N, and C: SH··· π Hydrogen Bond. *J. Phys. Chem. A* **2009**, *113*, 12774–12782.
(81) Daeffler, K. N. M.; Lester, H. A.; Dougherty, D. A. Functionally Important Aromatic-Aromatic and Sulfur-π Interactions in the D2 Dopamine Receptor. *J. Am. Chem. Soc.* **2012**, *134*, 14890–14896.
(82) Chien, E. Y. T.; Liu, W.; Zhao, Q.; Katritch, V.; Han, G. W.; Hanson, M. A.; Shi, L.; Newman, A. H.; Javitch, J. A.; Cherezov, V.; Stevens, R. C. Structure of the Human Dopamine D3 Receptor in Complex with a D2/D3 Selective Antagonist. *Science* **2010**, *330*, 1091–1095.
(83) Motherwell, W. B.; Moreno, R. B.; Pavlakos, I.; Arendorf, J. R. T.; Arif, T.; Tizzard, G. J.; Coles, S. J.; Aliev, A. E. Noncovalent Interactions of π Systems with Sulfur: The Atomic Chameleon of Molecular Recognition. *Angew. Chem. Int. Ed.* **2018**, *130*, 1207–1212.
(84) Némethy, G.; Scheraga, H. A. Strong Interaction between Disulfide Derivatives and Aromatic Groups in Peptides and Proteins. *Biochem. Biophys. Res. Commun.* **1981**, *98*, 482–487.
(85) Viguera, A. R.; Serrano, L. Side-Chain Interactions between Sulfur-Containing Amino Acids and Phenylalanine in α-Helices. *Biochemistry* **1995**, *34*, 8771–8779.
(86) Tatko, C. D.; Waters, M. L. Investigation of the Nature of the Methionine-π Interaction in β-Hairpin Peptide Model Systems. *Protein Sci.* **2004**, *13*, 2515–2522.
(87) Albanese, K. I.; Waters, M. L. Contributions of Methionine to Recognition of Trimethyllysine in Aromatic Cage of PHD Domains: Implications of Polarizability, Hydrophobicity, and Charge on Binding. *Chem. Sci.* **2021**, *12*, 8900–8908.
(88) Reißner, T.; Schneider, S.; Schorr, S.; Carell, T. Crystal Structure of a Cisplatin-(1,3-GTG) Cross-

Link within DNA Polymerase η. *Angew. Chem. Int. Ed.* **2010**, *49*, 3077–3080.
(89) Albanese, K. I.; Leaver-Fay, A.; Treacy, J. W.; Park, R.; Houk, K. N.; Kuhlman, B.; Waters, M. L. Comparative Analysis of Sulfonium-π, Ammonium-π, and Sulfur-π Interactions and Relevance to SAM-Dependent Methyltransferases. *J. Am. Chem. Soc.* **2022**, *144*, 2535–2545.
(90) Biirgi, H. B.; Dunitz, J. D.; Shefter, E. Geometrical Reaction Coordinates. II. Nucleophilic Addition to a Carbonyl Group. *J. Am. Chem. Soc.* **1973**, *95*, 5065–5067.
(91) Fufezan, C. The Role of Buergi-Dunitz Interactions in the Structural Stability of Proteins. *Proteins Struct. Funct. Bioinf.* **2010**, *78*, 2831–2838.
(92) Chakrabarti, P.; Pal, D. An Electrophile-Nucleophile Interaction in Metalloprotein Structures. *Protein Sci.* **1997**, *6*, 851–859.
(93) Choudhary, A.; Gandla, D.; Krow, G. R.; Raines, R. T. Nature of Amide Carbonyl--Carbonyl Interactions in Proteins. *J. Am. Chem. Soc.* **2009**, *131*, 7244–7246.
(94) Newberry, R. W.; VanVeller, B.; Raines, R. T. Thioamides in the Collagen Triple Helix. *Chem. Commun.* **2015**, *51*, 9624–9627.
(95) Newberry, R. W.; Vanveller, B.; Guzei, I. A.; Raines, R. T. n→π* Interactions of Amides and Thioamides: Implications for Protein Stability. *J. Am. Chem. Soc.* **2013**, *135*, 7843.
(96) Newberry, R. W.; Raines, R. T. The n→π∗ Interaction. *Acc. Chem. Res.* **2017**, *50*, 1838–1846.
(97) Bartlett, G. J.; Newberry, R. W.; Vanveller, B.; Raines, R. T.; Woolfson, D. N. Interplay of Hydrogen Bonds and n →π* Interactions in Proteins. *J. Am. Chem. Soc.* **2013**, *135*, 18682–18688.
(98) Kilgore, H. R.; Raines, R. T. n→π∗ Interactions Modulate the Properties of Cysteine Residues and Disulfide Bonds in Proteins. *J. Am. Chem. Soc.* **2018**, *140*, 17606–17611.
(99) Bartlett, G. J.; Choudhary, A.; Raines, R. T.; Woolfson, D. N. n→π* Interactions in Proteins. *Nat. Chem. Biol.* **2010**, *6*, 615–620.
(100) Newberry, R. W.; Bartlett, G. J.; VanVeller, B.; Woolfson, D. N.; Raines, R. T. Signatures of n→π* Interactions in Proteins. *Protein Sci.* **2014**, *23*, 284–288.
(101) Jeffrey, G. A.; Mitra, J.; Houk, K. N.; Rondan, N. G.; Paddon-Row, M. N. Pyramidalization of Carbonyl Carbons in Asymmetric Environments: Carboxylates, Amides, and Amino Acids. *J. Am. Chem. Soc.* **1985**, *107*, 321–326.
(102) Esposito, L.; Vitagliano, L.; Zagari, A.; Mazzarella, L. Pyramidalization of Backbone Carbonyl Carbon Atoms in Proteins. *Protein Sci.* **2000**, *9*, 2038.
(103) Shoulders, M. D.; Raines, R. T. Collagen Structure and Stability. *Annu. Rev. Biochem.* **2009**, *78*, 929-958.
(104) Fomenko, D. E.; Gladyshev, V. N. Identity and Functions of CxxC-Derived Motifs. *Biochemistry* **2003**, *42*, 11214–11225.
(105) Becke, A. D. Density-functional Thermochemistry. III. The Role of Exact Exchange. *J. Chem. Phys.* **1998**, *98*, 5648.
(106) Chai, J. Da; Head-Gordon, M. Long-Range Corrected Hybrid Density Functionals with Damped Atom-Atom Dispersion Corrections. *Phys. Chem. Chem. Phys.* **2008**, *10*, 6615–6620.
(107) Zhao, Y.; Truhlar, D. G.; Zhao, Y.; Truhlar, · D G. The M06 Suite of Density Functionals for Main Group Thermochemistry, Thermochemical Kinetics, Noncovalent Interactions, Excited States, and Transition Elements: Two New Functionals and Systematic Testing of Four M06-Class Functionals and 12 Other Function. *Theor. Chem. Acc.* **2007**, *120*, 215–241.
(108) Zhao, Y.; Truhlar, D. G. Density Functionals with Broad Applicability in Chemistry. *Acc. Chem. Res.* **2008**, *41*, 157–167.
(109) Mardirossian, N.; Head-Gordon, M. How Accurate Are the Minnesota Density Functionals for Noncovalent Interactions, Isomerization Energies, Thermochemistry, and Barrier Heights Involving Molecules Composed of Main-Group Elements? *J. Chem. Theory Comput.* **2016**, *12*, 4303–4325.
(110) Vorontsov, A. V.; Smirniotis, P. G. Benchmarking Semiempirical and DFT Methods for the Interaction of Thiophene and Diethyl Sulfide Molecules with a $Ti(OH)_4(H2O)$ Cluster. *J. Mol. Model.* **2017**, *23*, 223.
(111) Adamo, C.; Barone, V. Toward Reliable Density Functional Methods without Adjustable

Parameters: The PBE0 Model. *J. Chem. Phys.* **1999**, *110*, 6158.
(112) Grimme, S.; Ehrlich, S.; Goerigk, L. Effect of the Damping Function in Dispersion Corrected Density Functional Theory. *J. Comput. Chem.* **2011**, *32*, 1456–1465.
(113) Tsuzuki, S.; Uchimaru, T. Accuracy of Intermolecular Interaction Energies, Particularly Those of Hetero-Atom Containing Molecules Obtained by DFT Calculations with Grimme's D2, D3 and D3BJ Dispersion Corrections. *Phys. Chem. Chem. Phys.* **2020**, *22*, 22508–22519.
(114) Grimme, S.; Antony, J.; Ehrlich, S.; Krieg, H. A Consistent and Accurate Ab Initio Parametrization of Density Functional Dispersion Correction (DFT-D) for the 94 Elements H-Pu. *J. Chem. Phys.* **2010**, *132*, 154104.
(115) Nikoo, S. Computational Insights into Bio-Relevant Sulfur Chemistry. Ph.D. Thesis, University of Windsor, Ontario, Canada, 2019.
(116) Biswal, H. S.; Bhattacharyya, S.; Bhattacherjee, A.; Wategaonkar, S. Nature and Strength of Sulfur-Centred Hydrogen Bonds: Laser Spectroscopic Investigations in the Gas Phase and Quantum-Chemical Calculations. *Int. Rev. Phys. Chem.* **2015**, *34*, 99–160.
(117) Morgado, C. A.; McNamara, J. P.; Hillier, I. H.; Burton, N. A.; Vincent, M. A. Density Functional and Semiempirical Molecular Orbital Methods Including Dispersion Corrections for the Accurate Description of Noncovalent Interactions Involving Sulfur-Containing Molecules. *J. Chem. Theory Comput.* **2007**, *3*, 1656–1664.
(118) Sharma, J.; Champagne, P. A. Benchmark of Density Functional Theory Methods for the Study of Organic Polysulfides. *J. Comput. Chem.* **2022**, *43*, 2131.
(119) Mintz, B. J.; Parks, J. M. Benchmark Interaction Energies for Biologically Relevant Noncovalent Complexes Containing Divalent Sulfur. *J. Phys. Chem. A* **2012**, *116*, 46.
(120) Aeberhard, P. C.; Arey, J. S.; Lin, I.-C. C.; Rothlisberger, U. Accurate DFT Descriptions for Weak Interactions of Molecules Containing Sulfur. *J. Chem. Theory Comput.* **2009**, *5*, 23–28.
(121) Riley, K. E.; Hobza, P. Noncovalent Interactions in Biochemistry. *Wiley Interdiscip. Rev. Comput. Mol. Sci.* **2011**, *1*, 3–17.
(122) Raghavachari, K.; Trucks, G. W.; Pople, J. A.; Head-Gordon, M. A Fifth-Order Perturbation Comparison of Electron Correlation Theories. *Chem. Phys. Lett.* **1989**, *157*, 479–483.
(123) Von Lilienfeld, O. A.; Tavernelli, I.; Rothlisberger, U.; Sebastiani, D. Optimization of Effective Atom Centered Potentials for London Dispersion Forces in Density Functional Theory. *Phys. Rev. Lett.* **2004**, *93*, 153004.
(124) Lin, I. C.; Coutinho-Neto, M. D.; Felsenheimer, C.; Von Lilienfeld, O. A.; Tavernelli, I.; Rothlisberger, U. Library of Dispersion-Corrected Atom-Centered Potentials for Generalized Gradient Approximation Functionals: Elements H, C, N, O, He, Ne, Ar, and Kr. *Phys. Rev. B - Condens. Matter Mater. Phys.* **2007**, *75*, 205131.
(125) Weigend, F.; Ahlrichs, R. Balanced Basis Sets of Split Valence, Triple Zeta Valence and Quadruple Zeta Valence Quality for H to Rn: Design and Assessment of Accuracy. *Phys. Chem. Chem. Phys.* **2005**, *7*, 3297–3305.
(126) Weigend, F. Accurate Coulomb-Fitting Basis Sets for H to Rn. *Phys. Chem. Chem. Phys.* **2006**, *8*, 1057–1065.
(127) Dunning, T. H. Gaussian Basis Sets for Use in Correlated Molecular Calculations. I. The Atoms Boron through Neon and Hydrogen. *J. Chem. Phys.* **1998**, *90*, 1007.
(128) Kendall, R. A.; Dunning, T. H.; Harrison, R. J. Electron Affinities of the First-row Atoms Revisited. Systematic Basis Sets and Wave Functions. *J. Chem. Phys.* **1998**, *96*, 6796.
(129) Dunning, J.; Peterson, K. A.; Wilson, A. K. Gaussian Basis Sets for Use in Correlated Molecular Calculations. X. The Atoms Aluminum through Argon Revisited. *J. Chem. Phys.* **2001**, *114*, 9244–9253.
(130) Wilson, A. K.; Dunning, T. H. The HSO−SOH Isomers Revisited: The Effect of Tight d Functions†. *J. Phys. Chem. A* **2004**, *108*, 3129–3133.
(131) Bell, R. D.; Wilson, A. K. SO3 Revisited: Impact of Tight d Augmented Correlation Consistent Basis Sets on Atomization Energy and Structure. *Chem. Phys. Lett.* **2004**, *394*, 105–109.

(132) Boys, S. F.; Bernardi, F. The Calculation of Small Molecular Interactions by the Differences of Separate Total Energies. Some Procedures with Reduced Errors. *Mol. Phys.* **1970**, *19*, 553–566.
(133) Garden, A. L.; Lane, J. R.; Kjaergaard, H. G. Counterpoise Corrected Geometries of Hydrated Complexes. *J. Chem. Phys.* **2006**, *125*, 144317.
(134) Plumley, J. A.; Dannenberg, J. J. A Comparison of the Behavior of Functional/Basis Set Combinations for Hydrogen-Bonding in the Water Dimer with Emphasis on Basis Set Superposition Error. *J. Comput. Chem.* **2011**, *32*, 1519–1527.
(135) Pohl, G.; Plumley, J. A.; Dannenberg, J. J. The Interactions of Phenylalanines in β-Sheet-like Structures from Molecular Orbital Calculations Using Density Functional Theory (DFT), MP2, and CCSD(T) Methods. *J. Chem. Phys.* **2013**, *138*, 245102.
(136) Wu, W.; Kieffer, J. New Hybrid Method for the Calculation of the Solvation Free Energy of Small Molecules in Aqueous Solutions. *J. Chem. Theory Comput.* **2019**, *15*, 371–381.
(137) Zhang, J.; Zhang, H.; Wu, T.; Wang, Q.; Van Der Spoel, D. Comparison of Implicit and Explicit Solvent Models for the Calculation of Solvation Free Energy in Organic Solvents. *J. Chem. Theory Comput.* **2017**, *13*, 1034–1043.
(138) Sure, R.; el Mahdali, M.; Plajer, A.; Deglmann, P. Towards a Converged Strategy for Including Microsolvation in Reaction Mechanism Calculations. *J. Comput. Aided. Mol. Des.* **2021**, *35*, 473–492.
(139) Warshel, A.; Levitt, M. Theoretical Studies of Enzymic Reactions: Dielectric, Electrostatic and Steric Stabilization of the Carbonium Ion in the Reaction of Lysozyme. *J. Mol. Biol.* **1976**, *103*, 227–249.
(140) Estrada-Tejedor, R.; Ros-Blanco, L.; Closa, J. T. Multiscale Modeling for Complex Chemical Systems: Highlights about the Nobel Prize in Chemistry 2013. *Afinidad* **2014**, *71*, 89–94.
(141) Yan, X. C.; Robertson, M. J.; Tirado-Rives, J.; Jorgensen, W. L. Improved Description of Sulfur Charge Anisotropy in OPLS Force Fields: Model Development and Parameterization. *J. Phys. Chem. B* **2017**, *121*, 6626–6636.
(142) Svensson, M.; Humbel, S.; Froese, R. D. J.; Matsubara, T.; Sieber, S.; Morokuma, K. ONIOM: A Multilayered Integrated MO + MM Method for Geometry Optimizations and Single Point Energy Predictions. A Test for Diels-Alder Reactions and Pt(P(t-Bu)3)2 + H2 Oxidative Addition. *J. Phys. Chem.* **1996**, *100*, 19357–19363.
(143) Chung, L. W.; Sameera, W. M. C.; Ramozzi, R.; Page, A. J.; Hatanaka, M.; Petrova, G. P.; Harris, T. V.; Li, X.; Ke, Z.; Liu, F.; Li, H. B.; Ding, L.; Morokuma, K. The ONIOM Method and Its Applications. *Chem. Rev.* **2015**, *115*, 5678–5796.
(144) Ahmadi, S.; Barrios Herrera, L.; Chehelamirani, M.; Hostaš, J.; Jalife, S.; Salahub, D. R. Multiscale Modeling of Enzymes: QM-Cluster, QM/MM, and QM/MM/MD: A Tutorial Review. *Int. J. Quantum Chem.* **2018**, *118*, e25558.
(145) Magalhães, R. P.; Fernandes, H. S.; Sousa, S. F. Modelling Enzymatic Mechanisms with QM/MM Approaches: Current Status and Future Challenges. *Isr. J. Chem.* **2020**, *60*, 655–666.

2.2 Importance of Noncovalent Interactions Involving Sulfur Atoms in Thiopeptide Antibiotics – Glycothiohexide α and Nocathiacin I

This chapter is adapted with slight modifications with permission from Kojasoy, V.; Tantillo, D. J. Importance of Noncovalent Interactions Involving Sulfur Atoms in Thiopeptide Antibiotics–Glycothiohexide α and Nocathiacin I. *J. Phys. Chem. A* **2023**, *127*, 2081–2090.

2.2.1 Abstract

Noncovalent interactions involving sulfur atoms play essential roles in protein structure and function by significantly contributing to protein stability, folding and biological activity. Sulfur is a highly polarizable atom that can participate in many types of noncovalent interactions including hydrogen bonding, sulfur–π interactions, and S–lone pair interactions, but the impact of these sulfur-based interactions on molecular recognition and drug design is still often underappreciated. Here we examine, using quantum chemical calculations, the roles of sulfur-based noncovalent interactions in complex naturally occurring molecules representative of thiopeptide antibiotics: glycothiohexide α and its close structural analogue nocathiacin I. While donor-acceptor orbital interactions make only very small contributions, electrostatic and dispersion contributions are predicted to be significant in many cases. In pursuit of understanding the magnitudes and nature of these noncovalent interactions, we happened upon potential structural modifications that could significantly expand the chemical space of effective thiopeptide antibiotics.

2.2.2 Introduction

Thiopeptide antibiotics are sulfur-containing, structurally complex natural products of ribosomal origin that inhibit protein synthesis in bacteria.[1–4] In 1948, the first thiopeptide antibiotic, micrococcin, was isolated from sewage waters of Oxford.[5] Thiostrepton, perhaps the most prominent member of the thiopeptide family of antibiotics, was isolated in 1954,[6–8] followed by the discovery of a variety of others. The highly modified macrocyclic thiopeptides are classified into five series (*a*-*e*) based on the oxidation state of their

six-membered nitrogen heterocycle (Figure 2.2.1, red). All show almost no activity against Gram-negative bacteria but are highly active against Gram-positive bacteria.[1–4] Thiopeptide antibiotics have inspired medicinal chemists for decades. For instance, the thiopeptides thiostrepton and siomycin function as anticancer agents by stimulating the apoptosis of cancer cells without disrupting normal cells.[9–13] The thiopeptide cyclothiazomycin A inhibits human renin,[14–16] which plays a regulatory role in controlling blood pressure. The thiopeptide cyclothiazomycin B1 shows antifungal activity associated with its binding to the fungal cell wall chitin,[17] as well as playing a functional role in inhibiting RNA polymerase.[18] The thiopeptides nosiheptide and thiostrepton are used as veterinary pharmaceuticals.[19,20] In addition, thiostrepton and derivatives target parasite proteasomes and the apicoplast and exhibit antiparasitic activity,[21] and thiostrepton can induce *tipA* promotion.[22]

Here we explore the importance of sulfur atoms to the 3-dimensional structures of such molecules using the tools of modern computational quantum chemistry. Are the sulfur atoms essential? If sulfur atoms could be replaced by other groups without changing the overall shape and electrostatic profile of such compounds, the chemical space of potential antibiotics could be increased. Such chemical replacements also could be used to advantage to modulate properties such as solubility and metabolism.

Noncovalent interactions (NCIs)[23] involving sulfur atoms play crucial roles in protein structure and function by significantly contributing to protein and peptide stability, folding, binding, and chemical reactivity.[24] These interactions also modulate the conformational preferences of small molecules, including medicinally relevant compounds.[25,26] Sulfur, as a highly polarizable atom, is involved in many important interactions such as hydrogen bonding, sulfur-lone pair interactions with heteroatoms, and interactions with π-systems.[24,25,34–36,26–33] Sulfur-lone pair interactions have been shown to play key roles in determining the conformations of many small molecules, potentially allowing S•••X units to function as less polar isosteres

for NH•••X units in drugs.[26,37–39] Although most noncovalent interactions involving sulfur are considered to be weak, their cumulative effect can be large.[40]

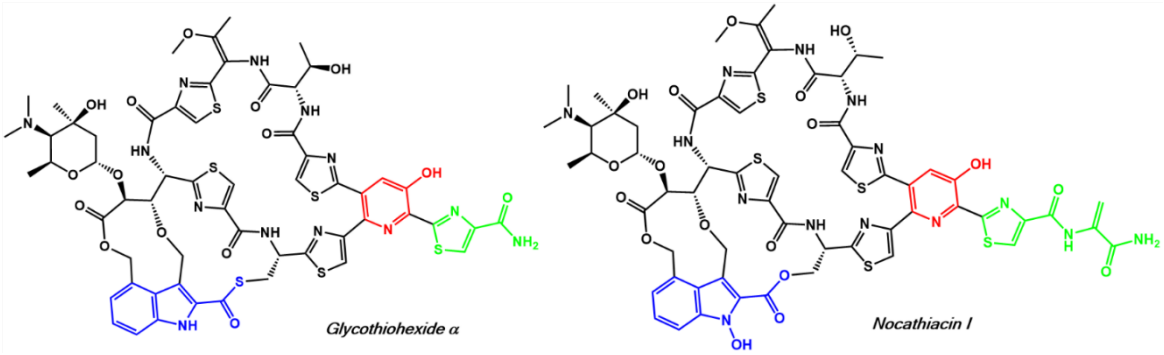

Figure 2.2.1. The structures of *e* series thiopeptides glycothiohexide α and nocathiacin I. The six-membered nitrogen heterocycle that determines the class of the thiopeptides is shown in red. The structural differences between glycothiohexide α and nocathiacin I are shown in blue and green.

As representative examples of thiopeptide antibiotics, we investigated glycothiohexide α and its close structural analogue nocathiacin I (Figure 2.2.1), both of which are highly potent against Gram-positive bacteria, including multidrug-resistant strains, and share substructures with both small drugs and proteins.[1,4,41] Glycothiohexide α was discovered while screening for antibiotics active against bacteria derived from clinical specimens resistant to vancomycin and methicillin.[42–44] It was isolated from the fermentation of a Sebekia species, and shows excellent in vitro activity, inhibiting bacterial growth.[42–44] However, it has low in vivo activity due to its poor solubility.[3,42–44] Similarly, nocathiacin I, isolated from the cultured broth of Nocardia sp., is highly potent against Gram-positive bacteria both in vivo and in vitro.[45–48]

We aimed to determine the strength of important intramolecular noncovalent interactions involving sulfur atoms in these molecules with quantum chemical tools, and characterize how they contribute to overall structure. Since universal agreement on the most effective means of quantifying the contributions of particular NCIs is lacking, especially intramolecular NCIs,[49–51] we applied multiple methods, cognizant

of the deficiencies of each and aiming for qualitative conclusions that are still useful for forward design. We conducted noncovalent interaction (NCI) analysis[52] to visualize the regions of noncovalent interactions. To assess orbital contributions, we performed natural bond orbital (NBO) analysis.[53] We also carried out symmetry-adapted perturbation theory (SAPT) analysis to partition stabilization energies into physically meaningful (electrostatic, exchange, induction, and dispersion) components.[54,55] Furthermore, to probe the uniqueness of sulfur atoms (and therefore their potential for being replaced), we switched the sulfur atoms present in glycothiohexide α and nocathiacin I to methylene groups and performed comparative analyses.

2.2.3 Methods

All geometry optimizations were carried out with Gaussian 16[56] using density functional theory (DFT) at the M06-2X/6-31G* level of theory.[57–59] NMR calculations[60] were performed with SMD(DMSO)-mPW1PW91/6-311+G(2d,p)//M06-2X/6-31G*[57–59,61,62] using the GIAO method[63–66] with Gaussian 16. We used linear regression to generate chemical shifts in which computed NMR isotropic shielding constants were plotted against experimental chemical shifts.[60] The slope and the intercept (scaling factors) of the resulting best fit line were used to convert the computed isotropic shielding constants (σ) into chemical shifts (δ).

$$\delta = \frac{intercept - \sigma}{-slope}$$

For our analyses, we calculated separate scaling factors for the lowest energy conformers of glycothiohexide α and nocathiacin I at the SMD(DMSO)-mPW1PW91/6-311+G(2d,p)//M06-2X/6-31G* level. Natural bond orbital (NBO) calculations were performed with NBO, version 3.1[67] implemented in Gaussian 16. Noncovalent interaction (NCI)[52] analysis and domain analysis were carried out with Multiwfn.[68] Symmetry-adapted perturbation theory (SAPT)[54] analysis was performed at the fiSAPT0/jun-cc-pVDZ//M06-2X/6-31G* level[69–74] using Psi4, version 1.4.[75] Electrostatic potential surfaces[76,77] were rendered with Gaussview 6.0. CLogP values were generated with BioByte within ChemDraw version 21.0.

2.2.4 Results and Discussion

2.2.4.1 Conformations

We started our analysis with a conformational search. We referred to a reported structure of nocathiacin I[78] to build an initial guess for its close structural analogue glycothiohexide α. A relevant study by Leet and co-workers[45] defined the absolute configuration of nocathiacin I by NMR studies and chiral capillary electrophoresis.[79] We ran conformational searches (using CREST, version 2.11.1; see SI) on both nocathiacin I and glycothiohexide α and proceeded with the resulting dominant conformers (Figure 2.2.2). Note that the conformers we obtained had significant deviations between their predicted and experimental proton chemical shifts (see SI for details).[44,47,60,80–84] However, examination of conformers from our search and a different conformer previously reported for nocathiacin I[85] indicated that proton chemical shifts varied greatly with conformation. This variation is, perhaps, not surprising, given previous work on cyclic peptide NMR.[86,87] Based on our results, it is not clear that the previously reported conformations actually represent the dominant conformations in solution, nor do the ones we discuss below, although all of these are likely energetically accessible. Resolving this issue is beyond the current study, however, which is aimed at assessing the impact of *potential* noncovalent interactions involving sulfur. The results for specific interactions described below should be generally transferrable to other conformations with similar

geometries (given the distance dependences of the interactions described and the associated expectations regarding modulation from surrounding groups).

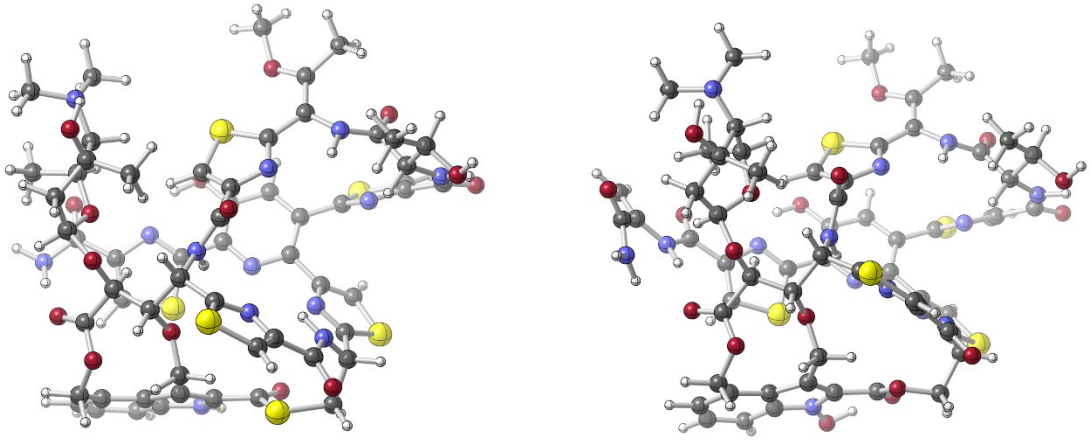

Figure 2.2.2. 3D structures of the lowest energy conformers of glycothiohexide α and nocathiacin I.

2.2.4.2 NCI Analysis

NCI analysis is a powerful technique to investigate the types and strength of noncovalent interactions using the reduced density gradient.[88] To identify the strengths of noncovalent interactions, the second derivatives of the density are used. The different types of interactions are visualized by color on isosurfaces in which blue, green and red represent strong attraction (e.g., hydrogen bonding, halogen bonding etc.), weak attraction (e.g., dispersion interactions), and strong repulsion (e.g., steric clashes, lone pair-lone pair repulsion), respectively.[52,88,89]

To visualize the regions of noncovalent interactions involving sulfur atoms, gradient isosurfaces of glycothiohexide α and nocathiacin I were generated (Figure 2.2.3). Many different noncovalent interactions are present for both of these complex molecules. The regions involving sulfur atoms (yellow spheres) are mostly green, which indicates weak attractive interactions, the origins of which are discussed below (see SI for additional domain-based analyses).

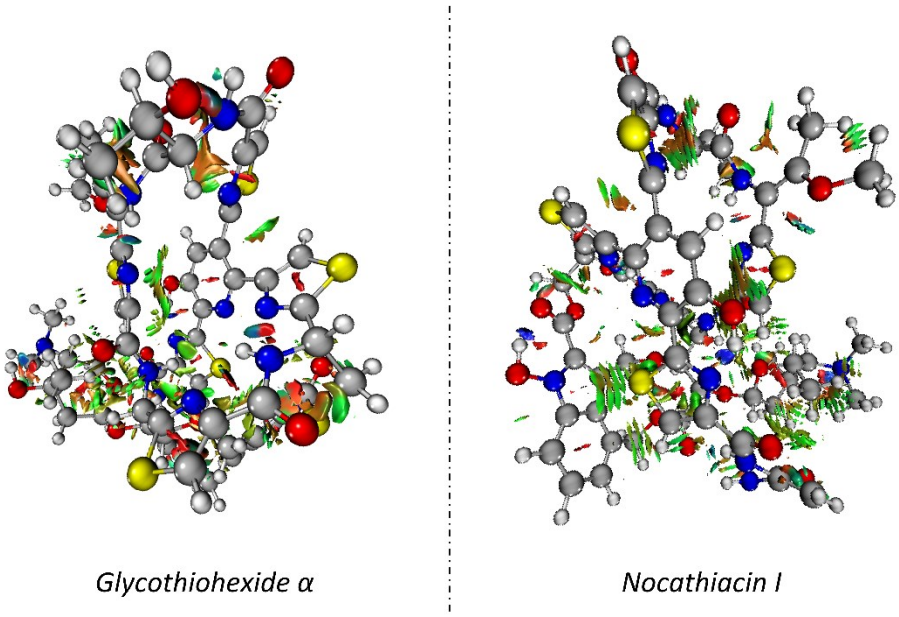

Figure 2.2.3. Gradient isosurfaces of glycothiohexide α and nocathiacin I (reduced density gradient = 0.5 a.u., electron density < 0.05 a.u). Blue, green, and red areas denote strong attraction, weak attraction, and strong repulsion, respectively.

2.2.4.3 NBO Analysis

To characterize the key sulfur-lone pair donor-acceptor orbital interactions, we calculated the corresponding second-order perturbation NBO energies ($E^{(2)}$). Only $E^{(2)}$orbital energies above a 0.1 kcal mol^{-1} threshold are reported. In Figure 2.2.4, the regions with key sulfur-based interactions are highlighted. Each color represents a different type of donor-acceptor interaction. For glycothiohexide α (Figure 2.2.4, left) the $E^{(2)}$ NBO energies for $n_S \rightarrow \sigma^*_{O\text{-}C}$ (in blue), $n_S \rightarrow \sigma^*_{C\text{-}O}$ (in green), and $n_S \rightarrow \sigma^*_{N\text{-}H}$ (in light pink) interactions are all ~0.2 kcal mol^{-1}. Although the magnitudes of these interaction energies are low, multiple such interactions contribute to the overall thermodynamic stability of the compounds in question.[40] The first of these interactions is a sulfur-lone pair interaction. Sulfur-lone pair interactions play important roles in a variety of biochemical processes.[25,29,31,90–94] A special interaction (in light orange) to be noted is the $n_S \rightarrow \pi^*_{C=O}$ interaction (~2.0 kcal mol^{-1}), which is oriented approximately along the Bürgi-Dunitz

trajectory.[95,96] Studies by Raines and co-workers have highlighted the importance of such $n \rightarrow \pi^*$ interactions in protein folding and structure, including cases with sulfur lone pairs.[27,28,30,34–36,97–99] For nocathiacin I (Figure 2.2.4, right) similar $n_S \rightarrow \sigma^*_{O\text{-}C}$ (in blue), and $n_S \rightarrow \sigma^*_{C\text{-}O}$ (in green) interactions are observed. The $n \rightarrow \pi^*$ interaction from the sulfur lone-pair to the imine group contributes 0.3 kcal mol^{-1} (in yellow). The interaction of two sulfur atoms ($S_{(1)}$ and $S_{(2)}$) of two nearby thiazole rings can be compared. While the lone-pair of the $S_{(2)}$ atom interacts with the $\sigma^*_{C\text{-}H}$ orbital of the opposing thiazole ring (0.3 kcal mol^{-1}, in grey); the lone-pair of the $S_{(1)}$ atom does not participate in any significant orbital interaction as a result of its orientation.

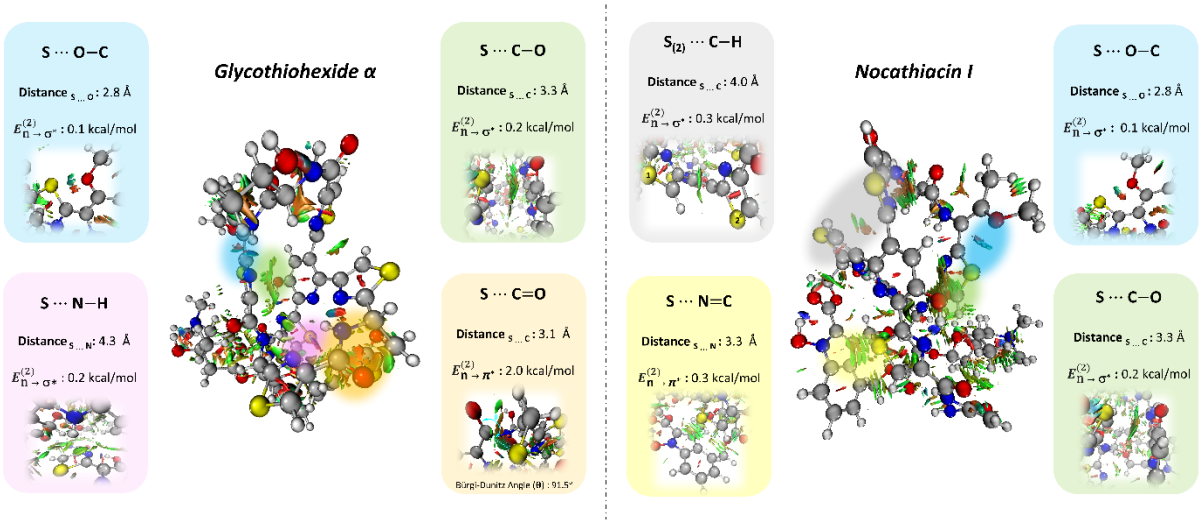

Figure 2.2.4. The second-order perturbation energies above the 0.1 kcal mol^{-1} threshold ($E^{(2)}$) corresponding to NBOs in each key sulfur lone-pair interaction regions (color-coded) of glycothiohexide α (left) and nocathiacin I (right).

2.2.4.4 fiSAPT Analysis

SAPT is a widely used technique for characterizing noncovalent interactions.[54,55] We used the SAPT method to partition the stabilization energy associated with the sulfur-based noncovalent interactions into electrostatic, exchange (steric repulsion), induction, and dispersion components. Functional-group intramolecular SAPT (fiSAPT) enables pairwise energy decomposition between individual noncovalent contacts and allows for the analysis in intramolecular systems by Hartree-Fock embedding.[73] For the SAPT

analysis, we truncated glycothiohexide α, and nocathiacin I into key interaction regions (Figure 2.2.5, top). Since our analysis is based on truncated models, our SAPT results provide only a qualitative description of the energetic ordering of the individual energy components. For a typical energy decomposition analysis, one needs two fragments.

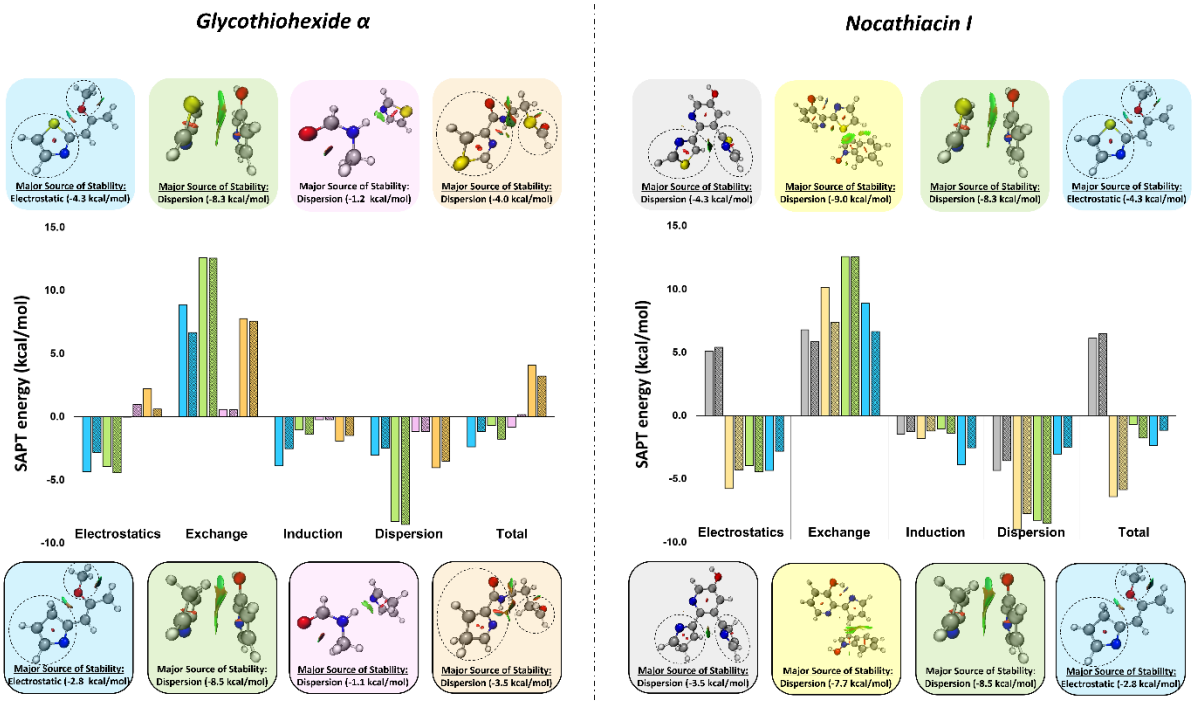

Figure 2.2.5. Calculated (fiSAPT0/jun-cc-pVDZ//M06-2X/6-31G*) total and decomposed energies (kcal mol^{-1}) for the colored interactions in the truncated regions of glycothiohexide α (top left), and nocathiacin I (top right). We made modified models of glycothiohexide α (bottom left), and nocathiacin I (bottom right) by switching S atoms with CH_2. The pictures of the new models (same color-code with the original models) are in black borders.

However, in intramolecular systems, the challenging process of inter-fragment partitioning, involving defining two fragments that are covalently linked by third unit, is required. A caveat is that fiSAPT allows for cutting through σ bonds only. Fragmenting through π bonds or inherently delocalized systems is not advised.[71] For the intramolecular systems studied (Figure 2.2.5, blue, light orange and grey),

the circled groups are our user-defined functional groups separated by a linker unit for the fiSAPT analysis. We confirmed the validity of our user-defined functional groups by checking the completeness of atomic orbital charges.[71] We also probed different fragmentation patterns, and defined smaller groups as functional groups for fiSAPT analysis. However, the conclusions changed drastically, as expected, due to the delocalization of charges between neighboring groups (see SI for details). Based on our analysis of glycothiohexide α (Figure 2.2.5, left panel, top), the key favorable interactions are dominated by dispersion forces, but in different magnitudes due to geometry and chemical environment. For instance, the dispersion interaction between the thiazole and the amide (light pink), contributes 1.2 kcal mol^{-1} whereas the same source of stability also dominates in the amide and the thioester interaction (light orange), but contributing 4.0 kcal mol^{-1}. For nocathiacin I (Figure 2.2.5, right panel, top), the dispersion interaction between two thiazole rings (grey) contributes 4.3 kcal mol^{-1} whereas the magnitude doubles for the pyridinol-thiazole interaction (yellow). Since glycothiohexide α and nocathiacin I are structural analogues, we would expect similar interactions to be present in these two molecules. Indeed, they both contain the thiazole-methoxy (blue) and thiazole-pyridinol (green) interactions, which are primarily dominated by electrostatics and dispersion, respectively.

2.2.4.5. New Models – Isosteric Substitution of Sulfur Atoms with Methylene Groups

There has been an ongoing effort to develop thiopeptide derivatives with improved pharmacological properties (i.e., aqueous solubility, metabolic stability). Among other strategies,[4] a widely used modification is tail degradation. A study by Naidu et al. showed that the tail functionalization of nocathiacin I enhances solubility and does not compromise potency.[100] This group also described other derivatives of nocathiacin I involving modifications at the indole and/or pyridine hydroxyl groups, and products of Michael addition of amines and thiols to the dehydroalanine moiety.[101–104] Myers et al.'s study on the tail modification of thiostrepton revealed steric and spatial limitations associated with retaining bioactivity.[105] Here we consider a fundamentally different approach to thiopeptide modification – replacement of sulfur atoms with methylene groups.

Others have examined the replacement of sulfur atoms in biomolecules. For example, Meinander et al. showed that the replacement of disulfide bridges with hydrocarbon linkers (alkane and alkene) drastically improved the stability and activity of kallikrein-related peptidase 3 (KLK3).[106,107] Stymiest et al. synthesized oxytocin analogues by replacing disulfide bridges with methylene and methine groups and noticed an increase in their metabolic stability.[108] They also observed very similar geometries upon overlaying oxytocin and its analogue in which its disulfide is replaced with a *cis*-alkene.[108,109]

To further explore the role of sulfur atoms in our systems, we switched sulfur atoms with methylene groups and optimized the resulting structures. We expected this switch to have a minimal effect on structure, since sulfur and carbon have similar electronegativities. It turned out that the optimized geometries of the glycothiohexide α, and nocathiacin I nearly perfectly matched their respective structural analogues with all sulfur atoms replaced by CH_2 groups (Figure 2.2.6). Moreover, the original and modified models have very similar electrostatic potential surfaces, which can be thought of as the electrostatic profile that these molecules present to the outside world (i.e., solvent, protein binding sites, etc.). While conformational searches on both of the modified (S → CH_2) systems produced lowest energy conformers with different geometries (see SI for details), multiple conformations are energetically viable and the changes made here are extreme – no one would actually change all of the sulfur atoms at once. In addition, what matters most is whether or not the bio-active conformer is energetically accessible, which is difficult to assess without a structure of the parent peptide bound to its target.

Despite the ostensible severity of the modifications we made – wholesale swapping of all sulfurs for methylenes – the major sources of stabilizing interactions were conserved (Figure 2.2.5). A switch from sulfur to methylene groups does not change the type of noncovalent interaction that contributes most in these modified structures, but it affects the magnitude of stabilization energies. For instance, in glycothiohexide α both the original (Figure 2.2.5, left panel, top, blue) and the modified (Figure 2.2.5, left panel, bottom, blue) systems are dominated by electrostatics, however the magnitude of stabilization in the

original system is greater than in the modified system by 1.5 kcal mol^{-1}. The same trend is observed in each case studied where sulfur atoms are switched with methylene groups.

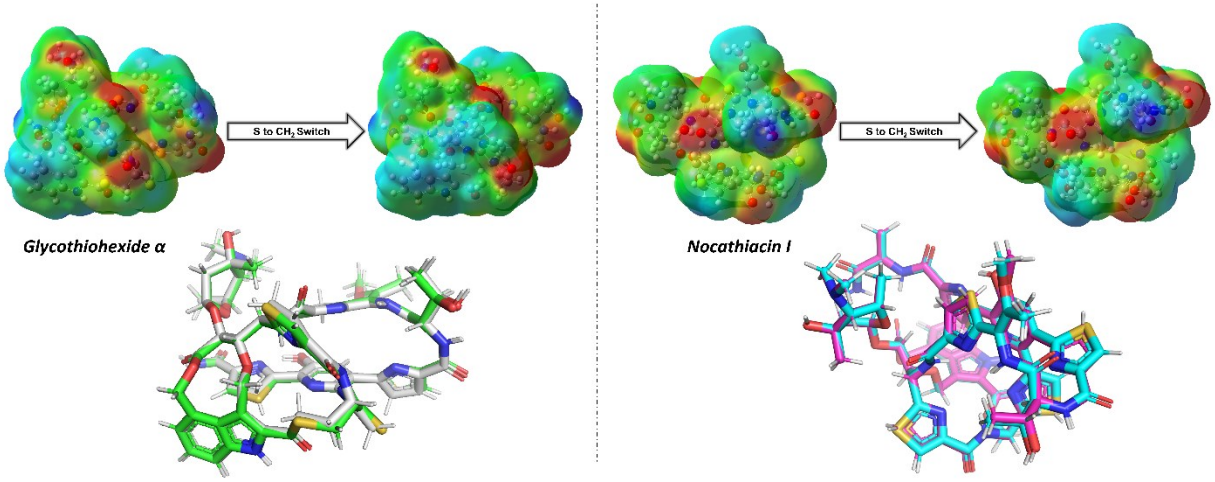

Figure 2.2.6. Comparison of the original and modified versions of glycothiohexide α (top left), and nocathiacin I (top right). At the top left: ESP map of glycothiohexide α, and its modified version; at the top right: ESP map of nocathiacin I, and its modified version. (Color range for ESP maps: $-4.654e^{-2}$ to $4.654e^{-2}$ with isovalue = 0.0004). At the bottom left: superimposed images (rmsd: 0.148) of glycothiohexide α (in green) and its modified version (in gray); at the bottom right: superimposed images (rmsd: 0.085) of nocathiacin I (in cyan) and its modified version (in magenta).

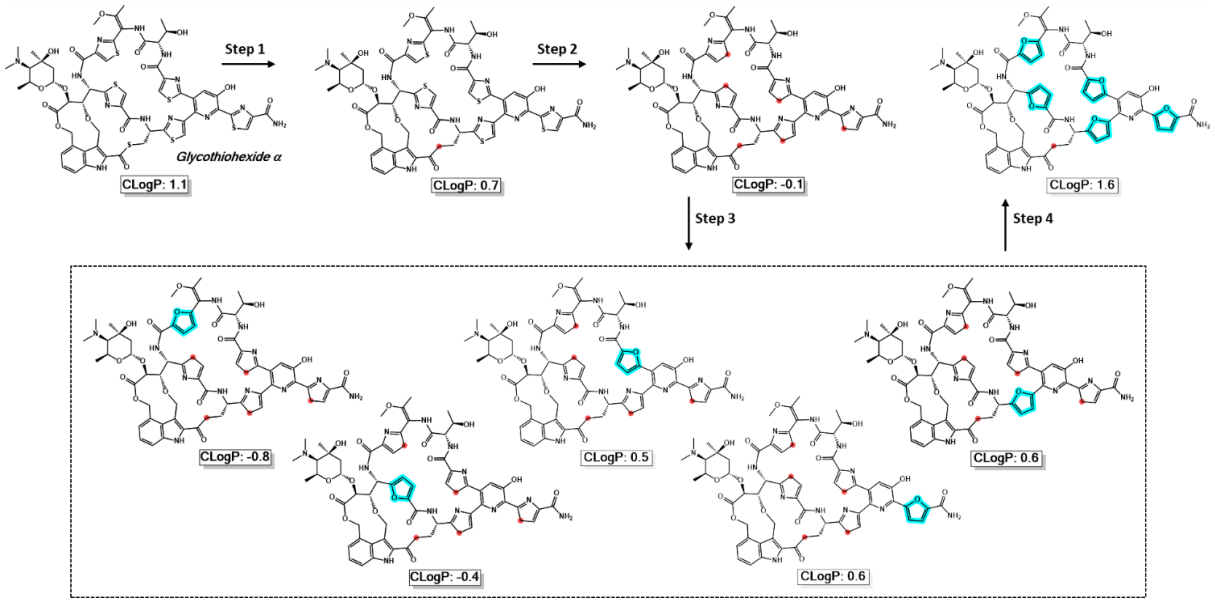

Figure 2.2.7. CLogP values throughout the bioisosteric replacement of sulfur atoms with methylene groups followed by the replacement of methylene-replaced thiazoles with furans in glycothiohexide α. The modifications are highlighted in red and cyan for the replacement of sulfur atoms with methylene groups and methylene-replaced thiazoles with furans, respectively.

We also estimated the logP (CLogP) values for the natural and S → CH_2 modified thiopeptides (Figure 2.2.7).[110] Glycothiohexide α contains six sulfur atoms: five in thiazole rings and one as a part of cysteine (Cys) residue. For our logP calculations we switched the sulfur atoms with methylene groups in two steps. In step 1, we only switched the sulfur of Cys. The logP value dropped by a considerable amount even after a single sulfur exchange.[110] As we substituted all the sulfur atoms with methylene groups (step 2), the logP value became negative, indicating increased solubility in water. Of course, modifying the thiazole rings in the manner described here is not likely to be done synthetically, but related changes could be made. For instance, when methylene-replaced thiazoles are modified into furans, the logP value varied (step 3 and step 4). Similar trends were observed for nocathiacin I (see SI for details). While standard methods for predicting logP come with significant error bars, the potential of swapping sulfur atoms for hydrocarbon groups as a means of modulating aqueous solubility, which is a problem inherent in many

thiopeptide antibiotics, without disturbing their structures and binding seems to warrant further investigation.

2.2.5 Conclusions

Noncovalent interactions involving sulfur atoms are prevalent in biological systems and serve as important control elements for structure and stability. With computational analyses, we examined the roles of such interactions in the thiopeptide antibiotics glycothiohexide α, and nocathiacin I. We also modified the sulfur atoms of glycothiohexide α and nocathiacin I to methylene groups, obtaining similar geometries and sources of stabilizing interactions. While donor-acceptor orbital interactions generally make very small contributions, electrostatic and dispersion contributions are significant in many cases. Based on CLogP estimates, these modifications may improve the aqueous solubility of these thiopeptides, and open new avenues for exploring new regions of chemical space in pursuit of compounds with different compositions but similar shapes. We hope that our computational analysis and predictions will help define what is possible in expanding the chemical space of effective thiopeptide antibiotics.

2.2.6 Acknowledgements

Support from the NSF XSEDE program is gratefully acknowledged.

2.2.7 Supporting Information

The supporting information is available free of charge at https://pubs.acs.org/doi/10.1021/acs.jpca.2c07600. Domain analysis; fiSAPT analysis; energies, frequencies, and coordinates of computed structures; computational NMR data; conformational analysis; and CLog*P* data (PDF)

2.2.8 References

(1) Bagley, M. C.; Dale, J. W.; Merritt, E. A.; Xiong, X. Thiopeptide Antibiotics. *Chem. Rev.* **2005**, *105*, 685–714.

(2) Just-Baringo, X.; Albericio, F.; Álvarez, M. Thiopeptide Antibiotics: Retrospective and Recent Advances. *Mar. Drugs* **2014**, *12*, 317–351.

(3) Shen, X.; Mustafa, M.; Chen, Y.; Cao, Y.; Gao, J. Natural Thiopeptides as a Privileged Scaffold for Drug Discovery and Therapeutic Development. *Med. Chem. Res.* **2019**, *28*, 1063–1098.

(4) Vinogradov, A. A.; Suga, H. Introduction to Thiopeptides: Biological Activity, Biosynthesis, and Strategies for Functional Reprogramming. *Cell Chem. Biol.* **2020**, *27*, 1032–1051.

(5) Su, T. L. Micrococcin, an Antibacterial Substance Formed by a Strain of Micrococcus. *Br. J. Exp. Pathol.* **1948**, *29*, 473–481.

(6) Donovick, R.; Pagano, J. F.; Stout, H. A.; Weinstein, M. J. Thiostrepton, a New Antibiotic. I. In Vitro Studies. *Antibiot. Annu.* **1955**, *3*, 554–559.

(7) Dutcher, J. D.; Vandeputte, J. Thiostrepton, a New Antibiotic. II. Isolation and Chemical Characterization. *Antibiot. Annu.* **1955**, *3*, 560–561.

(8) Jambor, W. P.; Steinberg, B. A.; Suydam, L. O. Thiostrepton, a New Antibiotic. III. In Vivo Studies. *Antibiot. Annu.* **1955**, *3*, 562–565.

(9) Radhakrishnan, S. K.; Bhat, U. G.; Hughes, D. E.; Wang, I. C.; Costa, R. H.; Gartel, A. L. Identification of a Chemical Inhibitor of the Oncogenic Transcription Factor Forkhead Box M1. *Cancer Res.* **2006**, *66*, 9731–9735.

(10) Kwok, J. M. M.; Myatt, S. S.; Marson, C. M.; Coombes, R. C.; Constantinidou, D.; Lam, E. W. F. Thiostrepton Selectively Targets Breast Cancer Cells through Inhibition of Forkhead Box M1 Expression. *Mol. Cancer Ther.* **2008**, *7*, 2022–2032.

(11) Bhat, U. G.; Halasi, M.; Gartel, A. L. FoxM1 Is a General Target for Proteasome Inhibitors. *PLoS One* **2009**, *4*, e6593.

(12) Pandit, B.; Bhat, U.; Gartel, A. L. Proteasome Inhibitory Activity of Thiazole Antibiotics. *Cancer Biol. Ther.* **2011**, *11*, 43.

(13) Hegde, N. S.; Sanders, D. A.; Rodriguez, R.; Balasubramanian, S. The Transcription Factor FOXM1 Is a Cellular Target of the Natural Product Thiostrepton. *Nat. Chem.* **2011**, *3*, 725–731.

(14) Aoki, M.; Ohtsuka, T.; Itezono, Y.; Yokose, K.; Furihata, K.; Seto, H. Structure of Cyclothiazomycin, a Unique Polythiazole-Containing Peptide with Renin Inhibitory Activity. Part 1. Chemistry and Partial Structures of Cyclothiazomycin. *Tetrahedron Lett.* **1991**, *32*, 217–220.

(15) Aoki, M.; Ohtsuka, T.; Itezono, Y.; Yokose, K.; Furihata, K.; Seto, H. Structure of Cyclothiazomycin, a Unique Polythiazole-Containing Peptide with Renin Inhibitory Activity. Part 2. Total Structure. *Tetrahedron Lett.* **1991**, *32*, 221–224.

(16) Aoki, M.; Ohtsuka, T.; Yamada, M.; Ohba, Y.; Yoshizaki, H.; Yasuno, H.; Sano, T.; Watanabe, J.; Yokose, K.; Seto, H. Cyclothiazomycin, a Novel Polythiazole-Containing Peptide with Renin Inhibitory Activity. Taxonomy, Fermentation, Isolation and Physico-Chemical Characterization. *J. Antibiot. (Tokyo).* **1991**, *44*, 582–588.

(17) Mizuhara, N.; Kuroda, M.; Ogita, A.; Tanaka, T.; Usuki, Y.; Fujita, K. I. Antifungal Thiopeptide Cyclothiazomycin B1 Exhibits Growth Inhibition Accompanying Morphological Changes via Binding to Fungal Cell Wall Chitin. *Bioorg. Med. Chem.* **2011**, *19*, 5300–5310.

(18) Hashimoto, M.; Murakami, T.; Funahashi, K.; Tokunaga, T.; Nihei, K. ichi; Okuno, T.; Kimura, T.; Naoki, H.; Himeno, H. An RNA Polymerase Inhibitor, Cyclothiazomycin B1, and Its Isomer. *Bioorg. Med. Chem.* **2006**, *14*, 8259–8270.

(19) Benazet, F.; Cartier, J. R. Effect of Nosiheptide as a Feed Additive in Chicks on the Quantity, Duration, Prevalence of Excretion, and Resistance to Antibacterial Agents of Salmonella Typhimurium; on the Proportion of Escherichia Coli and Other Coliforms Resistant to Antibacterial Agents; and on Their Degree and Spectrum of Resistance. *Poult. Sci.* **1980**, *59*, 1405–1415.

(20) Wang, S.; Zheng, Q.; Wang, J.; Zhao, Z.; Li, Q.; Yu, Y.; Wang, R.; Liu, W. Target-Oriented Design and Biosynthesis of Thiostrepton-Derived Thiopeptide Antibiotics with Improved Pharmaceutical Properties. *Org. Chem. Front.* **2015**, *2*, 106–109.
(21) Aminake, M. N.; Schoof, S.; Sologub, L.; Leubner, M.; Kirschner, M.; Arndt, H. D.; Pradel, G. Thiostrepton and Derivatives Exhibit Antimalarial and Gametocytocidal Activity by Dually Targeting Parasite Proteasome and Apicoplast. *Antimicrob. Agents Chemother.* **2011**, *55*, 1338–1348.
(22) Murakami, T.; Holt, T. G.; Thompson, C. J. Thiostrepton-Induced Gene Expression in Streptomyces Lividans. *J. Bacteriol.* **1989**, *171*, 1459–1466.
(23) Schneider, H. J. Noncovalent Interactions: A Brief Account of a Long History. *J. Phys. Org. Chem.* **2022**, *35*, e4340.
(24) Kojasoy, V.; Tantillo, D. J. Impacts of Noncovalent Interactions Involving Sulfur Atoms on Protein Stability, Structure, Folding, and Bioactivity. *Org. Biomol. Chem.* **2023**, *21*, 11–23.
(25) Beno, B. R.; Yeung, K. S.; Bartberger, M. D.; Pennington, L. D.; Meanwell, N. A. A Survey of the Role of Noncovalent Sulfur Interactions in Drug Design. *J. Med. Chem.* **2015**, *58*, 4383–4438.
(26) Hudson, B. M.; Nguyen, E.; Tantillo, D. J. The Influence of Intramolecular Sulfur–Lone Pair Interactions on Small-Molecule Drug Design and Receptor Binding. *Org. Biomol. Chem.* **2016**, *14*, 3975–3980.
(27) Kilgore, H. R.; Raines, R. T. n→π∗ Interactions Modulate the Properties of Cysteine Residues and Disulfide Bonds in Proteins. *J. Am. Chem. Soc.* **2018**, *140*, 17606–17611.
(28) Newberry, R. W.; Raines, R. T. Secondary Forces in Protein Folding. *ACS Chem. Biol.* **2019**, *14*, 1677–1686.
(29) Xiao, Y. N.; Zhang, C. X. Weak Nonbonded S···X (X = O, N, and S) Interactions in Proteins. Statistical and Theoretical Studies. *Bull. Chem. Soc. Jpn.* **2002**, *75*, 1611–1625.
(30) Newberry, R. W.; Bartlett, G. J.; VanVeller, B.; Woolfson, D. N.; Raines, R. T. Signatures of n→π* Interactions in Proteins. *Protein Sci.* **2014**, *23*, 284–288.
(31) Motherwell, W. B.; Moreno, R. B.; Pavlakos, I.; Arendorf, J. R. T.; Arif, T.; Tizzard, G. J.; Coles, S. J.; Aliev, A. E. Noncovalent Interactions of π Systems with Sulfur: The Atomic Chameleon of Molecular Recognition. *Angew. Chem. Int. Ed.* **2018**, *130*, 1207–1212.
(32) Van Bergen, L. A. H.; Alonso, M.; Palló, A.; Nilsson, L.; De Proft, F.; Messens, J. Revisiting Sulfur H-Bonds in Proteins: The Example of Peroxiredoxin AhpE. *Sci. Rep.* **2016**, *6*, 1–11.
(33) Ringer, A. L.; Senenko, A.; Sherrill, C. D. Models of S/π Interactions in Protein Structures: Comparison of the H2S–Benzene Complex with PDB Data. *Protein Sci.* **2007**, *16*, 2216.
(34) Choudhary, A.; Gandla, D.; Krow, G. R.; Raines, R. T. Nature of Amide Carbonyl--Carbonyl Interactions in Proteins. *J. Am. Chem. Soc.* **2009**, *131*, 7244–7246.
(35) Newberry, R. W.; Vanveller, B.; Guzei, I. A.; Raines, R. T. n→π* Interactions of Amides and Thioamides: Implications for Protein Stability. *J. Am. Chem. Soc.* **2013**, *135*, 7843.
(36) Newberry, R. W.; VanVeller, B.; Raines, R. T. Thioamides in the Collagen Triple Helix. *Chem. Commun.* **2015**, *51*, 9624–9627.
(37) Honda, T.; Tajima, H.; Kaneko, Y.; Ban, M.; Inaba, T.; Takeno, Y.; Okamoto, K.; Aono, H. Conformation-Activity Relationship on Novel 4-Pyridylmethylthio Derivatives with Antiangiogenic Activity. *Bioorg. Med. Chem. Lett.* **2008**, *18*, 2939–2943.
(38) Tajima, H.; Honda, T.; Kawashima, K.; Sasabuchi, Y.; Yamamoto, M.; Ban, M.; Okamoto, K.; Inoue, K.; Inaba, T.; Takeno, Y.; Aono, H. Pyridylmethylthio Derivatives as VEGF Inhibitors. Part 1. *Bioorg. Med. Chem. Lett.* **2010**, *20*, 7234–7238.
(39) Tajima, H.; Honda, T.; Kawashima, K.; Sasabuchi, Y.; Yamamoto, M.; Ban, M.; Okamoto, K.; Inoue, K.; Inaba, T.; Takeno, Y.; Tsuboi, T.; Tonouchi, A.; Aono, H. Pyridylmethylthio Derivatives as VEGF Inhibitors: Part 2. *Bioorg. Med. Chem. Lett.* **2011**, *21*, 1232–1235.
(40) Wagner, J. P.; Schreiner, P. R. London Dispersion in Molecular Chemistry - Reconsidering Steric Effects. *Angew. Chem. Int. Ed.* **2015**, *54*, 12274–12296.
(41) Connolly, T. P.; Regueiro-Ren, A.; Leet, J. E.; Springer, D. M.; Goodrich, J.; Huang, X.; Pucci, M.

J.; Clark, J. M.; Bronson, J. J.; Ueda, Y. Chemical Conversion of Nocathiacin I to Nocathiacin II and a Lactone Analogue of Glycothiohexide Alpha. *J. Nat. Prod.* **2005**, *68*, 550–553.
(42) Steinberg, D. A.; Bernan, V. S.; Montenegro, D. A.; Abbanat, D. R.; Pearce, C. J.; Korshalla, J. D.; Jacobus, N. V.; Petersen, P. J.; Mroczenski-Wildey, M. J.; Maiese, W. M.; Greenstein, M. Glycothiohexides, Novel Antibiotics Produced by "Sebekia" Sp. LL-14E605. I. Taxonomy, Fermentation and Biological Evaluation. *J. Antibiot. (Tokyo).* **1994**, *47*, 887–893.
(43) Northcote, P. T.; Williams, D.; Manning, J. K.; Borders, D. B.; Maiese, W. M.; Lee, M. D. Glycothiohexide α, A Novel Antibiotic Produced by "Sebekia" Sp. LL-14E605. *J. Antibiot. (Tokyo).* **1994**, *47*, 894–900.
(44) Northcote, P. T.; Siegel, M.; Borders, D. B.; Lee, M. D. Glycothiohexide Alpha, a Novel Antibiotic Produced by "Sebekia" Sp., LL-14E605. III. Structural Elucidation. *J. Antibiot. (Tokyo).* **1994**, *47*, 901–908.
(45) Constantine, K. L.; Mueller, L.; Huang, S.; Abid, S.; Lam, K. S.; Li, W.; Leet, J. E. Conformation and Absolute Configuration of Nocathiacin I Determined by NMR Spectroscopy and Chiral Capillary Electrophoresis. *J. Am. Chem. Soc.* **2002**, *124*, 7284–7285.
(46) Li, W.; Leet, J. E.; Ax, H. A.; Gustavson, D. R.; Brown, D. M.; Turner, L.; Brown, K.; Clark, J.; Yang, H.; Fung-Tomc, J.; Lam, K. S. Nocathiacins, New Thiazolyl Peptide Antibiotics from Nocardia Sp. I. Taxonomy, Fermentation and Biological Activities. *J. Antibiot. (Tokyo).* **2003**, *56*, 226–231.
(47) Leet, J. E.; Li, W.; Ax, H. A.; Matson, J. A.; Huang, S.; Huang, R.; Cantone, J. L.; Drexler, D.; Dalterio, R. A.; Lam, K. S. Nocathiacins, New Thiazolyl Peptide Antibiotics from Nocardia Sp. II. Isolation, Characterization, and Structure Determination. *J. Antibiot. (Tokyo).* **2003**, *56*, 232–242.
(48) Pucci, M. J.; Bronson, J. J.; Barrett, J. F.; Denbleyker, K. L.; Discotto, L. F.; Fung-Tomc, J. C.; Ueda, Y. Antimicrobial Evaluation of Nocathiacins, a Thiazole Peptide Class of Antibiotics. *Antimicrob. Agents Chemother.* **2004**, *48*, 3697–3701.
(49) Stone, A. J. Natural Bond Orbitals and the Nature of the Hydrogen Bond. *J. Phys. Chem. A* **2017**, *121*, 1531–1534.
(50) Weinhold, F.; Glendening, E. D. Comment on "Natural Bond Orbitals and the Nature of the Hydrogen Bond." *J. Phys. Chem. A* **2018**, *122*, 724–732.
(51) Stone, A. J.; Szalewicz, K. Reply to "Comment on 'Natural Bond Orbitals and the Nature of the Hydrogen Bond.'" *J. Phys. Chem. A* **2018**, *122*, 733–736.
(52) Johnson, E. R.; Keinan, S.; Mori-Sánchez, P.; Contreras-García, J.; Cohen, A. J.; Yang, W. Revealing Noncovalent Interactions. *J. Am. Chem. Soc.* **2010**, *132*, 6498–6506.
(53) Weinhold, F.; Landis, C. R.; Glendening, E. D. What Is NBO Analysis and How Is It Useful? *Int. Rev. Phys. Chem.* **2016**, *35*, 399–440.
(54) Jeziorski, B.; Moszynski, R.; Szalewicz, K. Perturbation Theory Approach to Intermolecular Potential Energy Surfaces of van Der Waals Complexes. *Chem. Rev.* **1994**, *94*, 1887–1930.
(55) Patkowski, K. Recent Developments in Symmetry-Adapted Perturbation Theory. *Wiley Interdiscip. Rev. Comput. Mol. Sci.* **2020**, *10*, e1452.
(56) Frisch, M. J.; Trucks, G. W.; Schlegel, H. B.; Scuseria, G. E.; Robb, M. A.; Cheeseman, J. R.; Scalmani, G.; Barone, V.; Petersson, G. A.; Nakatsuji, H., et al. *Gaussian 16,* Revision A.03.; Gaussian, Inc.: Wallingford, CT, 2016.
(57) Zhao, Y.; Truhlar, D. G. Density Functionals with Broad Applicability in Chemistry. *Acc. Chem. Res.* **2008**, *41*, 157–167.
(58) Zhao, Y.; Truhlar, D. G.; Zhao, Y.; Truhlar, · D G. The M06 Suite of Density Functionals for Main Group Thermochemistry, Thermochemical Kinetics, Noncovalent Interactions, Excited States, and Transition Elements: Two New Functionals and Systematic Testing of Four M06-Class Functionals and 12 Other Function. *Theor. Chem. Accounts 2007 1201* **2007**, *120*, 215–241.
(59) Frisch, M. J.; Pople, J. A.; Binkley, J. S. Self-consistent Molecular Orbital Methods 25. Supplementary Functions for Gaussian Basis Sets. *J. Chem. Phys.* **1998**, *80*, 3265.
(60) Lodewyk, M. W.; Siebert, M. R.; Tantillo, D. J. Computational Prediction of ^{1}H and ^{13}C Chemical

Shifts: A Useful Tool for Natural Product, Mechanistic, and Synthetic Organic Chemistry. *Chem. Rev.* **2012**, *112*, 1839–1862.
(61) Marenich, A. V.; Cramer, C. J.; Truhlar, D. G. Universal Solvation Model Based on Solute Electron Density and on a Continuum Model of the Solvent Defined by the Bulk Dielectric Constant and Atomic Surface Tensions. *J. Phys. Chem. B* **2009**, *113*, 6378–6396.
(62) Adamo, C.; Barone, V. Exchange Functionals with Improved Long-Range Behavior and Adiabatic Connection Methods without Adjustable Parameters: The MPW and MPW1PW Models. *J. Chem. Phys.* **1998**, *108*, 664.
(63) Cheeseman, J. R.; Trucks, G. W.; Keith, T. A.; Frisch, M. J. Shielding Tensors. *J. Chem. Phys.* **1996**, *104*, 5497–5509.
(64) Wolinski, K.; Hinton, J. F.; Pulay, P. Efficient Implementation of the Gauge-Independent Atomic Orbital Method for NMR Chemical Shift Calculations. *J. Am. Chem. Soc.* **1990**, *112*, 8251–8260.
(65) Bagno, A.; Saielli, G. Addressing the Stereochemistry of Complex Organic Molecules by Density Functional Theory-NMR. *Wiley Interdiscip. Rev. Comput. Mol. Sci.* **2015**, *5*, 228–240.
(66) de Albuquerque, A. C. F.; Ribeiro, D. J.; de Amorim, M. B. Structural Determination of Complex Natural Products by Quantum Mechanical Calculations of ^{13}C NMR Chemical Shifts: Development of a Parameterized Protocol for Terpenes. *J. Mol. Model.* **2016**, *22*, 1–7.
(67) Glendening, E. D.; Reed, A. E.; Carpenter, J. E.; Weinhold, F. NBO Version 3.1.; Gaussian Inc.: Pittsburgh 2003.
(68) Lu, T.; Chen, F. Multiwfn: A Multifunctional Wavefunction Analyzer. *J. Comput. Chem.* **2012**, *33*, 580–592.
(69) Hohenstein, E. G.; Sherrill, C. D. Density Fitting and Cholesky Decomposition Approximations in Symmetry-Adapted Perturbation Theory: Implementation and Application to Probe the Nature of π - π. *J. Chem. Phys.* **2010**, *132*, 184111.
(70) Hohenstein, E. G.; Parrish, R. M.; Sherrill, C. D.; Turney, J. M.; Schaefer, H. F. Large-Scale Symmetry-Adapted Perturbation Theory Computations via Density Fitting and Laplace Transformation Techniques: Investigating the Fundamental Forces of DNA-Intercalator Interactions. *J. Chem. Phys.* **2011**, *135*, 174107.
(71) Parrish, R. M.; Parker, T. M.; David Sherrill, C. Chemical Assignment of Symmetry-Adapted Perturbation Theory Interaction Energy Components: The Functional-Group SAPT Partition. *J. Chem. Theory Comput.* **2014**, *10*, 4417–4431.
(72) Parrish, R. M.; Sherrill, C. D. Quantum-Mechanical Evaluation of π-π Versus Substituent-π Interactions in π Stacking: Direct Evidence for the Wheeler-Houk Picture. *J. Am. Chem. Soc.* **2014**, *136*, 17386–17389.
(73) Parrish, R. M.; Gonthier, J. F.; Corminbœuf, C.; Sherrill, C. D. Communication: Practical Intramolecular Symmetry Adapted Perturbation Theory via Hartree-Fock Embedding. *J. Chem. Phys.* **2015**, *143*, 051103.
(74) Hohenstein, E. G.; Sherrill, C. D. Density Fitting of Intramonomer Correlation Effects in Symmetry-Adapted Perturbation Theory. *J. Chem. Phys.* **2010**, *133*, 014101.
(75) Smith, D. G. A.; Burns, L. A.; Simmonett, A. C.; Parrish, R. M.; Schieber, M. C.; Galvelis, R.; Kraus, P.; Kruse, H.; Di Remigio, R.; Alenaizan, A., et al. PSI4 1.4: Open-Source Software for High-Throughput Quantum Chemistry. *J. Chem. Phys.* **2020**, *152*, 184108.
(76) Murray, J. S.; Politzer, P. The Electrostatic Potential: An Overview. *Wiley Interdiscip. Rev. Comput. Mol. Sci.* **2011**, *1*, 153–163.
(77) Cons, B. D.; Twigg, D. G.; Kumar, R.; Chessari, G. Electrostatic Complementarity in Structure-Based Drug Design. *J. Med. Chem.* **2022**, *65*, 7476–7488.
(78) ChemSpider. http://www.chemspider.com/Chemical-Structure.10190178.html/ (accessed May 2021).
(79) The major conformers we obtained for nocathiacin I differ from those reported by Leet and co-workers in ref. 45. Given the limitations of our modeling; we cannot say with certainty which are lower in energy. We can say, however, that our attempts to build a conformer similar to those shown

in ref. 45 led to NMR predictions with larger deviations than observed for the ones used for our analysis. In any case, it is certainly possible that both types of conformers are present in solution.
(80) Bühl, M.; van Mourik, T. NMR Spectroscopy: Quantum-Chemical Calculations. *Wiley Interdiscip. Rev. Comput. Mol. Sci.* **2011**, *1*, 634–647.
(81) Toukach, F. V.; Ananikov, V. P. Recent Advances in Computational Predictions of NMR Parameters for the Structure Elucidation of Carbohydrates: Methods and Limitations. *Chem. Soc. Rev.* **2013**, *42*, 8376–8415.
(82) Schattenberg, C. J.; Kaupp, M. Extended Benchmark Set of Main-Group Nuclear Shielding Constants and NMR Chemical Shifts and Its Use to Evaluate Modern DFT Methods. *J. Chem. Theory Comput.* **2021**, *17*, 7602–7621.
(83) Bagno, A.; Saielli, G. Computational NMR Spectroscopy: Reversing the Information Flow. *Theor. Chem. Acc. 117*, 603–619.
(84) Based on our NMR predictions, the MADs from the experimentally obtained $^{13}C/^{1}H$ chemical shifts [44,47] (ppm) are computed to be 2.0/0.7 and 1.9/0.7 for the protonated (at the amine) forms of glycothiohexide α and nocathiacin I, respectively (excluding hydrogens attached to heteroatoms). Since the geometries of neutral and protonated forms of the thiopeptides are almost identical, all the analyses reported here are conducted on the neutral forms.
(85) NP-MRD. https://np-mrd.org/natural_products/NP0004603/ (accessed June 6, 2022).
(86) Zaretsky, S.; Hickey, J. L.; St. Denis, M. A.; Scully, C. C. G.; Roughton, A. L.; Tantillo, D. J.; Lodewyk, M. W.; Yudin, A. K. Predicting Cyclic Peptide Chemical Shifts Using Quantum Mechanical Calculations. *Tetrahedron* **2014**, *70*, 7655–7663.
(87) Nguyen, Q. N. N.; Schwochert, J.; Tantillo, D. J.; Lokey, R. S. Using 1H and 13C NMR Chemical Shifts to Determine Cyclic Peptide Conformations: A Combined Molecular Dynamics and Quantum Mechanics Approach. *Phys. Chem. Chem. Phys.* **2018**, *20*, 14003–14012.
(88) Laplaza, R.; Peccati, F.; A. Boto, R.; Quan, C.; Carbone, A.; Piquemal, J. P.; Maday, Y.; Contreras-García, J. NCIPLOT and the Analysis of Noncovalent Interactions Using the Reduced Density Gradient. *Wiley Interdiscip. Rev. Comput. Mol. Sci.* **2021**, *11*, e1497.
(89) Contreras-García, J.; Boto, R. A.; Izquierdo-Ruiz, F.; Reva, I.; Woller, T.; Alonso, M. A Benchmark for the Non-Covalent Interaction (NCI) Index Or… Is It Really All in the Geometry? *Theor. Chem. Acc.* **2016**, *135*, 1–14.
(90) Biswal, H. S. Hydrogen Bonds Involving Sulfur: New Insights from Ab Initio Calculations and Gas Phase Laser Spectroscopy. *Challenges Adv. Comput. Chem. Phys.* **2015**, *19*, 15–45.
(91) Steiner, T. S - H...S Hydrogen-Bond Chain in Thiosalicylic Acid. *Acta Crystallogr. Sect. C Cryst. Struct. Commun.* **2000**, *56*, 876–877.
(92) Meyer, E.; Joussef, A. C.; Gallardo, H.; Bortoluzzi, A. J.; Longo, R. L. 1,5-Type Nonbonded O···S and S···S Interactions in (Acylimino) and (Thioacylimino)Benzothiazoline Systems. Crystal Structures and Theoretical Calculations. *Tetrahedron* **2003**, *59*, 10187–10193.
(93) Hayashi, K.; Ogawa, S.; Sano, S.; Shiro, M.; Yamaguchi, K.; Sei, Y.; Nagao, Y. Intramolecular Nonbonded S···N Interaction in Rabeprazole. *Chem. Pharm. Bull.* **2008**, *56*, 802–806.
(94) Nagao, Y.; Hirata, T.; Goto, S.; Sano, S.; Kakehi, A.; Iizuka, K.; Shiro, M. Intramolecular Nonbonded S···O Interaction Recognized in (Acylimino)Thiadiazoline Derivatives as Angiotensin II Receptor Antagonists and Related Compounds. *J. Am. Chem. Soc.* **1998**, *120*, 3104–3110.
(95) Biirgi, H. B.; Dunitz, J. D.; Shefter, E. Geometrical Reaction Coordinates. II. Nucleophilic Addition to a Carbonyl Group. *J. Am. Chem. Soc.* **1973**, *95*, 5065–5067.
(96) Chakrabarti, P.; Pal, D. An Electrophile-Nucleophile Interaction in Metalloprotein Structures. *Protein Sci.* **1997**, *6*, 851–859.
(97) Bartlett, G. J.; Choudhary, A.; Raines, R. T.; Woolfson, D. N. N-->pi* Interactions in Proteins. *Nat. Chem. Biol.* **2010**, *6*, 615–620.
(98) Bartlett, G. J.; Newberry, R. W.; Vanveller, B.; Raines, R. T.; Woolfson, D. N. Interplay of Hydrogen Bonds and n →π* Interactions in Proteins. *J. Am. Chem. Soc.* **2013**, *135*, 18682–18688.
(99) Newberry, R. W.; Raines, R. T. The n→π∗ Interaction. *Acc. Chem. Res.* **2017**, *50*, 1838–1846.

(100) Naidu, B. N.; Sorenson, M. E.; Matiskella, J. D.; Li, W.; Sausker, J. B.; Zhang, Y.; Connolly, T. P.; Lam, K. S.; Bronson, J. J.; Pucci, M. J.; Yang, H.; Ueda, Y. Synthesis and Antibacterial Activity of Nocathiacin I Analogues. *Bioorg. Med. Chem. Lett.* **2006**, *16*, 3545–3549.
(101) Regueiro-Ren, A.; Naidu, B. N.; Zheng, X.; Hudyma, T. W.; Connolly, T. P.; Matiskella, J. D.; Zhang, Y.; Kim, O. K.; Sorenson, M. E.; Pucci, M.; Clark, J.; Bronson, J. J.; Ueda, Y. Novel Semi-Synthetic Nocathiacin Antibiotics: Synthesis and Antibacterial Activity of Bis- and Mono-O-Alkylated Derivatives. *Bioorganic Med. Chem. Lett.* **2004**, *14*, 171–175.
(102) Naidu, B. N.; Sorenson, M. E.; Hudyma, T.; Zheng, X.; Zhang, Y.; Bronson, J. J.; Pucci, M. J.; Clark, J. M.; Ueda, Y. Synthesis and Antibacterial Activity of O-Substituted Nocathiacin I Derivatives. *Bioorganic Med. Chem. Lett.* **2004**, *14*, 3743–3746.
(103) Naidu, B. N.; Sorenson, M. E.; Zhang, Y.; Kim, O. K.; Matiskella, J. D.; Wichtowski, J. A.; Connolly, T. P.; Li, W.; Lam, K. S.; Bronson, J. J.; Pucci, M. J.; Clark, J. M.; Ueda, Y. Nocathiacin I Analogues: Synthesis, in Vitro and in Vivo Biological Activity of Novel Semi-Synthetic Thiazolyl Peptide Antibiotics. *Bioorganic Med. Chem. Lett.* **2004**, *14*, 5573–5577.
(104) Naidu, B. N.; Sorenson, M. E.; Bronson, J. J.; Pucci, M. J.; Clark, J. M.; Ueda, Y. Synthesis, in Vitro, and in Vivo Antibacterial Activity of Nocathiacin I Thiol-Michael Adducts. *Bioorganic Med. Chem. Lett.* **2005**, *15*, 2069–2072.
(105) Myers, C. L.; Hang, P. C.; Ng, G.; Yuen, J.; Honek, J. F. Semi-Synthetic Analogues of Thiostrepton Delimit the Critical Nature of Tail Region Modifications in the Control of Protein Biosynthesis and Antibacterial Activity. *Bioorg. Med. Chem.* **2010**, *18*, 4231–4237.
(106) Meinander, K.; Weisell, J.; Pakkala, M.; Tadd, A. C.; Hekim, C.; Kallionpää, R.; Widell, K.; Stenman, U. H.; Koistinen, H.; Närvänen, A.; Vepsäläinen, J.; Luthman, K.; Wallén, E. A. A. Pseudopeptides with a Centrally Positioned Alkene -Based Disulphide Bridge Mimetic Stimulate Kallikrein-Related Peptidase 3 Activity. *Medchemcomm* **2013**, *4*, 549–553.
(107) Meinander, K.; Pakkala, M.; Weisell, J.; Stenman, U. H.; Koistinen, H.; Närvänen, A.; Wallén, E. A. A. Replacement of the Disulfide Bridge in a KLK3-Stimulating Peptide Using Orthogonally Protected Building Blocks. *ACS Med. Chem. Lett.* **2013**, *5*, 162–165.
(108) Stymiest, J. L.; Mitchell, B. F.; Wong, S.; Vederas, J. C. Synthesis of Oxytocin Analogues with Replacement of Sulfur by Carbon Gives Potent Antagonists with Increased Stability. *J. Org. Chem.* **2005**, *70*, 7799–7809.
(109) Stymiest, J. L.; Mitchell, B. F.; Wong, S.; Vederas, J. C. Synthesis of Biologically Active Dicarba Analogues of the Peptide Hormone Oxytocin Using Ring-Closing Metathesis. *Org. Lett.* **2003**, *5*, 47–49.
(110) Hansch, C.; Steward, A. R.; Anderson, S. M.; Bentley, D. The Parabolic Dependence of Drug Action upon Lipophilic Character as Revealed by a Study of Hypnotics. *J. Med. Chem.* **1968**, *11*, 1–11.

Chapter 3. Elucidation of Organic Reaction Mechanisms Involving Sulfur Atoms

3.1. The Reaction of Hydropersulfides (RSSH) with S-Nitrosothiols (RS-NO) and the Biological/Physiological Implications

This chapter is adapted with slight modifications with permission from Zarenkiewicz, J.[#]; Perez-Ternero, C.[#]; Kojasoy, V.[#]; McGinity, C.; Khodade, V. S.; Lin, J.; Tantillo, D. J.; Toscano, J. P.; Hobbs, A. J.; Fukuto, J. M. The Reaction of Hydropersulfides (RSSH) with S-Nitrosothiols (RS-NO) and the Biological/Physiological Implications. *Free Radic. Biol. Med.* **2022**, *188*, 459-467 ([#] equal contribution). Jessica Zarenkiewicz (of Prof. John P. Toscano's group) ran the chemical reactions and performed the chemical analysis of reaction products. Cristina Perez-Ternero (The William Harvey Research Institute) performed the biological tissue bath studies. Christopher McGinity (The William Harvey Research Institute) performed initial biological and chemical studies. Vinayak S. Khodade (of Prof. John P. Toscano's group) synthesized the RSSH donors.

3.1.1 Abstract

S-Nitrosothiol (RS-NO) generation/levels have been implicated as being important to numerous physiological and pathophysiological processes. As such, the mechanism(s) of their generation and degradation are important factors in determining their biological activity. Along with the effects on the activity of thiol proteins, RS-NOs have also been reported to be reservoirs or storage forms of nitric oxide (NO). That is, it is hypothesized that NO can be released from RS-NO at opportune times to, for example, regulate vascular tone. However, to date there are few established mechanisms that can account for facile NO release from RS-NO. Recent discovery of the biological formation and prevalence of hydropersulfides (RSSH) and their subsequent reaction with RS-NO species provides a possible route for NO release from RS-NO. Herein, it is found that RSSH is capable of reacting with RS-NO to liberate NO and that the analogous reaction using RSH is not nearly as proficient in generating NO. Moreover, computational results support the prevalence of this reaction over other possible competing processes. Finally, results of

biological studies of NO-mediated vasorelaxation are consistent with the idea that RS-NO species can be degraded by RSSH to release NO.

3.1.2 Introduction

S-Nitrosothiols (RS-NO) are implicated as playing a role in numerous physiological functions. For example, RS-NO species have been proposed to be storage forms of nitric oxide (NO) capable of being released at opportune times for the control of vascular tone (e.g., ref. 1-2 or intracellular intermediates in the vasorelaxant activity of NO[3]). Moreover, aberrant RS-NO generation (e.g., in crucial cysteine-containing proteins) has been proposed to be involved in the etiology of numerous pathophysiologies such as in the development of neurodegenerative disease[4,5] or cancer[6,7]. Although there is little doubt that the RS-NO function is prevalent in both small molecules (e.g., S-nitrosoglutathione, GS-NO) and in cysteine-containing proteins, the mechanisms by which they are generated and degraded physiologically remain elusive. Thus, the processes that determine the steady-state levels of RS-NO species are currently unestablished. In the case of possible NO liberation from RS-NO functionalities, many of the proposed mechanisms of RS-NO degradation either do not result in the release of NO or are considered to be physiologically irrelevant.[8] Regardless, pathways that establish steady-state RS-NO levels and that can lead to the liberation of NO from RS-NO may have important physiological consequences.

Recent work indicates that hydropersulfides (RSSH) along with other polysulfur species are prevalent and potentially important biological effectors (for reviews, see ref. 9-10). One of the prevailing ideas regarding the presence and function of RSSH species is that they can serve a cellular protective role as scavengers of potentially toxic electrophiles and/or deleterious oxidants (e.g., ref. 11). A rationale for this speculation is that RSSH species are superior reductants and nucleophiles compared to the corresponding thiols and, therefore, capable of facile scavenging of toxic oxidants/electrophiles and/or reversing their effects. An important aspect of this idea is that as an oxidized species, RSSH is more likely generated under cellular oxidizing conditions (i.e., under oxidative stress). This means that a superior reductant/nucleophile, RSSH, can be generated primarily under cellular oxidizing conditions, a situation

that may prevent or mitigate oxidation/electrophile-mediated cellular damage. A recent report from our lab also indicates that under purely chemical conditions RSSH reacts readily with R'S-NO species leading to NO liberation and the generation of the corresponding dialkyltetrasulfide (RSSSSR).[12] The proposed mechanism for this observation involves an initial nucleophilic attack of RSSH (likely as the anionic RSS^- species) on the electrophilic R'S-NO nitrogen giving, initially, an S-nitrosopersulfide (RSS-NO) intermediate (reaction 1). This reaction is then followed by spontaneous homolysis of the weak S–N bond to give NO and the perthiyl radical species (reaction 2) which in turn will dimerize to the tetrasulfide (reaction 3).[12-14]

$$\mathrm{RSSH} + \mathrm{R'S{-}NO} \rightarrow \mathrm{RSS\text{-}NO} + \mathrm{R'SH} \qquad \text{(reaction 1)}$$

$$\mathrm{RSS\text{-}NO} \rightarrow \mathrm{RSS}\cdot + \mathrm{NO} \qquad \text{(reaction 2)}$$

$$\mathrm{RSS}\cdot \rightarrow \tfrac{1}{2}\ \mathrm{RSSSSR} \qquad \text{(reaction 3)}$$

Importantly, the homolysis of the intermediate RSS-NO species (reaction 2) is due to the relative stability of the two radical species, NO and RSS·.[12] Predictably, S–N homolysis not nearly as facile with R'S-NO species due to the relative instability of R'S· (e.g., the R'S· is higher in energy compared to RSS· and readily reacts with O_2, NO and is a potent oxidant (vide infra), while RSS· is lower in energy and does not readily react with O_2 or NO and is a weak oxidant).

The chemistry described immediately above is of potential physiological relevance since it represents a mechanism of R'S-NO degradation and therefore could possibly be involved in determining R'S-NO steady-state levels. Moreover, the above R'S-NO degradation chemistry results in the liberation of NO, a process potentially important if indeed R'S-NO species are used as reservoirs and/or storage forms of NO.[8] Considering the possible importance of R'S-NO species to normal physiology as well as in the etiology of disease and as sources of NO, the chemistry and biological effects of the reaction of RSSH with R'S-NO are further investigated herein.

3.1.3 Methods

General Methods: All chemicals were purchased from commercial sources and used as received unless stated otherwise. A Fisher Scientific Accumet AB15 pH-meter was used for pH measurements. GC analysis was performed on an Agilent 8860 equipped with an electron capture detector (ECD) and Restek column (ShinCarbon ST 80/100, 2 m, 1/8" OD).

Synthesis and Characterization: RSSH donor 2-(((3-acetamido-4-methoxy-2-methyl-4 oxobutan-2-yl)disulfannecarbonyl)(methyl) amino)-ethan-1-aminium (**1**), GSNO, and *N*-acetylpenicillamine methyl ester were synthesized according to literature procedures and analytical characterization data were consistent with the reported values.[15]

Analysis of RSSH/RSH reaction with RS-NO by membrane inlet mass spectrometry (MIMS): MIMS was carried out using a Hiden HPR-40 system containing a 20 mL sample cell and a membrane selective for detecting gases (e.g., NO, N_2O, and H_2S) dissolved in aqueous solution.[16,17] The sample cell was filled with 20 mL of PBS (pH 7.4, 100 mM) containing diethylenetriaminepentaacetic acid (DTPA, 100 μM) and purged with argon for at least 30 min prior to analysis. The sample cell was also wrapped in aluminum foil to prevent photolysis of GSNO. Stock solutions of GSNO were prepared in PBS and RSSH/RSH was prepared in either DMSO or buffer. These stock solutions were purged with nitrogen for 10 min and used shortly after preparation. Aliquots of these solutions were injected into the sample cell using a gastight syringe and masses of interest were monitored with continuous sampling in positive ion mode.

GC Headspace analysis of RSSH/RSH reaction with RS-NO: Thiol stock solutions were prepared in DMSO. In a 15 mL vial sealed with rubber septum, PBS (pH 7.4, 100 mM) containing DTPA (100 μM) was purged with argon for 20 min. These vials were placed in a heated cell block, which was held at 37 °C. The RSSH or thiol and GSNO solutions were added to each vial to obtain 5 mL total volume, and resulting solutions were incubated for 3 h at 37 °C. Headspace gas samples (60 μL) were injected into Agilent 8860

GC with a Restek column (ShinCarbon ST 80/100, 2 m, 1/8" OD) to analyze N_2O. These experiments were carried out in triplicate for each concentration of interest and three injections were performed for each vial.

Organ bath pharmacology: Mice (C57/BL6; wild type, WT) or soluble guanylyl cyclase knockout (sGC KO; kind gift of Michael Tones, Pfizer; male & female; 20–30 g) were euthanized by cervical dislocation. The thoracic aorta was carefully removed, cleaned of connective tissue and cut into three or four ring segments of approximately 4 mm in length. Aortic rings were mounted in 7 mL organ baths (Danish Myotechnology, Aarhus, Denmark) containing Krebs-bicarbonate buffer (composition (mM): Na^+ 143; K^+ 5.9; Ca^{2+} 2.5; Mg^{2+} 1.2; Cl^- 128; HCO_3^- 25; HPO_4^{2-} 1.2; SO_4^{2-} 1.2; D-Glucose 11) and gassed with carbogen (95% O_2 / 5% CO_2; British Oxygen Company; BOC; Guildford, UK). Tension was initially set at 0.3 g and reset at intervals following an equilibration period of approximately 1 h during which time fresh Krebs-bicarbonate buffer was replaced every 15 min. After equilibration, the rings were primed with three separate additions of KCl (48 mM; Sigma Aldrich, Poole, UK), at each addition maximum tension was observed (approx. 3 min) before being washed out by the addition of fresh Krebs-bicarbonate buffer at 10 min intervals for a total of 30 min. Cumulative concentrations of the α-adrenoceptor agonist phenylephrine (PE; 1 nM-3 μM) were then added until a maximum contraction was observed. Another washout period was performed before vessels were contracted to an EC80 concentration of PE. Once this response had stabilized, a single addition of the endothelium-dependent dilator acetylcholine (ACh; 1 μM) was added to the bath to assess the integrity of the endothelium. If the contractions to PE were not maintained, or ACh produced relaxations of less than 50% of the PE-tone, tissues were discarded (apart from denuded studies; see below).

After another wash period, the vessels were again contracted with PE (EC_{80}) and cumulative concentration response curves to S-nitroso-*N*-acetyl-penicillamine (SNAP; 1 nM-10 μM), CysSSSCys (100 nM-300 μM), or RSSH donor **1** (100 nM-300 μM) were constructed. Tone was raised to the same PE EC_{80} as that determined in the absence of L-NAME/ODQ/endothelial denudation or in WT tissues (for sGC KO). Responses to SNAP were also studied in the presence of CysSSSCys and **1** (both at 10 μM; 15 min pre-

incubation). In turn, concentration-dependent responses to CysSSSCys and **1** (100 nM-300 μM) were explored in the presence of SNAP (100 μM; 30 min pre-incubation and washout). In further studies, to establish the NO-dependency of vasorelaxant responses to CysSSSCys, concentration-dependent relaxations to CysSSSCys were evaluated in the presence of the NO synthase inhibitor N^G-nitro-L-arginine methyl-ester (L-NAME; 300 μM; 15 min pre-incubation), the soluble guanylyl cyclase (sGC) inhibitor 1H-[1,2,4]oxadiazolo [4,3,-a]quinoxalin-1-one (ODQ) (5 μM), following denudation of the endothelium (rubbing gently the internal surface of each aortic ring with forceps and determined by a lack [<10%] relaxation to ACh [1 μM]), or in tissues from sGC knockout mice.

Acute blood pressure measurement in anaesthetized mice: Mice (C57/BL6; WT; male and female; 20–30 g) were anaesthetized with 1.5% isoflurane (Abbott Laboratories Ltd, Queenborough, UK) in O_2 and placed supine on a thermostatically controlled heating blanket (37.0 °C ± 0.5 ◦C). To measure blood pressure, the left common carotid artery was isolated and a fluid-filled (heparin; 100U/ml diluted in 0.9% saline), 0.28 mm internal diameter cannula (Critchley Electrical Products Pty Ltd, Castle Hill, Australia) introduced into the artery. Blood pressure was measured using an in-line P23 XL transducer (Viggo-Spectramed, USA, California) and PowerLab system, calibrated beforehand, and recorded using LabChart (ADInstruments, Castle Hill, Australia). The jugular vein was cannulated for drug administration. The arterial cannula was flushed once with heparinized saline (heparin; 100 U/ml diluted in 0.9% saline). After a minimum 10 min equilibration or until continuous stable pressure was observed, mice were given an intravenous bolus injection of CysSSSCys (1–10 mg/kg), **1** (1–10 mg/kg) or sodium nitroprusside (SNP; 1–10 μg/kg).

Computational Studies: Density functional theory (DFT) calculations were carried out using Gaussian 16[18] at the SMD(H2O)-M06-2X/def2-SVP//M06-2X/def2-SVP level of theory (see SI for details).[19-23] Intrinsic reaction coordinate (IRC) calculations were performed to confirm the transition state structures (TSSs) connect the expected minima.[24-26] The robustness of our chosen level of theory was investigated through a benchmark study with other functionals, basis sets and solvents (see SI for details); our mechanistic

conclusions persist independent of the method used. All computed structures and coordinates can be found at the ioChem-BD repository[27] at the following DOI: https://doi.org/10.19061/iochem-bd-6-130.

3.1.4 Results

Generation of NO (and other species) from the RSSH/RS-NO reaction: As has been proposed and reported previously, the reaction of RSSH with RS-NO can lead to the formation of RSSSSR and NO[12] and reactions 1–3 have been proposed to explain these results. In this previous work, it was not determined whether other products aside from NO could also be generated. For example, although reactions 1–3 can account for R'S-NO degradation and NO liberation, it must be realized that this is not the only potential reaction pathway. Aside from the transnitrosation pathway (i.e., the transfer of the nitrosonium ion from one sulfur to another), whereby nucleophilic attack occurs at the nitrogen atom of R'S-NO, it is also known that nucleophilic attack can occur at the sulfur atom of R'S-NO.[28] This reaction is referred to as an S-thiolation. If the nucleophile is RSSH/ RSS^-, then the products would be nitroxyl (HNO) and the corresponding dialkyltrisulfide (RSSSR') (reaction 4).

$$RSSH + R'S{-}NO \rightarrow RSSSR' + HNO \qquad \text{(reaction 4)}$$

Direct analysis of HNO formation is often problematic due to rapid dimerization to give, eventually, nitrous oxide (N_2O)[29] (reaction 5).

$$2HNO \rightarrow\rightarrow N_2O + H_2O \qquad \text{(reaction 5)}$$

Indeed, due to reaction 5, the detection of N_2O can be used as an indication of the intermediacy of HNO in a chemical system.[30] Thus, membrane inlet mass spectrometry (MIMS) is used to monitor the generation of NO, N_2O and other volatile, neutral species from the reaction of an S-nitrosothiol and an RSSH species. Due to self-reactivity, hydropersulfides are inherently unstable and typically examined using persulfide donors.[31-33] Therefore, these studies are performed using an alkylamine-substituted perthiocarbamate persulfide donor **1** (Figure 3.1.1)[15] and S-nitrosoglutathione (GSNO) as the representative RS-NO species. As shown in Figure 3.1.1, RSS^- generated from the decomposition of **1** can have several

possible fates in the presence of GS-NO; pathway **A** leads to NO formation and pathway **B** results in the eventual formation of N_2O (i.e., via the intermediacy of HNO). The RSSH donor **1** has a half-life of 16.7 min in aqueous solution at pH 7.4 and 37 °C and in the absence of any other reactant, an RSSH species formed from the breakdown of **1** will react with another unreacted molecule of **1** to give the corresponding dialkyltrisulfide and a thiocarbamate intermediate, which subsequently decomposes to produce carbonyl sulfide (COS)[15] (Figure 3.1.1, pathway **C**). Thus, the generation of NO, N_2O and/or COS provide qualitative evidence for the existence/prevalence of the various pathways depicted in Figure 3.1.1.

MIMS analysis of reaction mixtures containing 100 μM GSNO and increasing concentrations of **1** (50, 100 and 200 μM) was carried out in pH 7.4 buffer, in the dark and at 37 °C shows NO generation, indicating that pathway **A** appears to predominate under all reaction conditions (Figure 3.1.2a–c). Not unexpectedly, the level of COS increases with increasing concentrations of **1** since the higher levels of **1** allow the COS forming pathway to compete (Figure 3.1.1, pathway **C**). A qualitative assessment of the amount of N_2O generated from these reactions was carried out via GC headspace analysis and comparison to a standard curve generated from Angeli's salt decomposition (i.e., Angeli's salt is an established and reliable HNO donor[34]) (Figure 3.1.2d). Based on this analysis, the yield of N_2O was approximately 13–20%, which represents approximately 26–40% of the total possible nitrogen containing products (i.e., two HNO molecules dimerize to generate one N_2O, reaction 5). To be sure, extrapolation of HNO generation by pathway **B** (Figure 3.1.1) from these reactions via the measurement of N_2O is apt to be artificially high since N_2O can also be generated in this system by the reaction of HNO with two molecules of NO (reaction 6).[35] Thus, this reaction can result in a higher apparent yield of HNO (via N_2O measurement) and an artificially low apparent yield of NO from this chemistry.

$$2NO + HNO \rightarrow N_2O + NO_2^- + H^+ \qquad \text{(reaction 6)}$$

Importantly, no H_2S was observed in these analyses (data not shown), indicating the absence of RSSH disproportionation chemistry (*vide infra*).

For comparison, the reaction of a structurally analogous thiol, *N*-acetylpenicillamine methyl ester (the thiol (RS^-/RSH) analog of RSS^- in Figure 3.1.1) with GSNO was also examined. Comparison of the results shown in Figure 3.1.2 (with RSSH + GSNO) with those of Figure 3.1.3 (RSH + GSNO) shows clear qualitative differences between the levels of NO released under these two conditions (e.g., compare the magnitudes of the y-axes). It is clear that RSS^-/RSSH is far superior to RS^-/RSH in generating NO from reaction with RS-NO. This is especially evident when considering that the formation of RSS^-/RSSH occurs slowly ($t1/2$ = 16.7 min)[15] under the conditions of these experiments due to generation via a donor species while the levels of RS^-/RSH are present from the beginning at the stated concentrations. In addition, under these reaction conditions, N_2O is not observed by GC headspace analysis, consistent with the MIMS data.

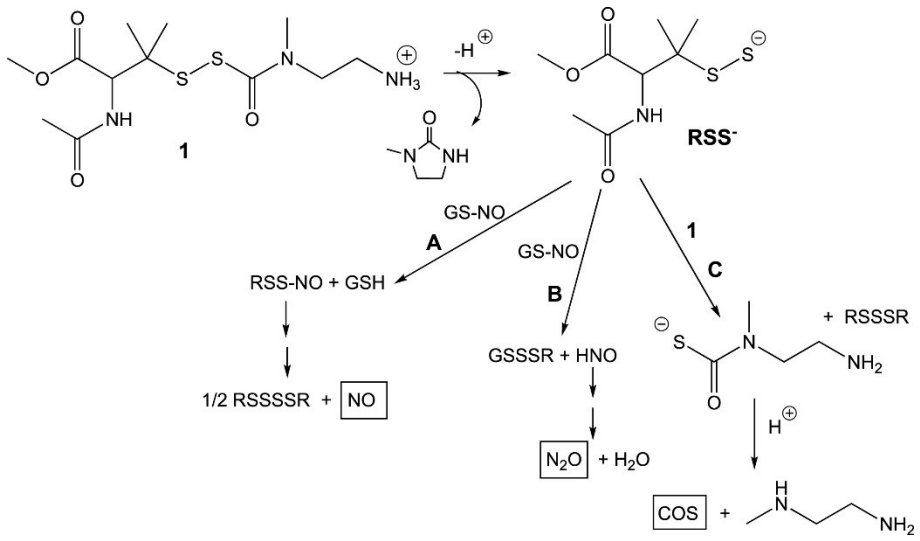

Figure 3.1.1. Possible pathways for the reaction between **1** and GS-NO. Pathway **A**: Transnitrosation between RSS^- and GS-NO and subsequent generation of NO. Pathway **B**: S-Thiolation of GS-NO by RSS^- and generation of HNO. Pathway **C**: RSS^- reaction with excess 1, leading to the eventual generation of COS.

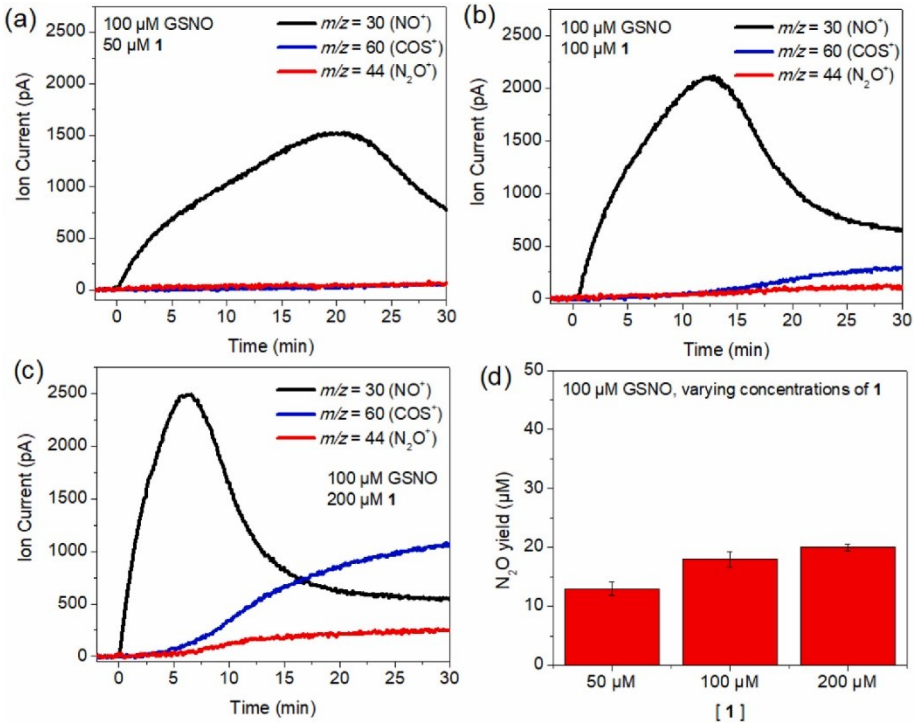

Figure 3.1.2. MIMS signals observed during the incubation of GSNO (100 μM) with (a) 50 μM, (b) 100 μM and (c) 200 μM of RSSH donor 1. m/z = 30 corresponds to NO^+, *m/z* = 60 corresponds to COS^+, and *m/z* = 44 corresponds to N_2O^+. (d) N_2O yields independently quantified via GC headspace analysis (±SD). All reactions were carried out under anaerobic conditions in PBS (pH 7.4, 100 mM) containing diethylenetriaminepentaacetic acid (DTPA) (100 μM) at 37 °C and protected from light.

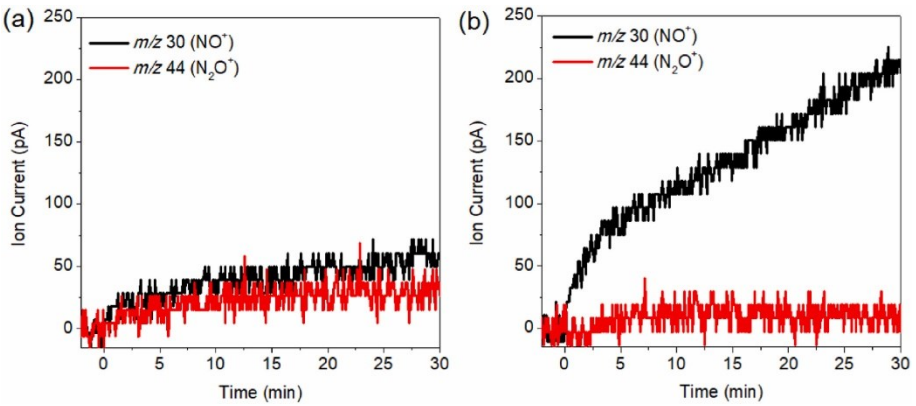

Figure 3.1.3. MIMS analysis of the reaction of 100 μM GSNO with *N*-acetyl penicillamine methyl ester at (a) 50 μM and (b) 200 μM. Reaction carried out under same conditions as described for the experiments shown in Figure 3.1.2.

Computational analysis of the RSSH/RS-NO reaction: To gain further insight into the reaction of RSSH with R'S-NO, a series of computational studies were performed at the SMD(H2O)-M06-2X/def2-SVP//M06-2X/ def2-SVP level. The deprotonation of RSSH followed by attack of the nucleophile RSS^- on the nitrogen of R'S-NO yields the formation of an S-nitrosopersulfide intermediate (RSS-NO). This reaction is predicted to be endergonic by 4.2 kcal mol^{-1} and is reversible which can be attributed to RSS^- being a better nucleophile compared to RS^- a due to a mild α-effect.[31] RSS-NO is kinetically and thermodynamically unstable at room temperature (S–N bond length is 1.9 Å, BDE = approx. 4 kcal mol^{-1})[12] and thus, it readily dissociates into perthiyl radical (RSS·) and nitric oxide (NO). The relatively stable RSS· species are non-oxidizing in contrast to their RS· counterparts due to delocalization of the odd electron,[12-14,31] but can dimerize to form dialkyltetrasulfide (RSSSSR) which is predicted to be exergonic by ~20 kcal mol^{-1} (Figure 3.1.1, and Fig 3.1.4, pathway **A**).

As discussed previously, there is an alternative pathway for these reactants. Pathway **B** (Figure 3.1.1) generates HNO instead of NO via RSSH attack on the sulfur of R'S-NO to form RSSSR' and HNO.[28] This S-thiolation reaction involves a proton transfer from RSSH to the nitrogen of R'S-NO followed by an asynchronous event of S–S bond formation and HNO liberation. (A proton transfer to the nitrogen of R'S-

NO is more favorable than a proton transfer to the oxygen of R'S-NO. See SI for details.) The barrier for the formation of RSSSR and HNO is quite high and predicted to be 52.4 kcal mol^{-1} with respect to the sum of separate reactant energies. However, the energy profile of the S-thiolation reaction shown in Figure 3.1.4 (pathway **b**) indicates that the bulk of the barrier is due to the proton transfer event, which is unfavorable without an explicit polar solvent (or enzymatic) environment; note that from the second structure shown, where the proton has largely transferred to nitrogen, the remaining barrier is only ~10 kcal mol^{-1} (We incorporated continuum water and chloroform via single point energy calculations. See SI for details). Thus, if the *N*-protonated R'S-NO and RSS^{-} are readily available, the S-thiolation step would be highly favorable with a small barrier at most.

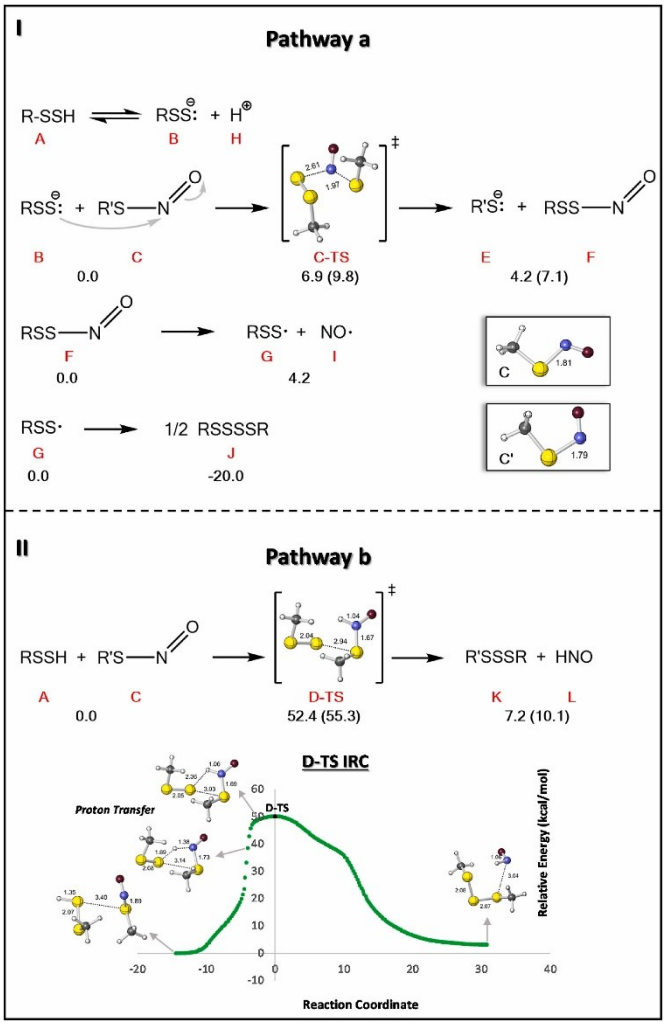

Figure 3.1.4. I. Computed ([*SMD*-H2O]-M06-2X/def2-SVP//M06-2X/def2-SVP) relative free energies (kcal mol^{-1}) for minima and TSSs involved in pathway **a**. There are two conformers of C (C and C′). Energies in the parenthesis are relative to the sum of the energies of C′ and B, whereas the energies without the parenthesis are relative to the sum of the energies of C and B. II. *On top:* Computed ([*SMD*-H2O]-M06-2X/def2-SVP//M06-2X/def2-SVP) relative free energies (kcal mol^{-1}) for minima and TSSs involved in pathway **b**. There are two conformers of C (C and C′). Energies in the parenthesis are relative to the sum of the energies of C′ and A, whereas the energies without the parenthesis are relative to the sum of the energies of C and A. *At the bottom:* The electronic energy profile of the D-TS (M06-2X/def2-SVP). The D-TS is located where x = 0 on the plot. The electronic energy at each point in the IRC is relative to the electronic energy of the reactant complex (kcal mol^{-1}). The electronic energy barrier after the proton transfer is 0.5 kcal mol^{-1}. The bond distances are in Å. (R = R' = CH_3).

The S-thiolation with simple thiols (RSH) has been previously studied by Timerghazin and co-workers who found a similar reaction path.[36] To compare the role of RSSH versus RSH in the reaction, we reproduced their S-thiolation analysis (Figure 3.1.5, top) (energies differ slightly from Timerghazin's energies due to the difference in the choice of level of theory.) The energy profile for the HNO generating reaction shows a high barrier as expected since it again includes the energy needed for the proton transfer (Figure 3.1.5, bottom). The electronic energy (M06-2X/def2-SVP) barrier for the S-thiolation reaction after the proton transfer is 3.6 kcal mol^{-1}. Hence, once the proton of RSSH or RSH species is transferred to the nitrogen of RS-NO, the HNO generation reaction becomes viable. However, inspection of the reaction pathways indicates that the barrier remaining after proton transfer is less for the system with two sulfurs, although both are small.

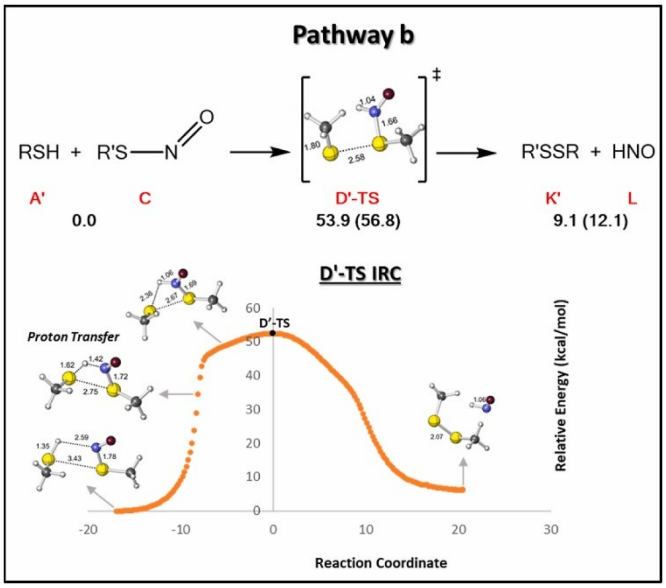

Figure 3.1.5. *On top:* Computed ([*SMD*-H2O]-M06-2X/def2-SVP//M06-2X/def2-SVP) relative free energies (kcal mol^{-1}) for minima and TSSs involved in pathway **b**. There are two conformers of C (C and C′). Energies in the parenthesis are relative to the sum of the energies of C′ and A′, whereas the energies without the parenthesis are relative to the sum of the energies of C and A'. *At the bottom:* The electronic energy profile of the D′-TS (M06-2X/def2-SVP). The D′-TS is located where x = 0 on the plot. The electronic energy at each point in the IRC is relative to the electronic energy of the reactant complex (kcal mol^{-1}). The electronic energy barrier after the proton transfer is 3.6 kcal mol^{-1}. The bond distances are in Å. (R = R' = CH_3).

Vasorelaxation resulting from the RSSH/RS-NO reaction: As an extremely potent vasorelaxant, the presence of NO can be readily detected using a vascular tissue bath assay. Thus, if the RSSH/RS'-NO reaction liberates NO, this should result in the relaxation of vascular tissue. In order to test this idea, the effect of vascular tissue pre-treatment with the nitrosonium (NO^+) donor *S*-nitroso-*N*-acetylpenicillamine (SNAP), which will transnitrosate cellular thiols resulting in cellular RSNO species,[37] on persulfide-mediated vasorelaxation was examined. As shown in Figure 3.1.6, the persulfide donors cysteine trisulfide (CysSSSCys, an established donor of Cys-SSH in cells)[38] and RSSH donor **1** both exhibited significantly increased vasorelaxant potency in murine aorta after pre-treatment with SNAP (30 min incubation followed

by washout) (10 μM).[15] Moreover, the concentration-dependent relaxations to SNAP were enhanced by pre-treatment with CysSSSCys and, to a lesser extent, by **1** (Figure 3.1.6C, D).

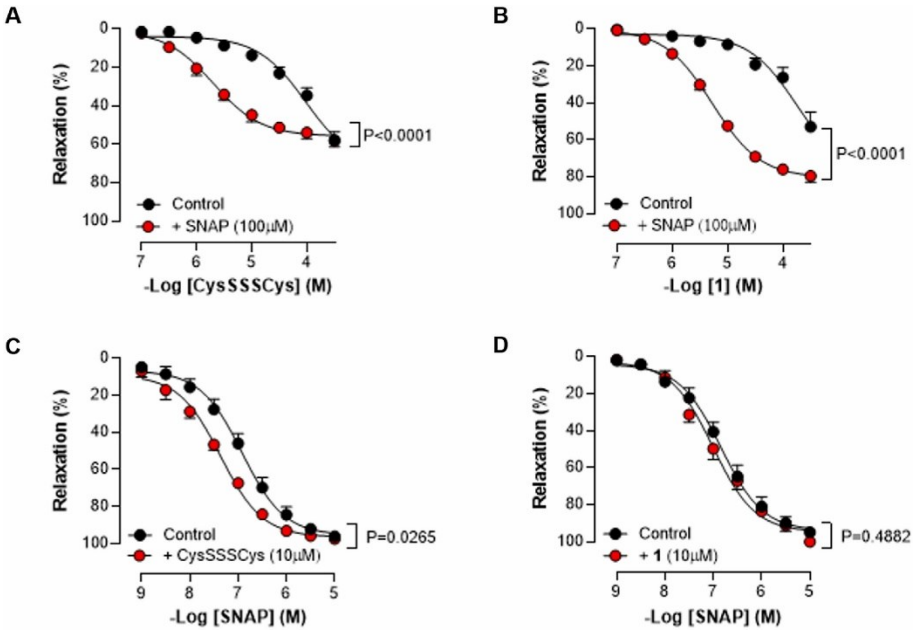

Figure 3.1.6. Concentration-response curves to CysSSSCys (A) or RSSH donor 1 (B) in the absence and presence of SNAP (100 μM). Concentration-response curves to SNAP (C, D) in the absence and presence of CysSSSCys (10 μM; C) or 1 (10 μM; D). Data are expressed as mean ± sem with statistical analysis conducted by two-way analysis of variance. n = 8.

Although modestly potent, both RSSH donors CysSSSCys and **1** alone (i.e., no SNAP pre-treatment) exhibited vasorelaxant properties (Figure 3.1.6A, B, control). This effect may be the result of liberation of NO from endogenous sources of intracellular R'SNO via reaction with RSSH. To this end, further studies were conducted with CysSSSCys to determine the mechanism(s) underpinning this inherent vasorelaxation activity. Interestingly, the vasorelaxant response to CysSSSCys was significantly inhibited in the presence of the NO synthase inhibitor L-nitroarginine methyl ester[39] (L-NAME, 300 μM; Figure 3.1.7A) and by endothelial denudation (Figure 3.1.7B). In addition, the relaxant effects of CysSSSCys were significantly

attenuated in the presence of the sGC inhibitor ODQ or in tissues from sGC knockout mice (Figure 3.1.7C, D). These findings are consistent with the idea that CysSSSCys (via formation of RSSH) is able to liberate NO from endogenous 'stores' which in turn elicits vasorelaxation via an sGC/cGMP-dependent process.

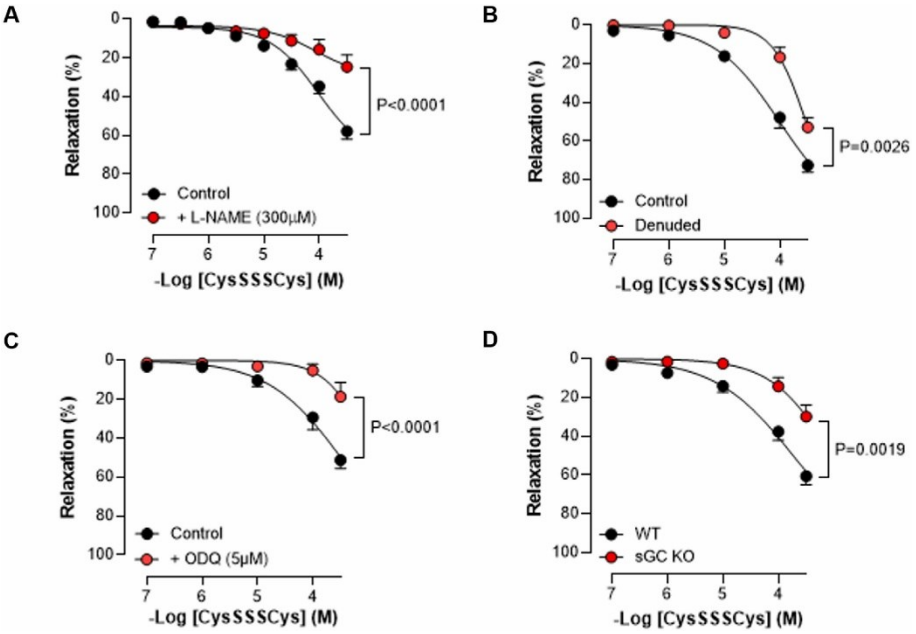

Figure 3.1.7. Concentration-response curves to CysSSSCys in the absence and presence of the NO synthase inhibitor L-NAME (300 μM; A), endothelial denudation (B), the sGC inhibitor ODQ (5 μM; C) or in wild type (WT) and sGC knockout (KO) mice (D). Data are expressed as mean ± sem with statistical analysis conducted by two-way analysis of variance. n = 8.

In vivo hypotensive actions: In order to test the idea that RSSH species may facilitate vasodilation (possibly via an RSSH/R'SNO interaction) in an *in vivo* model, CysSSSCys and **1**, along with the established and clinically relevant NO-donor sodium nitroprusside (SNP), were administered to anaesthetized mice and blood pressure monitored. All treatments produced a dose-dependent reduction in mean arterial blood pressure (MABP; Figure 3.1.8). The potency of the NO donor was approximately three orders of magnitude greater than either persulfide donor.

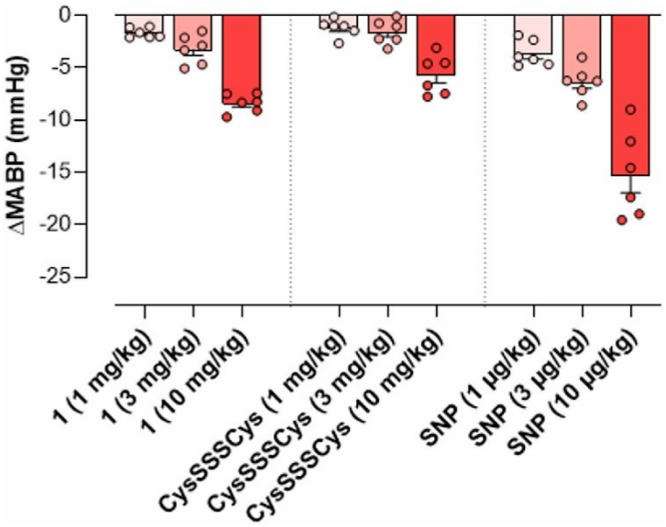

Figure 3.1.8. Dose-dependent reductions in mean arterial blood pressure (MABP) in response to bolus, intravenous administration of **1**, CysSSSCys and sodium nitroprusside (SNP). n = 8.

3.1.5 Discussion

Herein, it is confirmed that RSSH has a great potential to react with R'S-NO species. This is not surprising since the electrophilic R'S-NO readily transnitrosates with nucleophilic RS^-/RSH species (although this is not a particularly fast reaction, k = 5 - 170 $M^{-1}s^{-1}$, depending on the nature of the reactants[37]) (reaction 7) and RSSH is a far superior nucleophile compared to RSH.

$$RS\text{–}NO + R'SH \rightleftharpoons RSH + R'S\text{–}NO \qquad \text{(reaction 7)}$$

Previous work by Timerghazin and co-workers[36] on the RSH/R'SNO transnitrosation/S-thiolation reactions indicates that a competing S-thiolation reaction (reaction 8) can also occur but is heavily dependent on a proton transfer event (or proper protonation states of the reactants) to facilitate reaction at sulfur (instead of at nitrogen as is the case for transnitrosation).

$$RS\text{–}NO + R'SH \rightleftharpoons RSSR' + HNO \qquad \text{(reaction 8)}$$

That is, the S-thiolation reaction is disfavored versus transnitrosation without specific catalysis or conditions that would facilitate protonation on the RS-NO nitrogen (to increase electrophilicity of the sulfur atom) and deprotonation of RSH (to increase nucleophilicity). Without these specific protonation-deprotonation events, S-thiolation and, therefore, HNO generation from this reaction is not favored.

In the analogous reaction to the RSH/R'S-NO reaction described immediately above, the RSSH/R'S-NO reaction can also follow two pathways: transnitrosation (pathway **A**, Figure 3.1.1) and S-thiolation (pathway **B**, Figure 3.1.1). Unlike transnitrosation in the RSH/R'S-NO reaction (which simply produces another RS-NO species and is readily reversible), the RSSH/R'S-NO transnitrosation reaction generates a distinct and fleeting intermediate, RSS-NO, which can spontaneously homolyze to give NO and the perthiyl radical, RSS· (reaction 2). Under purely chemical conditions, dimerization of RSS· occurs to generate RSSSSR and thus this process can be considered to be essentially irreversible.[12-14] Experimental results analyzing the small molecule products of the RSSH/R'S-NO reaction show a predominance of NO formed with lesser amounts of HNO (as measured by N_2O formation), (Figure 3.1.2). As mentioned previously, HNO generation is undoubtedly overestimated in these experiments due to alternative pathways for N_2O formation besides simple HNO dimerization (e.g., reaction 6). This result is consistent with the idea that transnitrosation between R'S-NO and RSSH not only occurs readily, but also results in the generation of free NO. Importantly, a comparison of RSH and RSSH reaction with R'S-NO shows significantly less (approximately 10–30 fold) NO generated (comparing the results of Figure 3.1.2a, c and 3a, b). Also, it should be stressed that in these experiments RSSH is generated using a donor species with a $t_{1/2}$ of approximately 16.7 min under the conditions of these experiments. Thus, the levels of RSSH build up over time and will never be as high as the stated concentrations of the donor. However, in the experiments using RSH, the thiol exists at the stated initial concentration. Thus, in the comparison of NO formation from the RSH/R'S-NO versus RSSH/R'S-NO reactions, the NO-forming capacity of the RSSH/R'S-NO reaction is likely to be significantly greater than the 10-30 fold differences observed in these experiments.

Computational analysis of the RSSH/R'S-NO reaction also indicates a favored transnitrosation reaction, leading to NO generation (Figure 3.1.1, pathway **a**), as opposed to an S-thiolation reaction, that leads to HNO formation (Figure 3.1.1, pathway **b**). However, it is also determined that the HNO-forming S-thiolation reaction with RSSH is more favorable than the HNO-forming S-thiolation reaction with RSH. The primary impedance for S-thiolation for the RSSH/R'S-NO reaction is the unfavorable and requisite proton transfer event (or the requirement for specific protonation on the nitrogen of R'S-NO and the deprotonation of the attacking RSSH). This result is entirely consistent with the results previously reported by Timerghazin et al.[36] for the RSH/R'S-NO reaction. It should be stressed, however, that the relative favorability of these reactions will be highly dependent on the pH, reactant ratios, sterics and specific protonation events (e.g., that may occur within specific protein environments). Thus, in a biological milieu or at specific protein sites, either pathway may be viable (albeit all things being equal, the transnitrosation pathway appears favorable).

As stated earlier, R'S-NO species have been proposed to be storage forms and/or reservoirs of NO that can be liberated to, for example, control vascular tone.[40,41] In the case of possible NO liberation from an S-nitrosothiol on hemoglobin, a novel electron transfer from a deoxygenated ferrous heme to the S-nitrosothiol function has been proposed as a possible mechanism of NO liberation.[42,43] However, in cases where this possibility does not exist (i.e., in cases lacking a nearby ferrous iron), reasonable mechanisms for NO liberation from RS-NO remain unestablished. Herein using vasorelaxation as a biologically relevant and specific detector of NO, it is shown that smooth muscle tissues pre-loaded with R'S-NO (via pre-treatment with the S-nitrosothiol SNAP) exhibit a marked increase in RSSH-mediated vasorelaxation (Figure 3.1.6A, B); likewise, the vasorelaxant activity of SNAP is enhanced by RSSH pretreatment (Figure 3.1.6C, D). These observations support a mechanism dependent on NO release via reactions 1 and 2. This concept was confirmed by establishing that the vasorelaxant actions of RSSH were blocked in the presence of sGC inhibition (with ODQ) and in tissues from sGC KO mice (Figure 3.1.7C, D). Importantly, in vascular tissue that is not pre-treated with an S-nitrosothiol, RSSH still has vasorelaxant properties, albeit with a

much decreased potency compared to R'S-NO pretreated tissues. Interestingly, the vasorelaxant properties of RSSH are markedly diminished in the presence of an NOS inhibitor and following endothelial denudation (Figure 3.1.7A, B), implicating endogenous NO biosynthesis in at least some of the vasorelaxant effects associated RSSH. At this time, this effect is not fully understood. However, it can be speculated that some portion of NOS-derived NO results in R'S-NO formation (thereby intimating a dynamic endogenous synthetic pathway) and therefore inhibition of NOS decreases R'S-NO and therefore, diminishes the effect of exogenous RSSH. It is important to note that the vasorelaxant properties of S-nitrosocysteine can be enhanced by the presence of Cys-SH.[44] However, our chemical studies comparing the ability of RSH and RSSH to release NO via reaction with R'S-NO would predict that RSSH would be much more potent in this regard (compare Figure 3.1.2a with Figure 3.1.3a). Regardless, this study presents the possibility that RSSH species are capable of degrading R'S-NO in biological tissues with subsequent liberation of NO, as indicated by a vasorelaxant response. Furthermore, consistent with the idea that RSSH can serve to liberate NO from endogenous R'S-NO sources, leading to vasorelaxation, RSSH species are shown to possess vasorelaxant properties *in vivo* in anaesthetized mice (Figure 3.1.8).

R'S-NO species have also been proposed to be deleterious. For example, aberrant overproduction of NO, leading to excessive R'S-NO formation in critical proteins has been implicated in the etiology of neurodegenerative disease[5] and cancer[6]. As such, processes that regulate steady-state R'S-NO levels in cells become of considerable interest with regards to the development of possible disease therapies. As mentioned previously, RSSH are oxidized with respect to RSH and therefore may be expected to be more prevalent under oxidizing cellular conditions.[11] As RSSH are superior nucleophiles and reductants compared to the corresponding RSH species, their biological generation presents the scenario that a superior reductant is generated primarily during oxidative stress conditions and therefore can serve a protective role. Importantly, this idea has experimental support from studies reporting protective actions of RSSH against oxidative and/or electrophilic stress.[33,38,45-50] Thus, R'S-NO species generated under oxidative stress conditions (consider that R'S-NO species are also oxidized with respect to RSH) may be particularly

susceptible to destruction by the RSSH chemistry described herein. Thus, in this way, endogenous RSSH generation may serve to protect a cell from aberrant and potentially harmful RS-NO formation. To be sure, R'S-NO species are also proposed as normal physiological signaling agents and even protectants against RSH overoxidation.[51] Thus, the generation of an R'S-NO reactive species, such as RSSH, may only be beneficial under conditions of an over-production and potentially deleterious levels of R'S-NO, such as may be the case under oxidative stress.

3.1.6 Acknowledgements

The authors thank the NSF XSEDE program for computational support. The authors also thank David Wink, Yoshito Kumagai and Taka Akaike for their helpful discussions.

3.1.7 Supporting Information

Supplementary data to this article can be found online at https://doi.org/10.1016/j.freeradbiomed.2022.06.245.

3.1.8 References

(1) Rayner, B. S.; Wu, B. J.; Raftery, M.; Stocker, R.; Witting, P. K. Human S-Nitroso Oxymyoglobin Is a Store of Vasoactive Nitric Oxide. *J. Biol. Chem.* **2005**, *280*, 9985–9993.
(2) Singel, D. J.; Stamler, J. S. Chemical Physiology of Blood Flow Regulation by Red Blood Cells: The Role of Nitric Oxide and S-Nitrosohemoglobin. *Annu. Rev. Physiol*. **2005**, *67*, 99–145.
(3) Ignarro, L. J.; Lippton, H. L.; Edwards, J. C. Mechanism of Vascular Smooth Muscle Relaxation by Organic Nitrates, Nitrites and Nitroprusside: Formation of Potent, Unstable, S-Nitrosothiol Metabolites. *J. Pharmacol. Exp. Therapeut.* **1981**, *218,* 739-749.
(4) Nakamura, T.; Prikhodko, O. A.; Pirie, E.; Nagar, S.; Akhtar, M. W.; Oh, C. K.; McKercher, S. R.; Ambasudhan, R.; Okamoto, S. ichi; Lipton, S. A. Aberrant Protein S-Nitrosylation Contributes to the Pathophysiology of Neurodegenerative Diseases. *Neurobiol. Dis*. **2015**, *84*, 99–108.
(5) Nakamura, T.; Lipton, S. A. 'SNO'-Storms Compromise Protein Activity and Mitochondrial Metabolism in Neurodegenerative Disorders. *Trends Endocrinol. Metabol.* **2017**, *28*, 879–892.
(6) Ehrenfeld, P.; Cordova, F.; Duran, W. N.; Sanchez, F. A. S-Nitrosylation and Its Role in Breast Cancer Angiogenesis and Metastasis. *Nitric Oxide* **2019**, *87*, 52–59.
(7) Rizza, S.; Filomeni, G. Exploiting S-Nitrosylation for Cancer Therapy: Facts and Perspectives. *Biochem. J.* **2020**, *477*, 3649–3672.
(8) Fukuto, J. M.; Perez-Ternero, C.; Zarenkiewicz, J.; Lin, J.; Hobbs, A. J.; Toscano, J. P. Hydropersulfides (RSSH) and Nitric Oxide (NO) Signaling: Possible Effects on S-Nitrosothiols (RS-NO). *Antioxidants* **2022**, *11*, 169.
(9) Toohey, J. I.; Cooper, A. J. L. Thiosulfoxide (Sulfane) Sulfur: New Chemistry and New Regulatory Roles in Biology. *Molecules* **2014**, *19*, 12789–12813.

(10) Fukuto, J. M.; Ignarro, L. J.; Nagy, P.; Wink, D. A.; Kevil, C. G.; Feelisch, M.; Cortese-Krott, M. M.; Bianco, C. L.; Kumagai, Y.; Hobbs, A. J.; Lin, J.; Ida, T.; Akaike, T. Biological Hydropersulfides and Related Polysulfides – a New Concept and Perspective in Redox Biology. *FEBS Lett.* **2018**, *592*, 2140–2152.
(11) Fukuto, J. M.; Hobbs, A. J. A Comparison of the Chemical Biology of Hydropersulfides (RSSH) with Other Protective Biological Antioxidants and Nucleophiles. *Nitric Oxide* **2021**, *107*, 46–57.
(12) Bianco, C. L.; Chavez, T. A.; Sosa, V.; Saund, Simran, S.; Nguyen, Q. N. N.; Tantillo, D. J.; Ichimura, A. S.; Toscano, J. P.; Fukuto, J. M. The Chemical Biology of the Persulfide (RSSH)/Perthiyl (RSS·) Redox Couple and Possible Role in Biological Redox Signaling. *Free Radic. Biol. Med.* **2016**, *101*, 20–31.
(13) Everett, S. A.; Wardman, P. Perthiols as Antioxidants: Radical-Scavenging Andprooxidative Mechanisms. *Methods Enzymol*. **1995**, *251*, 55–69.
(14) Chauvin, J. P. R.; Griesser, M.; Pratt, D. A. Hydropersulfides: H-Atom Transfer Agents Par Excellence. *J. Am. Chem. Soc.* **2017**, *139*, 6484–6493.
(15) Khodade, V. S.; Pharoah, B. M.; Paolocci, N.; Toscano, J. P. Alkylamine-Substituted Perthiocarbamates: Dual Precursors to Hydropersulfide and Carbonyl Sulfide with Cardioprotective Actions. *J. Am. Chem. Soc.* **2020**, *142*, 4309–4316.
(16) Chavez, T.A.; Toscano, J.P. Detection of HNO by Membrane Inlet Mass Spectrometry. In *The Chemistry And Biology of Azanone (HNO)*; Marti, M.A.; Doctorovich, F.; Farmer, P., Eds.; Elsevier Ltd., 2017; pp 255–267.
(17) Zarenkiewicz, J.; Khodade, V. S.; Toscano, J. P. Reaction of Nitroxyl (HNO) with Hydrogen Sulfide and Hydropersulfides. *J. Org. Chem.* **2021**, *86*, 868–877.
(18) Frisch, M. J.; Trucks, G. W.; Schlegel, H. B.; Scuseria, G. E.; Robb, M. A.; Cheeseman, J. R.; Scalmani, G.; Barone, V.; Petersson, G. A.; Nakatsuji, H., et al. *Gaussian 16,* Revision A.03.; Gaussian, Inc.: Wallingford, CT, 2016.
(19) Marenich, A. V.; Cramer, C. J.; Truhlar, D. G. Universal Solvation Model Based on Solute Electron Density and on a Continuum Model of the Solvent Defined by the Bulk Dielectric Constant and Atomic Surface Tensions. *J. Phys. Chem. B* **2009**, *113*, 6378–6396.
(20) Weigend, F.; Ahlrichs, R. Balanced Basis Sets of Split Valence, Triple Zeta Valence and Quadruple Zeta Valence Quality for H to Rn: Design and Assessment of Accuracy. *Phys. Chem. Chem. Phys.* **2005**, *7*, 3297–3305.
(21) Weigend, F. Accurate Coulomb-Fitting Basis Sets for H to Rn. *Phys. Chem. Chem. Phys.* **2006**, *8*, 1057–1065.
(22) Zhao, Y.; Truhlar, D. G. Density Functionals with Broad Applicability in Chemistry. *Acc. Chem. Res.* **2008**, *41*, 157–167.
(23) Mardirossian, N.; Head-Gordon, M. How Accurate Are the Minnesota Density Functionals for Noncovalent Interactions, Isomerization Energies, Thermochemistry, and Barrier Heights Involving Molecules Composed of Main-Group Elements? *J. Chem. Theory Comput.* **2016**, *12*, 4303–4325.
(24) Gonzalez, C.; Schlegel, H. B. Reaction Path Following in Mass-Weighted Internal Coordinates. *J. Phys. Chem.* **1990**, *94*, 5523–5527.
(25) Fukui, K. The Path of Chemical Reactions - the IRC Approach. *Acc. Chem. Res.* **1981**, *14*, 363–368.
(26) Maeda, S.; Harabuchi, Y.; Ono, Y.; Taketsugu, T.; Morokuma, K. Intrinsic Reaction Coordinate: Calculation, Bifurcation, and Automated Search. *Int. J. Quantum Chem.* **2015**, *115*, 258–269.
(27) Álvarez-Moreno, M.; De Graaf, C.; López, N.; Maseras, F.; Poblet, J. M.; Bo, C. Managing the Computational Chemistry Big Data Problem: The ioChem-BD Platform. *J. Chem. Inf. Model.* **2015**, *55*, 95–103.
(28) Wong, P. S. Y.; Hyun, J.; Fukuto, J. M.; Shirota, F. N.; DeMaster, E. G.; Shoeman, D. W.; Nagasawa, H. T. Reaction between S-Nitrosothiols and Thiols: Generation of Nitroxyl (HNO) and Subsequent Chemistry. *Biochemistry* **1998**, *37*, 5362–5371.
(29) Kohout, F. C.; Lampe, F. W. On the Role of the Nitroxyl Molecule in the Reaction of Hydrogen Atoms with Nitric Oxide. *J. Am. Chem. Soc.* **1965**, *87*, 5795–5796.

(30) Bonner, F. T.; Ravid, B. Thermal Decomposition of Oxyhyponitrite (Sodium Trioxodinitrate(II)) in Aqueous Solution. *Inorg. Chem.* **1975**, *14*, 558–563.
(31) Ono, K.; Akaike, T.; Sawa, T.; Kumagai, Y.; Wink, D. A.; Tantillo, D. J.; Hobbs, A. J.; Nagy, P.; Xian, M.; Lin, J.; Fukuto, J. M. Redox Chemistry and Chemical Biology of H_2S, Hydropersulfides, and Derived Species: Implications of Their Possible Biological Activity and Utility. *Free Radic. Biol. Med.* **2014**, *77*, 82–94.
(32) Dillon, K. M.; Matson, J. B. A Review of Chemical Tools for Studying Small Molecule Persulfides: Detection and Delivery. *ACS Chem. Biol.* **2021**, *16*, 1128–1141.
(33) Khodade, V. S.; Aggarwal, S. C.; Eremiev, A.; Bao, E.; Porche, S.; Toscano, J. P. Development of Hydropersulfide Donors to Study Their Chemical Biology. *Antioxid. Redox Signal.* **2022**, *36*, 309–326.
(34) King, S. B.; Nagasawa, H. T. Chemical Approaches toward Generation of Nitroxyl. *Methods Enzymol.* **1998**, *301*, 211–228.
(35) Miranda, K. M. The Chemistry of Nitroxyl (HNO) and Implications in Biology. *Coord. Chem. Rev.* **2005**, *249*, 433–455.
(36) Ivanova, L. V.; Cibich, D.; Deye, G.; Talipov, M. R.; Timerghazin, Q. K. Modeling of S-Nitrosothiol–Thiol Reactions of Biological Significance: HNO Production by S-Thiolation Requires a Proton Shuttle and Stabilization of Polar Intermediates. *ChemBioChem* **2017**, *18*, 726–738.
(37) Hogg, N. The Kinetics of S-Transnitrosation—A Reversible Second-Order Reaction. *Anal. Biochem.* **1999**, *272*, 257–262.
(38) Bianco, C. L.; Akaike, T.; Ida, T.; Nagy, P.; Bogdandi, V.; Toscano, J. P.; Kumagai, Y.; Henderson, C. F.; Goddu, R. N.; Lin, J.; Fukuto, J. M. The Reaction of Hydrogen Sulfide with Disulfides: Formation of a Stable Trisulfide and Implications for Biological Systems. *Br. J. Pharmacol.* **2019**, *176*, 671–683.
(39) Fukuto, J. M.; Chaudhuri, G. Inhibition of Constitutive and Inducible Nitric Oxide Synthase: Potential Selective Inhibition. *Annu. Rev. Pharmacol. Toxicol.* **1995**, *35*, 165–194.
(40) Ng, E. S. M.; Kubes, P. The Physiology of S-Nitrosothiols: Carrier Molecules for Nitric Oxide. *Can. J. Physiol. Pharmacol*. **2003**, *81*, 759–764.
(41) Rodriguez, J.; Maloney, R. E.; Rassaf, T.; Bryan, N. S.; Feelisch, M. Chemical Nature of Nitric Oxide Storage Forms in Rat Vascular Tissue. *Proc. Natl. Acad. Sci. U. S. A.* **2003**, *100*, 336–341.
(42) Pezacki, J. P.; Ship, N. J.; Kluger, R. Release of Nitric Oxide from S-Nitrosohemoglobin. Electron Transfer as a Response to Deoxygenation. *J. Am. Chem. Soc.* **2001**, *123*, 4615–4616.
(43) Ship, N. J.; Pezacki, J. P.; Kluger, R. Rates of Release of Nitric Oxide from HbSNO and Internal Electron Transfer. *Bioorg. Chem.* **2003**, *31*, 3–10.
(44) Feelisch, M.; Te Poel, M.; Zamora, R.; Deussen, A.; Moncada, S. Understanding the Controversy over the Identity of EDRF. *Nature* **1994**, *368*, 62–65.
(45) Ida, T.; Sawa, T.; Ihara, H.; Tsuchiya, Y.; Watanabe, Y.; Kumagai, Y.; Suematsu, M.; Motohashi, H.; Fujii, S.; Matsunaga, T.; Yamamoto, M.; Ono, K.; Devarie-Baez, N. O.; Xian, M.; Fukuto, J. M.; Akaike, T. Reactive Cysteine Persulfides and S-Polythiolation Regulate Oxidative Stress and Redox Signaling. *Proc. Natl. Acad. Sci. U. S. A.* **2014**, *111*, 7606–7611.
(46) Greiner, R.; Pálinkás, Z.; Bäsell, K.; Becher, D.; Antelmann, H.; Nagy, P.; Dick, T. P. Polysulfides Link H2S to Protein Thiol Oxidation. *Antioxid. Redox Signal.* **2013**, *19*, 1749–1765.
(47) Powell, C. R.; Dillon, K. M.; Wang, Y.; Carrazzone, R. J.; Matson, J. B. A Persulfide Donor Responsive to Reactive Oxygen Species: Insights into Reactivity and Therapeutic Potential. *Angew. Chem. Int. Ed.* **2018**, *57*, 6324–6328.
(48) Ezeriņa, D.; Takano, Y.; Hanaoka, K.; Urano, Y.; Dick, T. P. N-Acetyl Cysteine Functions as a Fast-Acting Antioxidant by Triggering Intracellular H2S and Sulfane Sulfur Production. *Cell Chem. Biol.* **2018**, *25*, 1-13.
(49) Zhang, T.; Ono, K.; Tsutsuki, H.; Ihara, H.; Islam, W.; Akaike, T.; Sawa, T. Enhanced Cellular Polysulfides Negatively Regulate TLR4 Signaling and Mitigate Lethal Endotoxin Shock. *Cell Chem. Biol.* **2019**, *26*, 1-13.

(50) Henderson, C. F.; Bica, I.; Long, F. T.; Irwin, D. D.; Stull, C. H.; Baker, B. W.; Suarez Vega, V.; Taugher, Z. M.; Fletes, E. D.; Bartleson, J. M.; Humphrey, M. L.; Álvarez, L.; Akiyama, M.; Kumagai, Y.; Fukuto, J. M.; Lin, J. Cysteine Trisulfide Protects E. Coli from Electrophile-Induced Death through the Generation of Cysteine Hydropersulfide. *Chem. Res. Toxicol.* **2020**, *33*, 678–686.
(51) Sun, J.; Steenbergen, C.; Murphy, E. S-Nitrosylation: NO-Related Redox Signaling to Protect Against Oxidative Stress. *Antioxid. Redox Signal.* **2006**, *8*, 1693–1705.

3.2. Mechanistic Investigation of the Formation of Zwiebelanes Isolated from Onions

3.2.1 Introduction

Onions do complex chemistry. This vegetable (*Allium cepa* L.) is a prominent member of the genus *Allium* and has interested chemists, biologists and botanists for ages due its wide variety of uses in medicine and food industries.[1–4] The zwiebelanes (Scheme 3.2.1) constitute one class of biologically active natural products isolated from onion bulbs, their discovery arising from a search for antiasthmatic agents.[5–8] On the basis of spectroscopic analysis, the zwiebelanes were characterized as diastereoisomeric cyclic organosulfur compounds, 2,3-dimethyl-5,6-dithiabicyclo[2.1.1]hexane 5-oxides.[5,9]

Our interest in the zwiebelanes arose out of consideration of the chemical mechanisms by which they might be formed in Nature (Scheme 3.2.1) and our interest in characterizing such mechanisms using computational quantum chemistry.[10–12]

Previous experimental studies[5,8] suggested that when onion is cut, allinase enzymes transform isoalliin (**1**) to the onion lachrymatory factor[13,14] propanethial S-oxide (**3**) through a rearrangement of 1-propenesulfenic acid (**2**).[6-9] Alk(en)yl 1-propenethiosulfinates (**4**) are believed to form concomitantly via condensation of **2** with sulfenic acids; **4** act as the main flavorants in onion.[15] Dimerization of **2** coupled to loss of water can afford **6** which can then be converted to the zwiebelanes (**10/11**). In the laboratory, **6** can be formed via oxidation of disulfide (**5**). The (*E,Z*)/(*Z,E*) isomers of **6** affords natural product **10a** whereas (*Z,Z*) isomers would afford natural product **11a**.[5,8] Compound **6** can undergo a [3,3]-sigmatropic shift to yield **7**, which could form bicyclic sultene **8** via 1,3-dipolar cycloaddition. While further rearrangement of **8** may result in **10/11**, it was also suggested that **7** can undergo intramolecular (2+2) cycloaddition to form **10/11** directly.[5,8] Here we describe the results of density functional theory (DFT) calculations that prompt us to propose a different mechanism for zwiebelane A (**10a**) formation.

Scheme 3.2.1. Mechanism of the formation of zwiebelanes and related compounds.[5]

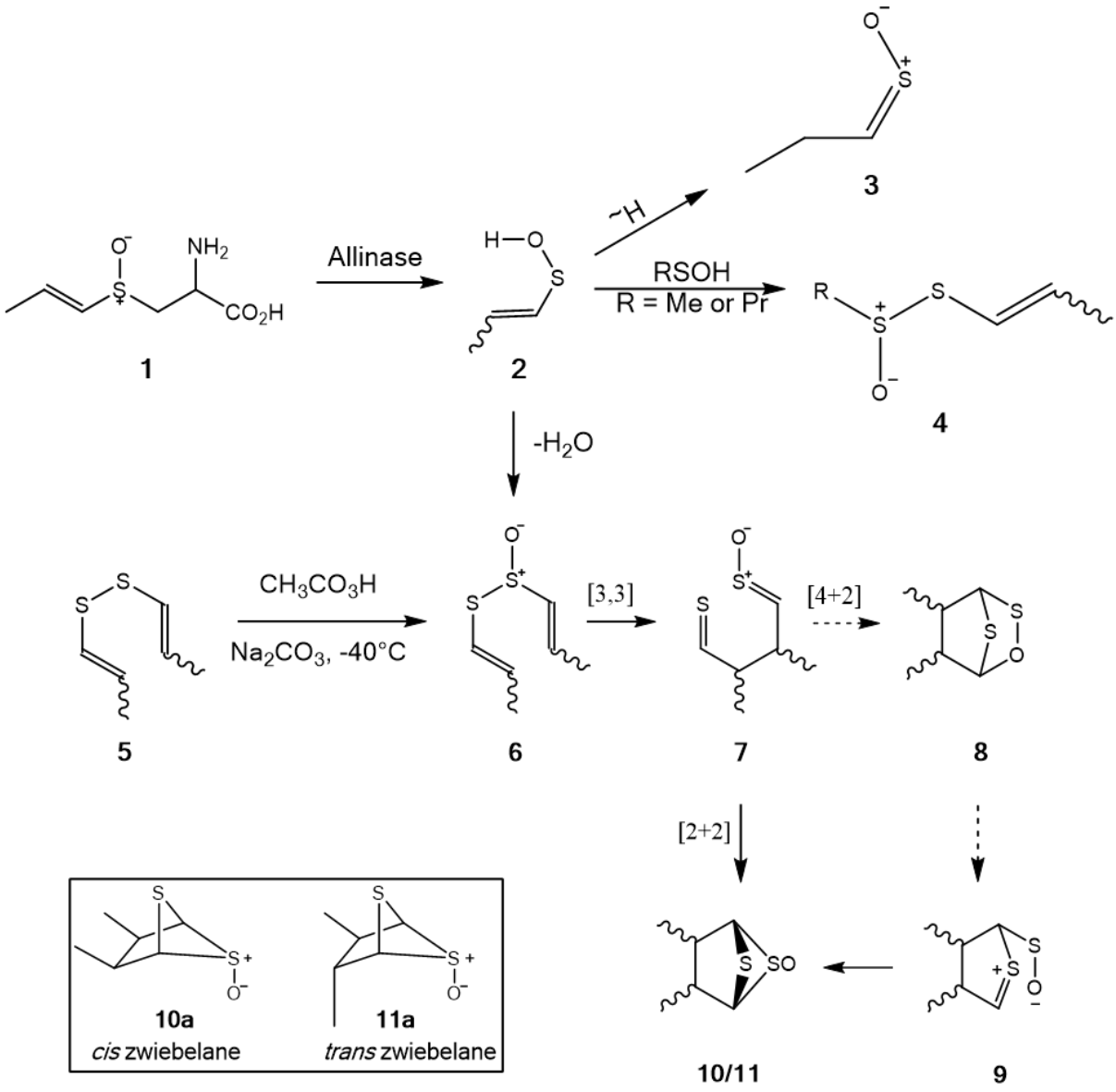

3.2.2 Methods

DFT calculations[16,17] were carried out using the Gaussian 16[18] program package. All optimization and frequency calculations for minima and transition state structures (TSSs) were performed at SMD(H_2O)-PW6B95-D3(BJ)/def2-TZVP(-f)[19,20] level of theory. NMR chemical shift calculations were carried out using M062X/6-31+G(d,p)[21] for geometries and GIAO[22–24] IEFPCM($CHCl_3$)-mPW1PW91/6-311+G(2d,p) for NMR predictions.[25–30] A linear scaling approach was used to convert computed isotropic shielding constants to chemical shifts. [31–33]

3.2.3 Results and Discussion

3.2.3.1 Confirmation of Structures

Bayer et al. isolated two isomeric compounds, which they named zwiebelane A (*cis*-zwiebelane) (**10**) and zwiebelane B (*trans*-zwiebelane) (**11**).[5] The four possible isomers of zwiebelane A (**10a-d**) and two possible isomers for zwiebelane B (**11a,b**) are shown in Figure 3.2.1. On the basis of the experimental spectroscopic data, structures of zwiebelane A and B were assigned as **10a** and **11a**. To assure that our mechanistic study was focused on the correct compounds we computed ^{1}H and ^{13}C NMR chemical shifts for all isomers using DFT.[16,17] As shown in Figure 3.2.1, the match between experimental and predicted chemical shifts is indeed best for **10a** and **11a**. In general, the largest deviations between experimental and predicted chemical shifts were observed for methine groups attached to sulfur atoms, as expected.[25–30] In addition, the methyl protons for the methyl group proximal to the oxygen are not predicted well for **11a**; this likely results from insufficient treatment of an intramolecular CH–O interaction between these groups.[34] Isomers **10a** and **11a** also are the lowest energy isomers for **10** and **11**: for **10**, the relative free energies with respect to **10a** are 10.2, 11.4 and 3.9 kcal mol^{-1} for **10b**, **10c** and **10d**, respectively; for **11**, the relative free energy of **11b** with respect to **11a** is 8.6 kcal mol^{-1}(M06-2X/6-311+G(d,p)//M06-2X/6-31+G(d,p)). In summary, we see no reason to doubt the original structural assignments.[35,36]

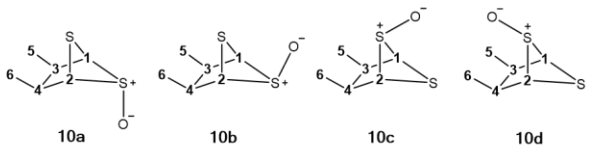

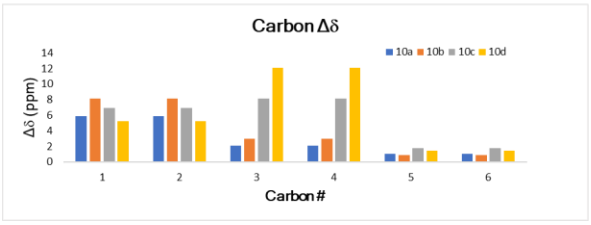

^{13}C MADs for 10a, 10b, 10c and 10d: 2.99, 4.03, 5.59 and 6.22 ppm

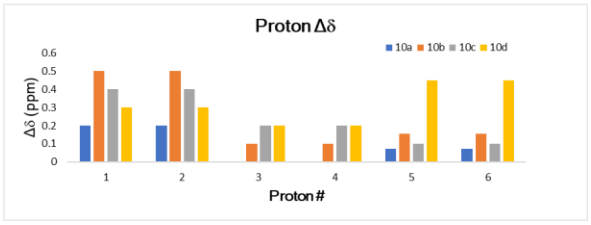

^{1}H MADs for 10a, 10b, 10c and 10d: 0.08, 0.21, 0.18 and 0.36 ppm

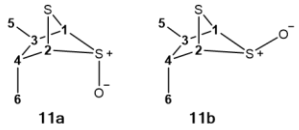

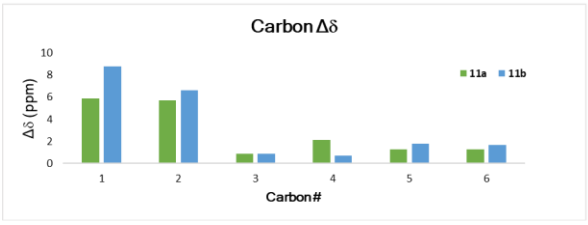

^{13}C MADs for 11a and 11b: 2.85 and 3.42 ppm

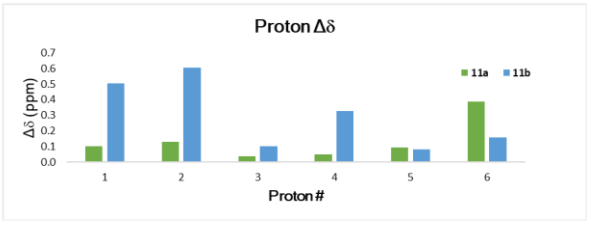

^{1}H MADs for 10a and 10b: 0.17 and 0.22 ppm

Figure 3.2.1. Absolute differences (in parts per million) between calculated (IEFPCM($CHCl_3$)-mPW1PW91/6-311+G(2d,p)//M062X/6-31+G(d,p)) and experimental ^{13}C and ^{1}H NMR shifts for **10a-d** (top) and **11a,b** (bottom).

3.2.3.2 Mechanistic Possibilities

Starting from structure **6**, the pathway toward the zwiebelanes first involves a [3,3] sigmatropic shift to form **7**. We calculated free energy barriers for each isomer of **6** that was previously suggested to form **7** (Figure 3.2.2a-d) and also proposed a different isomer (Figure 3.2.2e) that could further lead to **10a**. In Figure 3.2.2a and 3.2.2c, the thiosulfinate oxygens are pseudoequatorial, whereas in Figure 3.2.2b, 3.2.2d, and 3.2.2e, they are pseudoaxially oriented. For each isomer of **6**, the barrier for this rearrangement is predicted to be low, within 13-16 kcal mol^{-1}, and the forward reaction is predicted to be exergonic by nearly 2 kcal mol^{-1} (Figure 3.2.2). We decided to go with our proposed configuration of **6** (Figure 3.2.2e) and found a different pathway that could lead to **10a**.

a.

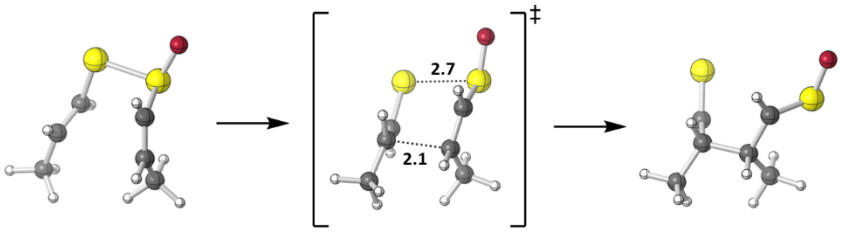

(*Z*,*E*)-6 0.0 | 6-TS 13.5 | 7 -1.8

b.

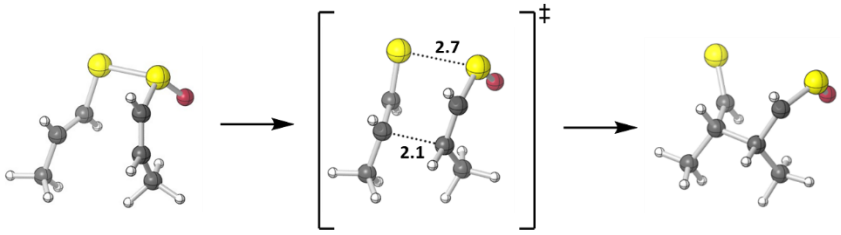

(*Z*,*E*)-6 0.0 | 6-TS 15.0 | 7 -2.1

c.

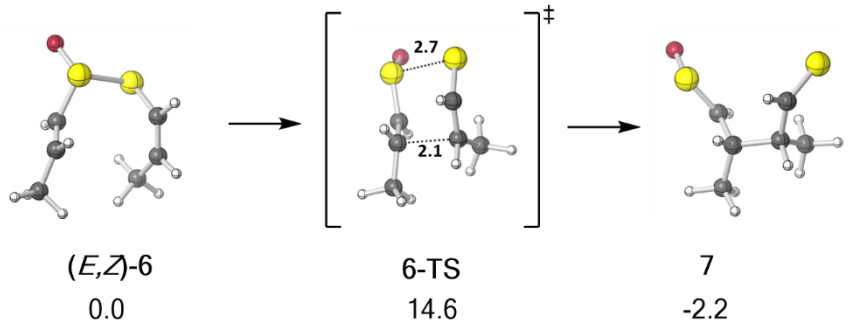

d.

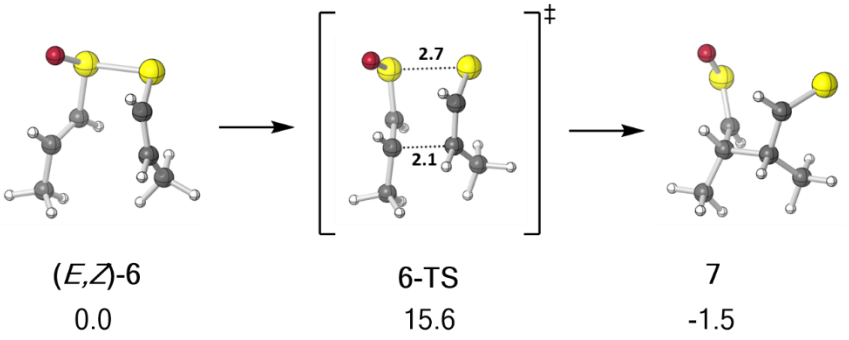

e.

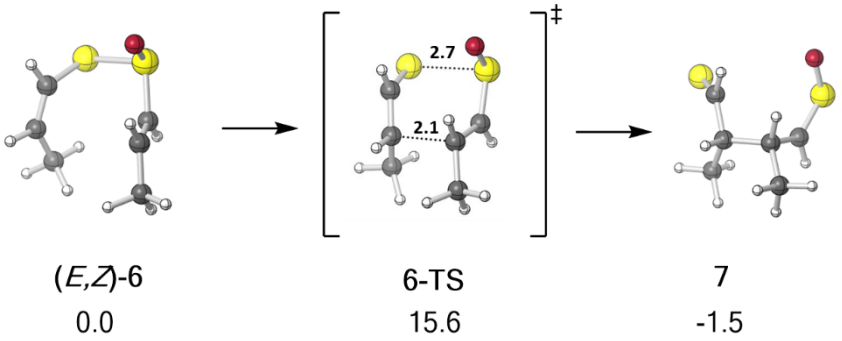

Figure 3.2.2. The relative Gibbs free energies (SMD(H_2O)-PW6B95-D3(BJ)/def2-TZVP(-f)) for the formation of **7** (in kcal mol^{-1}) with respect to each isomer of **6**.

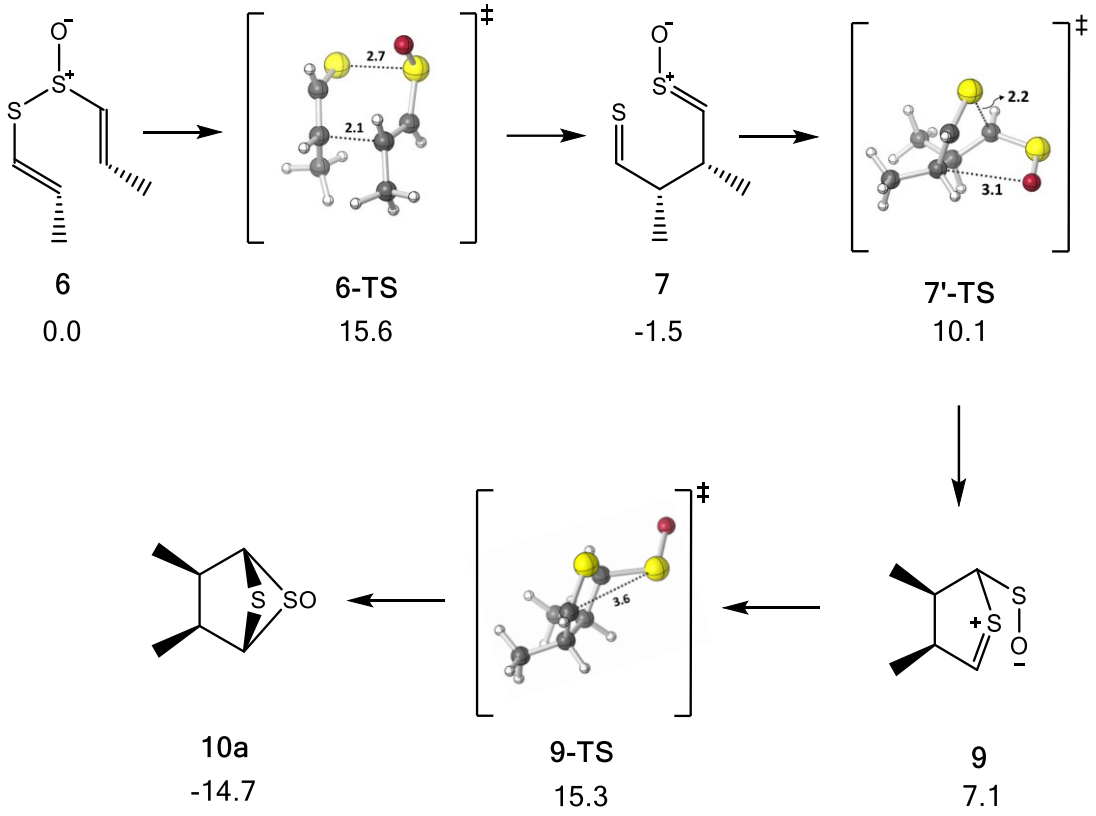

Figure 3.2.3. The minima and transition state structures for the synthesis of natural product **10a** starting from (*E,*Z)-**6.** The relative Gibbs free energies (SMD(H_2O)-PW6B95-D3(BJ)/def2-TZVP(-f)) for the structures (in kcal mol^{-1}) with respect to (*E,*Z)-**6**.

It was proposed previously that **7** can form **10a** via intramolecular (2+2) cycloaddition.[5,8] We couldn't find a TSS that directly connects **7** to **10a**. However, we found a TSS (**7-TS**) that connects **7** to **9** (Figure 3.2.3). We couldn't locate **7-TS** in gas phase which could be attributed to better stabilization of the zwitterion **9** in water. Structure **9** can then be converted to the natural product **10a** via **9-TS**. We are actively exploring possible pathways starting from different isomers of **6** towards **10a** along with the formation of bicyclic sultene **8**. Molecular dynamics studies are undergoing to test for the possibility of a post-transition state bifurcation occurrence in onions.

3.2.4 References

(1) Kubec, R.; Štefanová, I.; Moos, M.; Urajová, P.; Kuzma, M.; Zápal, J. Allithiolanes: Nine Groups of a Newly Discovered Family of Sulfur Compounds Responsible for the Bitter Off-Taste of Processed Onion. *J. Agric. Food Chem.* **2018**, *66*, 8783–8794.

(2) Carson, J. F. Chemistry and Biological Properties of Onions and Garlic. *Food Rev. Int.* **1987**, *3*, 71–103.

(3) Rose, P.; Whiteman, M.; Moore, P. K.; Yi, Z. Z. Bioactive S-Alk(En)yl Cysteine Sulfoxide Metabolites in the Genus Allium: The Chemistry of Potential Therapeutic Agents. *Nat. Prod. Rep.* **2005**, *22*, 351–368.

(4) Fritsch, R. M.; Keusgen, M. Occurrence and Taxonomic Significance of Cysteine Sulphoxides in the Genus Allium L. (Alliaceae). *Phytochemistry* **2006**, *67*, 1127–1135.

(5) Bayer, T.; Wagner, H.; Block, E.; Grisoni, S.; Zhao, S. H.; Neszmelyi, A. Zwiebelanes: Novel Biologically Active 2,3-Dimethyl-5,6-Dithiabicyclo[2.1.1]Hexane 5-Oxides from Onion. *J. Am. Chem. Soc.* **1989**, *111*, 3085–3086.

(6) Block, E. Fifty Years of Smelling Sulfur. *J. Sulphur Chem.* **2013**, *34,* 158–207.

(7) Borjihan, B.; Ogita, A.; Fujita, K. I.; Doe, M.; Tanaka, T. The Cyclic Organosulfur Compound Zwiebelane a from Onion (Allium Cepa) Functions as an Enhancer of Polymyxin B in Fungal Vacuole Disruption. *Planta Med.* **2010**, *76*, 1864–1866.

(8) Block, E.; Bayer, T.; Naganathan, S.; Zhao Shu-Hai. Allium Chemistry: Synthesis and Sigmatropic Rearrangements of Alk(En)yl 1-Propenyl Disulfide S-Oxides from Cut Onion and Garlic. *J. Am. Chem. Soc.* **1996**, *118*, 2799–2810.

(9) Block, E.; Thiruvazhi, M.; Toscano, P. J.; Bayer, T.; Grisoni, S.; Zhao, S.-H. Allium Chemistry: Structure, Synthesis, Natural Occurrence in Onion (Allium cepa), and Reactions of 2,3-Dimethyl-5,6-dithiabicyclo[2.1.1]hexane S-Oxides. *J. Am. Chem. Soc.* **1996**, *118*, 2790–2798.

(10) Tantillo, D. J. Walking in the Woods with Quantum Chemistry-Applications of Quantum Chemical Calculations in Natural Products Research. *Nat. Prod. Rep*. **2013**, *30*, 1079–1086.

(11) Tantillo, D. J. Interrogating Chemical Mechanisms in Natural Products Biosynthesis Using Quantum Chemical Calculations. *WIREs Comp. Molec. Sci.* **2020***, 10,* e1453.

(12) Sato, H.; Saito, K.; Yamazaki, M. Acceleration of Mechanistic Investigation of Plant Secondary Metabolism Based on Computational Chemistry. *Front. Plant Sci*. **2019**, *10*, 802.

(13) Imai, S.; Tsuge, N.; Tomotake, M.; Nagatome, Y.; Sawada, H.; Nagata, T.; Kumagai, H. An Onion Enzyme That Makes the Eyes Water. *Nature* **2002**, *419*, 685.

(14) July, R. Structure and Origin of the Onion Lachrymatory Factor. A Microwave Study. *J. Am. Chem. Soc.* **1979**, *1979*, 2200–2201.

(15) Randle, W. M. Onion Flavor Chemistry and Factors Influencing Flavor Intensity. In *Spices - Flavour Chemistry and Antioxidant Properties;* Risch, S. J.; C.-T. Ho, Eds.; ACS Symposium series*,* 1997*;* pp 41-52.

(16) Parr, R. G.; Yang, W. Density-Functional Theory of the Electronic Structure of Molecules. *Annu. Rev. Phys. Chem.* **1995**, *46*, 701–728.

(17) Eschrig, H. The Fundamentals of Density Functional Theory. *Inst. Solid State Mater. Res. Dresden Univ. Technol. Dresden* **2003**, 204.

(18) Frisch, M. J.; Trucks, G. W.; Schlegel, H. B.; Scuseria, G. E.; Robb, M. A.; Cheeseman, J. R.; Scalmani, G.; Barone, V.; Petersson, G. A.; Nakatsuji, H., et al. *Gaussian 16,* Revision A.03.; Gaussian, Inc.: Wallingford, CT, 2016.

(19) Weigend, F.; Ahlrichs, R. Balanced Basis Sets of Split Valence, Triple Zeta Valence and Quadruple Zeta Valence Quality for H to Rn: Design and Assessment of Accuracy. *Phys. Chem. Chem. Phys.* **2005**, *7*, 3297–3305.

(20) Goerigk, L.; Hansen, A.; Bauer, C.; Ehrlich, S.; Najibi, A.; Grimme, S. A Look at the Density Functional Theory Zoo with the Advanced GMTKN55 Database for General Main Group

Thermochemistry, Kinetics and Noncovalent Interactions. *Phys. Chem. Chem. Phys.* **2017**, *19*, 32184–32215.
(21) Zhao, Y.; Truhlar, D. G. M062X and M06. *Theor. Chem. Acc.* **2008**, *120*, 215–241.
(22) Bagno, A.; Saielli, G. Addressing the Stereochemistry of Complex Organic Molecules by Density Functional Theory-NMR. *Wiley Interdiscip. Rev. Comput. Mol. Sci.* **2015**, *5*, 228–240.
(23) de Albuquerque, A. C. F.; Ribeiro, D. J.; de Amorim, M. B. Structural Determination of Complex Natural Products by Quantum Mechanical Calculations of 13C NMR Chemical Shifts: Development of a Parameterized Protocol for Terpenes. *J. Mol. Model.* **2016**, *22*, 1–7.
(24) Cheeseman, J. R.; Trucks, G. W.; Keith, T. A.; Frisch, M. J. Shielding Tensors. *J. Chem. Phys.* **1996**, *104*, 5497–5509.
(25) Jain, R.; Bally, T.; Rablen, P. R. Calculating Accurate Proton Chemical Shifts of Organic Molecules with Density Functional Methods and Modest Basis Sets. *J. Org. Chem.* **2009**, *74*, 4017–4023.
(26) Bagno, A.; Saielli, G. Computational NMR Spectroscopy: Reversing the Information Flow. *Theor. Chem. Acc.* **2007**, *117*, 603–619.
(27) Dybiec, K.; Gryff-Keller, A. Remarks on GIAO-DFT Predictions of ^{13} C Chemical Shifts. *Magn. Reson. Chem.* **2009**, *47*, 63–66.
(28) Helgaker, T.; Jaszuński, M.; Ruud, K. Ab Initio Methods for the Calculation of NMR Shielding and Indirect Spin−Spin Coupling Constants. *Chem. Rev.* **1999**, *99,* 293-352.
(29) Hoffmann, F.; Li, D.-W.; Sebastiani, D.; Brüschweiler, R. Improved Quantum Chemical NMR Chemical Shift Prediction of Metabolites in Aqueous Solution toward the Validation of Unknowns. *J. Phys. Chem. A* **2017**, *121*, 3071–3078.
(30) Lodewyk, M. W.; Siebert, M. R.; Tantillo, D. J. Computational Prediction of ^{1} H and ^{13} C Chemical Shifts: A Useful Tool for Natural Product, Mechanistic, and Synthetic Organic Chemistry. *Chem. Rev.* **2012**, *112*, 1839–1862.
(31) Maeda, S.; Harabuchi, Y.; Ono, Y.; Taketsugu, T.; Morokuma, K. Intrinsic Reaction Coordinate: Calculation, Bifurcation, and Automated Search. *Int. J. Quantum Chem.* **2015**, *115*, 258–269.
(32) Fukui, K. The Path of Chemical Reactions - the IRC Approach. *Acc. Chem. Res.* **1981**, *14*, 363–368.
(33) Gonzalez, C.; Schlegel, H. B. Reaction Path Following in Mass-Weighted Internal Coordinates. *J. Phys. Chem.* **1990**, *94*, 5523–5527.
(34) Nguyen, Q. N. N.; Schwochert, J.; Tantillo, D. J.; Lokey, R. S. Using 1H and 13C NMR Chemical Shifts to Determine Cyclic Peptide Conformations: A Combined Molecular Dynamics and Quantum Mechanics Approach. *Phys. Chem. Chem. Phys.* **2018**, *20*, 14003–14012.
(35) Weinreb, S. M. Lepadiformine: A Case Study of the Value of Total Synthesis in Natural Product Structure Elucidation. *Acc. Chem. Res.* **2003**, *36*, 59–65.
(36) Nicolaou, K. C.; Snyder, S. A. Chasing Molecules That Were Never There: Misassigned Natural Products and the Role of Chemical Synthesis in Modern Structure Elucidation. *Angew. Chemie Int. Ed.* **2005**, *44*, 2050–2050.

Chapter 4. Catalyst-Controlled Regiodivergence in Rearrangements of Indole-Based Onium Ylides

This chapter is adapted with slight modifications with permission from Nair, V. N.; Kojasoy, V.; Laconsay, C. J.; Kong, W.; Tantillo, D. J.; Tambar, U. K. Catalyst-Controlled Regiodivergence in Rearrangements of Indole-Based Onium Ylides. *J. Am. Chem. Soc.* **2021**, *143*, 9016-9025. Copyright 2021 American Chemical Society. Vaishnavi N. Nair (of Prof. Uttam K. Tambar's group) completed the experimental portions of this chapter. Croix J. Laconsay and Wang Yeuk Kong contributed to the DFT calculations.

4.1 Abstract

We have developed catalyst-controlled regiodivergent rearrangements of onium-ylides derived from indole substrates. Oxonium ylides formed *in situ* from substituted indoles selectively undergo [2,3]- and [1,2]-rearrangements in the presence of a rhodium and a copper catalyst, respectively. The combined experimental and density functional theory (DFT) computational studies indicate divergent mechanistic pathways involving a metal-free ylide in the rhodium catalyzed reaction favoring [2,3]-rearrangement, and a metal-coordinated ion-pair in the copper catalyzed [1,2]-rearrangement that recombines in the solvent-cage. The application of our methodology was demonstrated in the first total synthesis of the indole alkaloid (±)-sorazolon B, which enabled the stereochemical reassignment of the natural product. Further functional group transformations of the rearrangement products to generate valuable synthetic intermediates were also demonstrated.

4.2 Introduction

Molecular rearrangements are arguably some of the most effective reactions for the generation of new carbon−carbon bonds in the synthesis of complex molecules.[1] In recent years, advances in catalytic onium ylide rearrangements have paved the way for catalyst control of rearrangements that are traditionally unselective.[2,3] In this context, catalytic generation of onium ylides from diazocarbonyl compounds has served as a versatile platform for selective rearrangements (Scheme 4.1A). Despite many reports of catalytic onium ylide rearrangements of aliphatic systems,[4,5] only a few examples of analogous aromatic

rearrangements are known which are limited to sulfonium (X = SR) and ammonium ($X = NR_2$) ylides.[6] The challenge of developing this class of rearrangements is partially due to the energetic penalty associated with disruption of aromaticity in the sigmatropic [2,3]-rearrangement (Scheme 4.1A).[7] A pioneering study on catalytic thia-Sommelet-Hauser rearrangement was reported by Wang and co-workers in 2008.[6c] In recent years, examples of controlled [1,2]- and [2,3]-rearrangements of ylides in aromatic systems have appeared in the literature.[8] Pan and co-workers reported rearrangements of sulfonium ylides where the selectivity for [1,2]- vs [2,3]-rearrangement is controlled by the solvent and substrate.[8a] Another report from Koenigs and co-workers shows a solvent controlled approach in rearrangements of sulfonium ylides formed from donor/acceptor carbenes.[8b] Alternatively, catalytic ylide-formation and aromatic [2,3]-rearrangements of oxonium systems (X = OR) are not known, presumably because of side reactions through nonylide pathways such as C−H insertion and cyclopropanation that compete with facile ylide formation.[9] Also, the examples for the [1,2]-rearrangement of oxonium ylides in the literature are generally limited to cyclic ylides.[4b–k] Catalytic methods for the selective formation of either [1,2]- or [2,3]-rearrangement products of aromatic systems from the same starting materials would provide a valuable new strategy for the synthesis of complex molecules.

Herein, we report the first catalyst-controlled regiodivergent aromatic rearrangements of indole-based oxonium ylides (Scheme 4.1B). With the proper choice of catalyst system, we can selectively generate the [1,2]- or [2,3]-rearrangement product. As our initial target for the rearrangements, we chose the indole-scaffold because of its prevalence in many natural products and medicinally valuable compounds.[10] In addition to exploring the scope of this reaction, we also performed DFT calculations to examine mechanisms and the origins of catalyst-controlled regiodivergence. Finally, to showcase the utility of our method, we demonstrated the conversion of rearrangement products into the indole alkaloid sorazolon B and several valuable building blocks for drug discovery.

Scheme 4.1. Catalyst Control of Regioselectivity in Onium Ylide Rearrangements

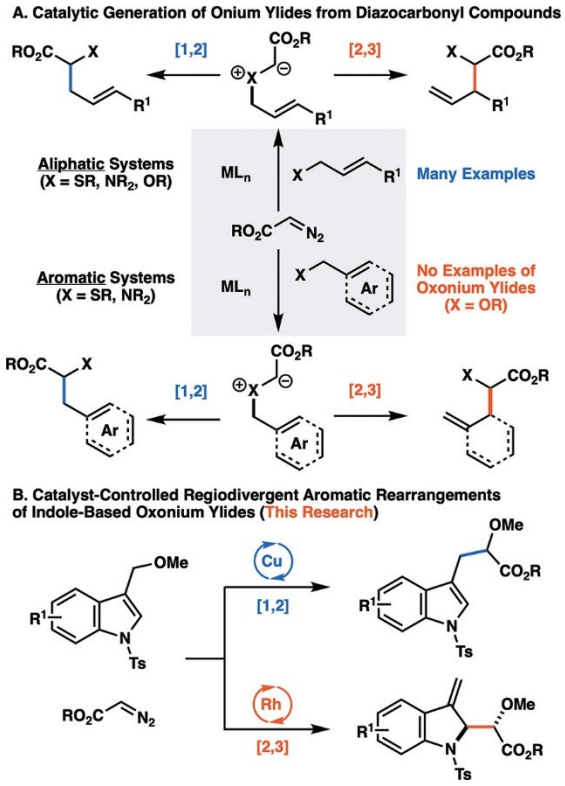

4.3 Results and Discussion

4.3.1 Development of Regiodivergent Rearrangements

Our initial investigations began with the screening of various catalysts that are generally applied in carbene chemistry,[11] using 3-(methoxymethyl)-1-tosyl-1H-indole (**1a**) and benzyl diazoester (**2a**) as substrates (Table 4.1). While we did not observe any reactivity in the presence of palladium, silver, or gold catalysts (entries 1−3), CuOTf·benzene (5 mol %) afforded a mixture of [1,2]- and [2,3]-rearrangement products **3a** and **4a** (82:18 rr), respectively, in low yield (entry 4). Moreover, we were pleased to note that indoline **4a** bearing an exomethylene moiety (presumably from the [2,3]-rearrangement) was formed with excellent diastereoselectivity (>20:1 dr). Moving forward with this initial result that gave **3a** as the major product, we began optimizing the [1,2]-rearrangement of the oxonium ylides by screening additional copper sources.

Other copper catalysts such as CuCl, $CuCl_2$, and CuOAc/$NaBAr_F$ gave similar or slightly improved yields, but relatively lower regioselectivities (entry 5−7). We were delighted to see an improved yield (38%) as well as regioselectivity (86:14 rr) with $[Cu(MeCN)_4]PF_6$ as catalyst (entry 8). The use of $Cu(hfacac)_2$ to perform the rearrangement further enhanced the yield (52%) and regioselectivity (92:8 rr) (entry 9). An examination of the conversion of the starting materials under these conditions revealed that the yield was limited by the incomplete consumption of indole **1a**, whereas the diazoester **2a** was completely consumed to give the desired products along with minor amounts of dibenzyl fumarate and dibenzyl maleate as the side products resulting from homodimerization. Increasing the amount of benzyl diazoester 2a to 2.4 equiv resulted in >95% conversion of **1a** to provide the [1,2]-rearrangement product **3a** in 78% yield and >95:5 rr (entry 10).

Alternatively, when $Rh_2(OAc)_4$ (2 mol %) was used as the catalyst, we observed a switch in the regioselectivity that gave the [2,3]-rearrangement product **4a** as the major product (>95:5 rr) in 42% yield and >20:1 dr (entry 11). The screening of several other dirhodium carboxylate catalysts commonly used in metal-carbene transformations, such as $Rh_2(cap)_4$, $Rh_2(TFA)_4$, $Rh_2(TPA)_4$, and $Rh_2(oct)_4$,[12] failed to improve the yield for the reaction (entries 12−15). Similar to the copper-catalyzed [1,2]-rearrangement, an incomplete consumption of indole 1a (55%) was identified as the reason for the moderate yields. However, increasing the amount of diazoester **2a** to 2.4 equiv diminished the yield of the [2,3]-rearrangement product **4a** to 26% (entry 16). We speculate that the reason for the lower yield with excess diazoester might be the propensity of the exomethylene group in **4a** to undergo cyclopropanation with excess highly reactive rhodium-carbene (see SI for details). We also examined other indole substrates besides methyl ether **1a** for optimization studies. While ethyl ether underwent the [2,3]-rearrangement, other alkyl and arylethers such as isopropyl and phenyl ethers did not give any conversion under the [2,3]-rearrangement conditions (see SI for details). Other N-protecting groups such as Me, Boc, and Ac were also screened during optimization for [2,3]-rearrangement, but most of these substrates did not show significant product formation (see SI for details). Further screening of different solvents also did not provide improvement in the yield (entries 17-

19). As a result, the conditions with $Rh_2(OAc)_4$ (2 mol %) in CH_2Cl_2 at 23 °C were identified as optimal for the catalytic ylide-formation/aromatic [2,3]-rearrangement (entry 11).

Table 4.1. Optimization of [1,2]- and [2,3]-Rearrangements[a]

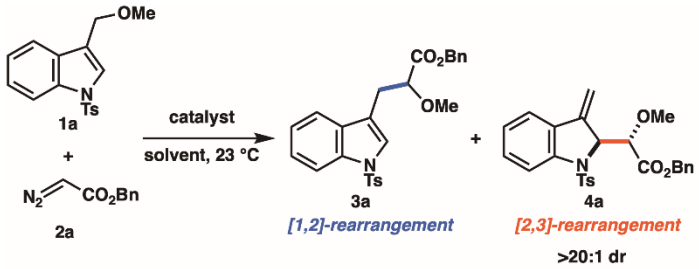

Entry	Catalyst	Solvent	Conversion[b] (%)	Yield[c] (%)	3a:4a
1	$PdCl_2$	CH_2Cl_2	<5	<5	-
2	AgOTf	CH_2Cl_2	<5	<5	-
3	Ph_3PAuCl	CH_2Cl_2	<5	<5	-
4	Cu(OTf)· benzene	CH_2Cl_2	5	5	82:18
5	CuCl	CH_2Cl_2	5	5	71:29
6	$CuCl_2$	CH_2Cl_2	8	7	75:25
7	CuOAc/ $NaBAr_F$	CH_2Cl_2	26	18	76:24
8	$[Cu(MeCN)_4]PF_6$	CH_2Cl_2	42	38[d]	86:14
9	$Cu(hfacac)_2$	CH_2Cl_2	67	52[d]	92:8
10[e]	$Cu(hfacac)_2$	CH_2Cl_2	>95	78[d]	>95:5
11	$Rh_2(OAc)_4$	CH_2Cl_2	55	42[d]	<5:95
12	$Rh_2(cap)_4$	CH_2Cl_2	<5	<5	-
13	$Rh_2(TFA)_4$	CH_2Cl_2	30	<5	-
14	$Rh_2(TPA)_4$	CH_2Cl_2	56	23	32:68
15	$Rh_2(oct)_4$	CH_2Cl_2	44	33	10:90
16[e]	$Rh_2(OAc)_4$	CH_2Cl_2	92	26	<5:95
17	$Rh_2(OAc)_4$	DCE	41	36	<5:95
18	$Rh_2(OAc)_4$	$CHCl_3$	51	33	<5:95
19	$Rh_2(OAc)_4$	toluene	20	16	<5:95

[a]Reaction conditions: indole **1a** (0.16 mmol), benzyl diazoester **2a** (1.2 equiv, added using syringe pump as 0.2 M solution in solvent at a rate of 2 mL/h), copper catalyst (5 mol %) or rhodium catalyst (2 mol %). [b]Conversion of **1a**. [c]NMR yield using 1,3,5-trimethoxybenzene as internal standard. [d]Isolated yield. [e]2.4 equiv of **2a** was used.

4.3.2 Substrate Scope of Regiodivergent Rearrangements

With the optimized reaction conditions for both the copper-catalyzed ylide-formation/[1,2]-rearrangement and rhodium-catalyzed ylide-formation/[2,3]-rearrangement in hand (entries 10 and 11, Table 4.1), we next explored reaction scope (Table 4.2).

Table 4.2. Products Generated by Regiodivergent [1,2]- and [2,3]-Rearrangements

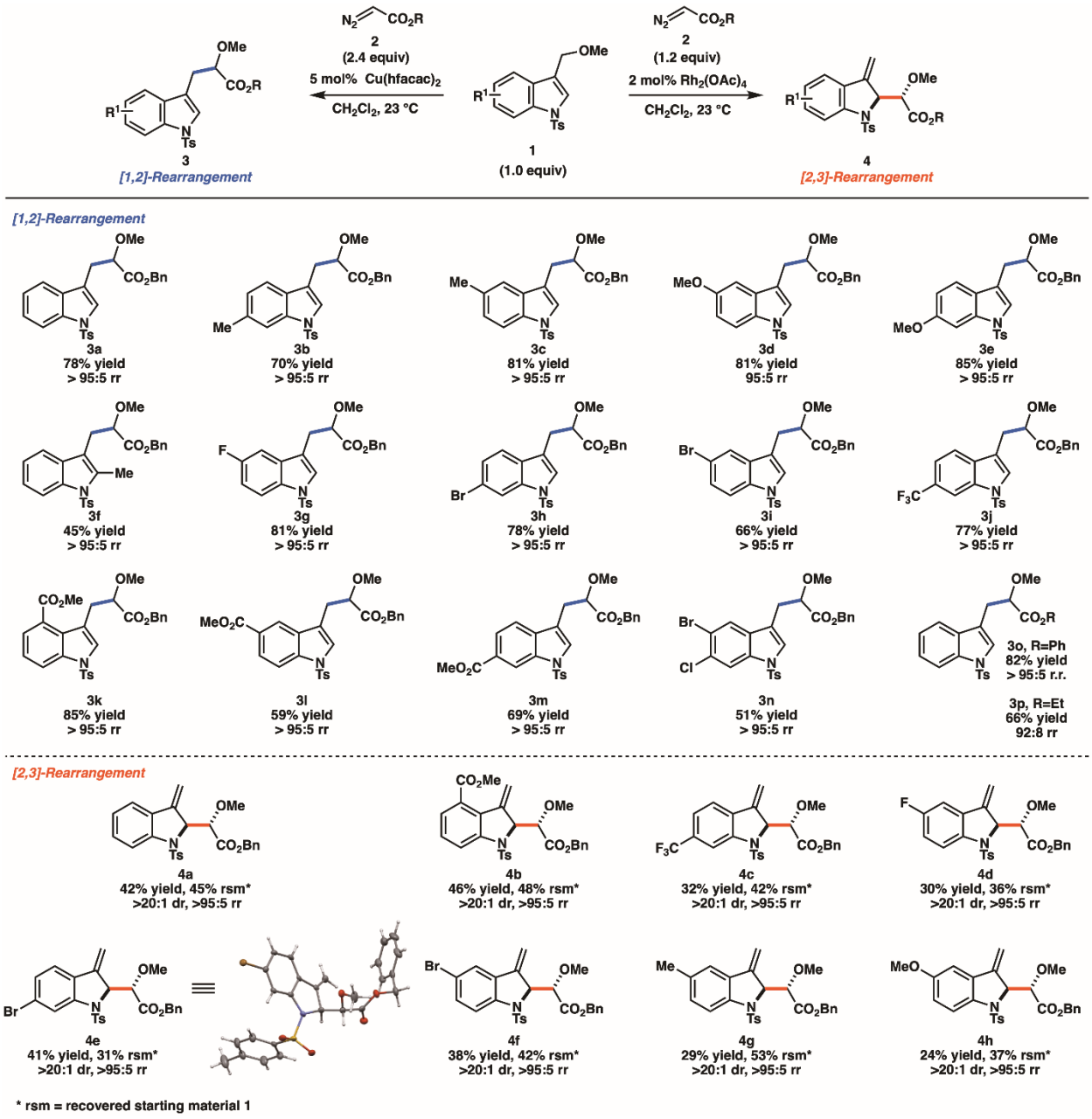

Indole substrates with a broad range of substituents at various positions on the heteroaromatic ring (**3a−3p**) worked efficiently under the [1,2]-rearrangement conditions. Electron rich 5-and 6-substituted indole substrates provided high yields and excellent regioselectivities (**3b−3e**). Substitution at the 2-position generated the desired [1,2]-rearrangement product **3f**, albeit in slightly lower yield, but nonetheless gave excellent regioselectivity (>95:5 rr). Several electron-withdrawing substituents on the indole ring, including fluoro, bromo, trifluoromethyl, and ester groups (**3g−3m**), provided good yields and high regioselectivities. The reaction also progressed smoothly to generate dihalogenated product **3n** in 51% yield and >95:5 rr. In addition, other alkyl and aryl diazoesters were shown to be competent in generating [1,2]-rearrangement products in moderate to good yields (**3o and 3p**).

Next, we explored the scope of the rhodium-catalyzed ylide formation/[2,3]-rearrangement to provide various substituted indolines (**4**) that would be difficult to access in high selectivity by conventional methods.[13] Several electron-deficient indole rings with different substitution patterns underwent selective aromatic [2,3]-rearrangement to generate indolines (**4b−4f**) in moderate yields and with excellent regioselectivities. Electron-donating substituents on the indole ring led to comparatively lower isolated yields of the products (**4g** and **4h**); however, the [2,3]-rearrangement proceeded with excellent regioselectivity.[14] The rearrangement products were generally stable to re-aromatization, presumably because of the electron-withdrawing tosyl protecting group similar to other known indolines.[13b,c] Notably, the [2,3]-rearrangement of all the substrates exhibited high diastereoselectivity (>20:1 dr). The relative stereochemistry of the major anti-diastereomer of product **4e** was confirmed by X-ray crystallography, and the relative stereochemistry of the major diastereomer of all other 2-substituted indolines was assigned by analogy.

4.3.3 Mechanistic Studies

To gain insight into the divergent mechanisms of the catalyst controlled ylide-formation/rearrangement reactions, a series of computational studies were performed using density functional theory at the PWPB95-

D3(BJ)/def2-QZVPP//IEFPCM(CH_2Cl_2)-B3LYP/6-31G(d), SDD level (see SI for details).[15] The robustness of our chosen level of theory was evaluated through a series of tests with other functionals and basis sets (see SI for details); while there is some variation in predicted relative energies, these variations do not affect our mechanistic conclusions. 3-(Methoxymethyl)-1-tosyl-1H-indole 1a was selected as the model substrate.

For the rhodium-catalyzed ylide-formation/[2,3]-rearrangement, we first examined the structure of the metal-bound oxonium ylide (Figure 4.1). Formation of the carbon-bound ylide **5** is predicted to be exergonic by 9.2 kcal mol^{-1}, whereas formation of the oxygen-bound ylide **6** is endergonic by 7.0 kcal mol^{-1}.

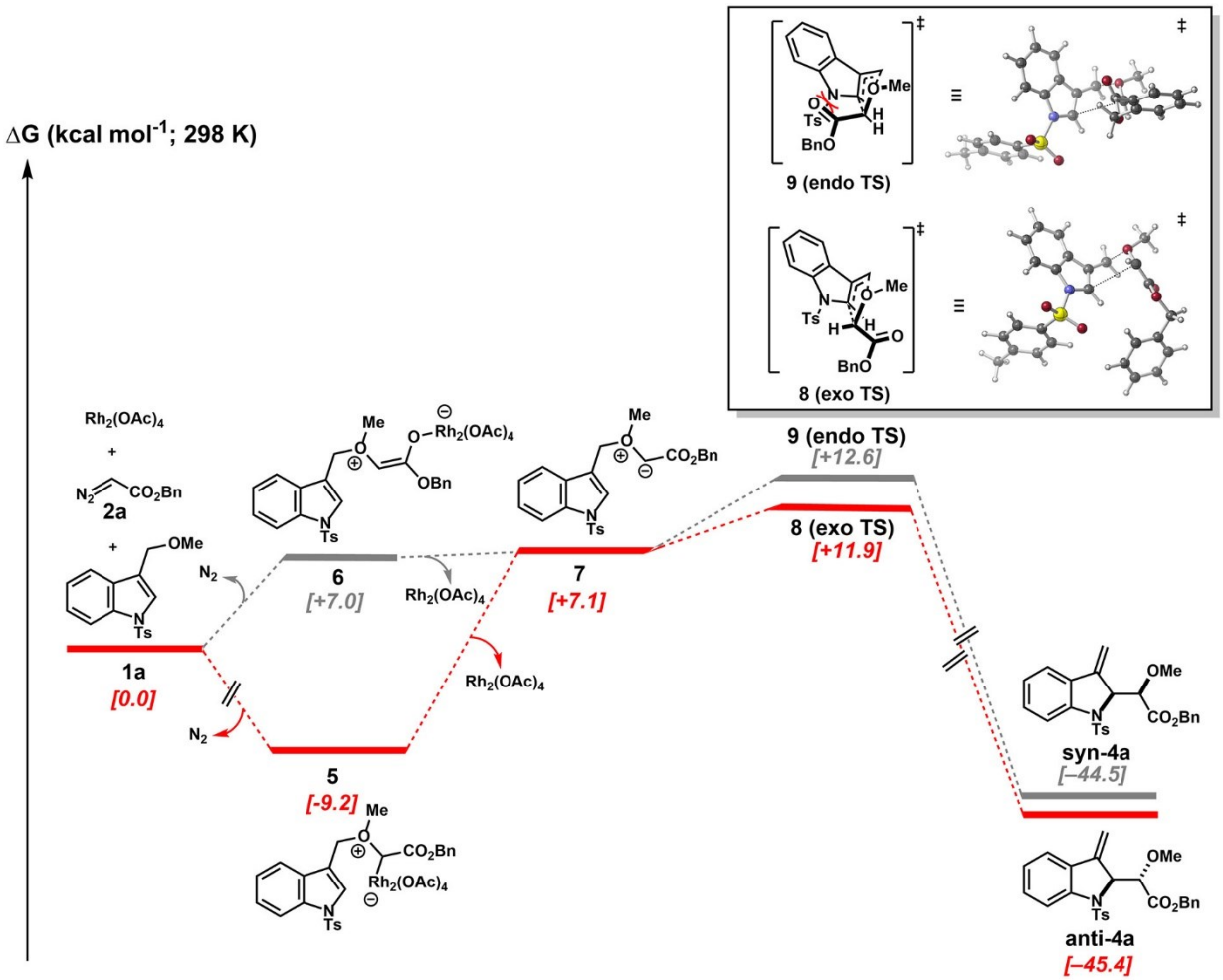

Figure 4.1. Computed (PWPB95-D3(BJ)/def2-QZVPP//IEFPCM(CH_2Cl_2)-B3LYP/6-31G(d), SDD) relative free energies (kcal mol^{-1}, *italics*) for minima and TSSs involved in the Rh-promoted reaction of **1a** and **2a**.

Our proposed pathway for a concerted [2,3]-rearrangement process is summarized in Figure 4.1. Dissociation of $Rh_2(OAc)_4$ prior to rearrangement generates free oxonium ylide **7**. Early dissociation of rhodium(II) complexes from ylides has been reported for other diazocarbonyl-mediated reactions.[4a,16] The most probable pathway to the product involves a metal-free [2,3]-rearrangement of oxonium ylide **7**, which leads to the observed product **4a** with the experimentally observed relative stereochemistry.[17] As expected, we were not able to find a transition state structure for the symmetry-forbidden metal-free [1,2]-rearrangement of oxonium ylide **7**.[18] The *relative* stereochemistry of the major diastereomer of products arising from the [2,3]-rearrangement of indole-based onium ylides such as **7** is consistent with a preference for an *exo* transition state structure (**8**).[4d] Relative free energies calculated for the *exo* and *endo* transition states predicted a lower energy barrier for *exo* transition state **8** leading to the observed diastereomer *anti*-**4a**.

For the copper-catalyzed ylide-formation/[1,2]-rearrangement, we propose a mechanism that involves a stepwise process (Figure 4.2A).[4e,19] The preferential formation of the [1,2]-rearrangement product **3a** over the [2,3]-rearrangement product **4a** is an argument against pathways involving the early dissociation of copper from the initially generated metal-coordinated ylide **11**, since metal-free [1,2] rearrangement is predicted to have an extremely high barrier compared to that of the [2,3]-rearrangement (see SI for details). On the basis of our computational results, we favor an ion-pair fragmentation/recombination pathway for the copper-catalyzed reactions.[20] Other possible pathways were explored but were not consistent with our experimental results (see SI for details). For example, formation of simple radical-pairs cannot be ruled out on the basis of our computational results, but our experimental data argues against it. Specifically, cyclopropane containing substrate **1q** reacted with diazoester **2a** to yield the [1,2]-rearrangement product **3q** with the radical probe intact (Figure 4.2B).[21,22]

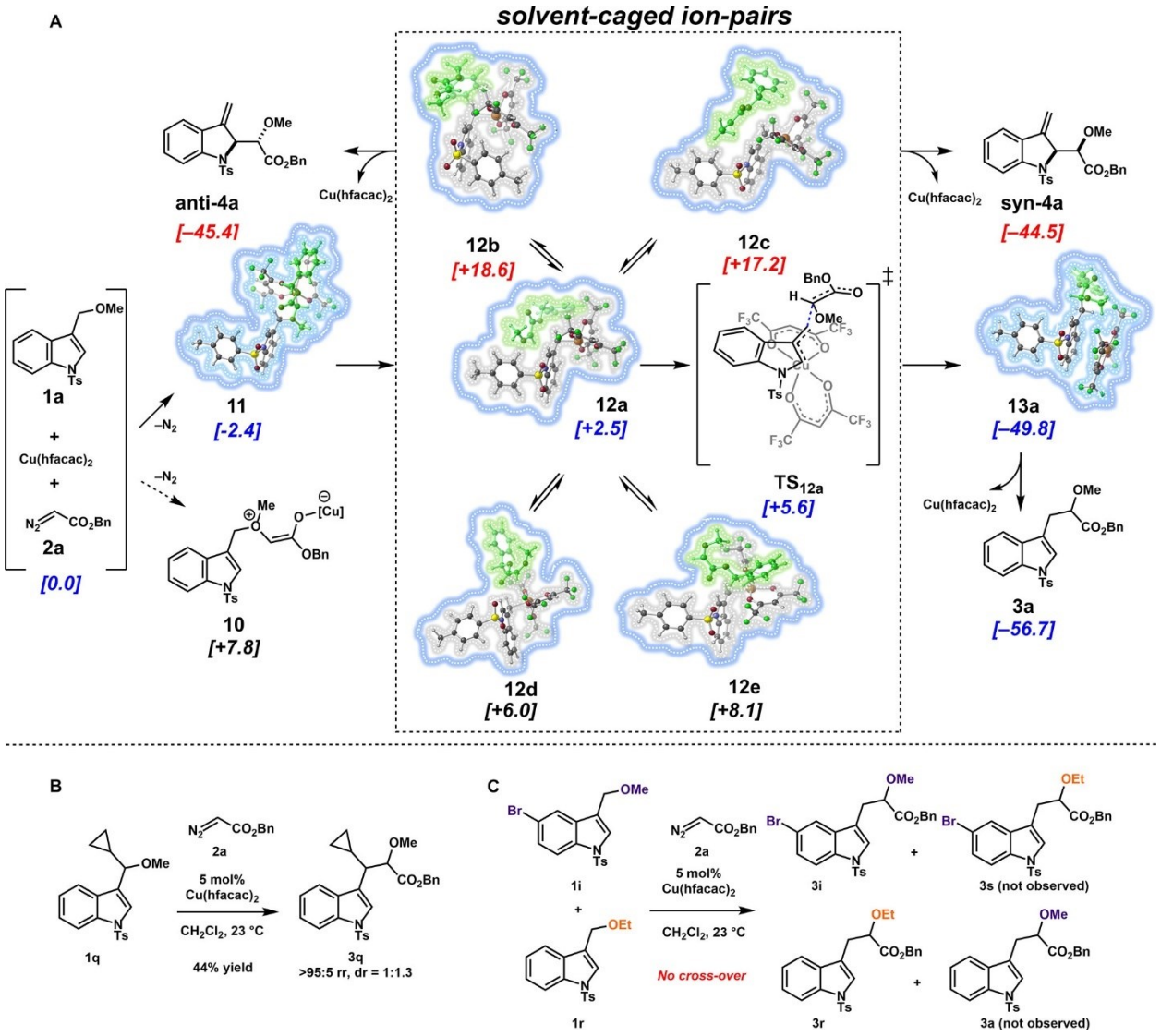

Figure 4.2. (A) Computed (PWPB95-D3(BJ)/def2-QZVPP//IEFPCM(CH_2Cl_2)-B3LYP/6-31G(d),SDD) relative free energies (kcal mol^{-1}, *italics*) for minima and TSSs involved in the Cu-promoted reaction of **1a** and **2a**. A selection of ion-pairs **12a-12e** were generated by scanning the bonds that form en route to the products. The energies for ion-pairs **12a-12e** are based on optimized complexes. Geometries of ion-pairs **12a-12e**, their preceding zwitterion **11**, and the recombination product **13a** shown in ball-and-stick images are included to facilitate comparison of overall shapes. For clarity in visual comparison, the enolate part of the ion-pair is highlighted in green and the indolyl part (highlighted in gray) is positioned the same way for each structure above. The solvent cage (not modeled explicitly) is depicted in blue with dotted lines. (B)

Reaction conditions for radical probe experiment: indole **1q** (0.16 mmol), benzyl diazoester **2a** (1.2 equiv, added using syringe pump as 0.2 M solution in CH_2Cl_2 at a rate of 2 mL/h), $Cu(hfacac)_2$ (5 mol %), CH_2Cl_2, 23 °C. (C) Reaction conditions for crossover experiment: indole **1i** (0.08 mmol, 0.5 equiv), indole **1r** (0.08 mmol, 0.5 equiv) benzyl diazoester **2a** (1.2 equiv, added using syringe pump as 0.2 M solution in CH_2Cl_2 at a rate of 2 mL/h), $Cu(hfacac)_2$ (5 mol %), CH_2Cl_2, 23 °C.

To gain insight into the key carbon−carbon bond formation event in the copper-catalyzed reaction, we considered ion-pair complexes (**12a, 12b, 12c, 12d,** and **12e**) that could lead to the [1,2]-rearrangement product **3a** or the [2,3]-rearrangement product diastereomers *syn*-**4a** and *anti*-**4a** with minimal reorganization (Figure 4.2A).[23] In principle, these ion-pairs would be in equilibrium with each other and could recombine to form copper-bound recombination products (e.g., **13a**, Figure 4.2A).[24] However, recombination in a solvent cage is expected to be faster than equilibration between ion-pairs.[20g,25] Although a solvent cage was not explicitly modeled in our calculations, the formation of ion-pairs in a solvent cage is consistent with experimentally determined results. When substrates **1i** and **1r** were simultaneously subjected to the [1,2]-rearrangement conditions, we did not detect crossover products **3s** and **3a** (Figure 4.2C).

We were able to find a transition state structure (TS_{12a}) converting the ion-pair **12a** to **13a**, the $Cu(hfacac)_2$-bound experimentally observed product, with a 3.1 kcal mol^{-1} barrier. Subsequent dissociation of Cu catalyst yields **3a**. If **12a** was formed preferentially on the dissociation of the copper-coordinated oxonium ylide **11**, we propose that this ion-pair could rapidly recombine to the experimentally observed product (**12a** → **3a**) before equilibration with other ionpairs. Comparisons of the various ion-pairs and metal-ylide intermediate **11** do indeed reveal greater conformational similarity between **11** and **12a** than either **12b, 12c, 12d,** or **12e** (Figure 4.2A; see SI for details). We also investigated the proposed stepwise ion-pair mechanism with other copper catalysts ($Cu(acac)_2$, $CuCl_2$, $Cu(hfacac)^+$, and $Cu(acac)^+$), and all qualitatively lead to similar results (see SI for details).

In summary, on the basis of our combined experimental and computational data, we favor a mechanism for the rhodium-promoted reaction where early catalyst dissociation occurs at the ylide stage, and products are formed via a metal-free [2,3]-sigmatropic rearrangement. For the copper-promoted reaction, we favor a mechanism where a copper-coordinated ion-pair is formed and rapidly recombines in a solvent cage to form the observed [1,2]-rearrangement product.

4.3.4 Synthetic Applications of Regiodivergent Rearrangements

The products generated through the [2,3]-rearrangement proved to be versatile substrates to access building blocks that are potentially useful for the synthesis of complex molecules (Scheme 4.2). For example, rearrangement product **4a** can undergo ozonolysis to yield indoxyl product **14**. In the presence of acid, the rearrangement product **4a** is rearomatized to furnish 2,3-disubstituted indole **15**. In the presence of an electrophilic source of bromine, it is selectively converted to 3-bromomethyl indole **16**.

To demonstrate the synthetic utility of the [1,2]-rearrangement products, we incorporated this transformation into the first total synthesis of the indole alkaloid sorazolon B, which enabled a stereochemical reassignment of the natural product's structure that was reported in the original isolation paper (Scheme 4.3).[26] To commence the total synthesis, 3-(methoxymethyl)-1-tosyl-1H-indole (**1a**) was coupled with diazoester **2a** under the [1,2]-rearrangement conditions to furnish benzylester **3a** in 82% yield and >95:5 rr. The efficiency of the reaction was maintained on a gram scale. A two-step procedure converted benzylester **3a** to the Weinreb amide **17**. Subsequent removal of the N-tosyl group provided N−H indole **18** in 93% yield. To access the relative configuration for the proposed structure of sorazolon B (**21**), we treated the Weinreb amide **18** first with ethynylmagnesium bromide followed by methylmagnesium bromide, which generated tertiary alcohol **19** in 19:1 dr and 57% yield over the two steps. The relative configuration of the major diastereomer, which was confirmed by X-ray crystallography, was consistent with a Cram chelation controlled addition of methylmagnesium bromide.[27] Alcohol **19** was then converted to diol **20**, which was subjected to gold catalyzed 6-endo cyclization.[28] Although the

resulting tricyclic skeleton of **21** was consistent with the proposed structure of sorazolon B, the NMR data of our synthetic sample did not match the corresponding data for the natural product.

Scheme 4.2. Synthetic Derivatization of [2,3]-Rearrangement Product

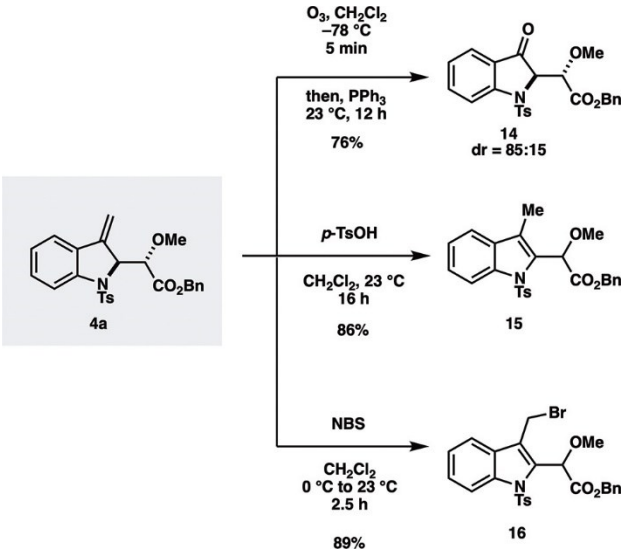

We hypothesized that the relative configuration of the two stereogenic centers in sorazolon B may have been misassigned. To test this hypothesis, we switched the order of addition of Grignard reagents to the Weinreb amide **18**. An initial addition of methylmagnesium bromide followed by a Cram chelation-controlled addition of ethynylmagnesium bromide yielded the tertiary alcohol **22** in 9:1 dr. The relative configuration of the major diastereomer was confirmed by X-ray crystallography. The treatment of methyl ether **22** with bromodimethylborane and 2-methyl-2-butene resulted in the formation of diol **23**. In the presence of $Au(MeCN)SbF_6$ and JohnPhos, diol **23** was converted to tricycle **24**, which had spectroscopic data that were identical with the data reported for sorazolon B in the original isolation paper.[26]

Scheme 4.3. Synthesis and Stereochemical Reassignment of (±)-Sorazolon B from [1,2]-Rearrangement Product

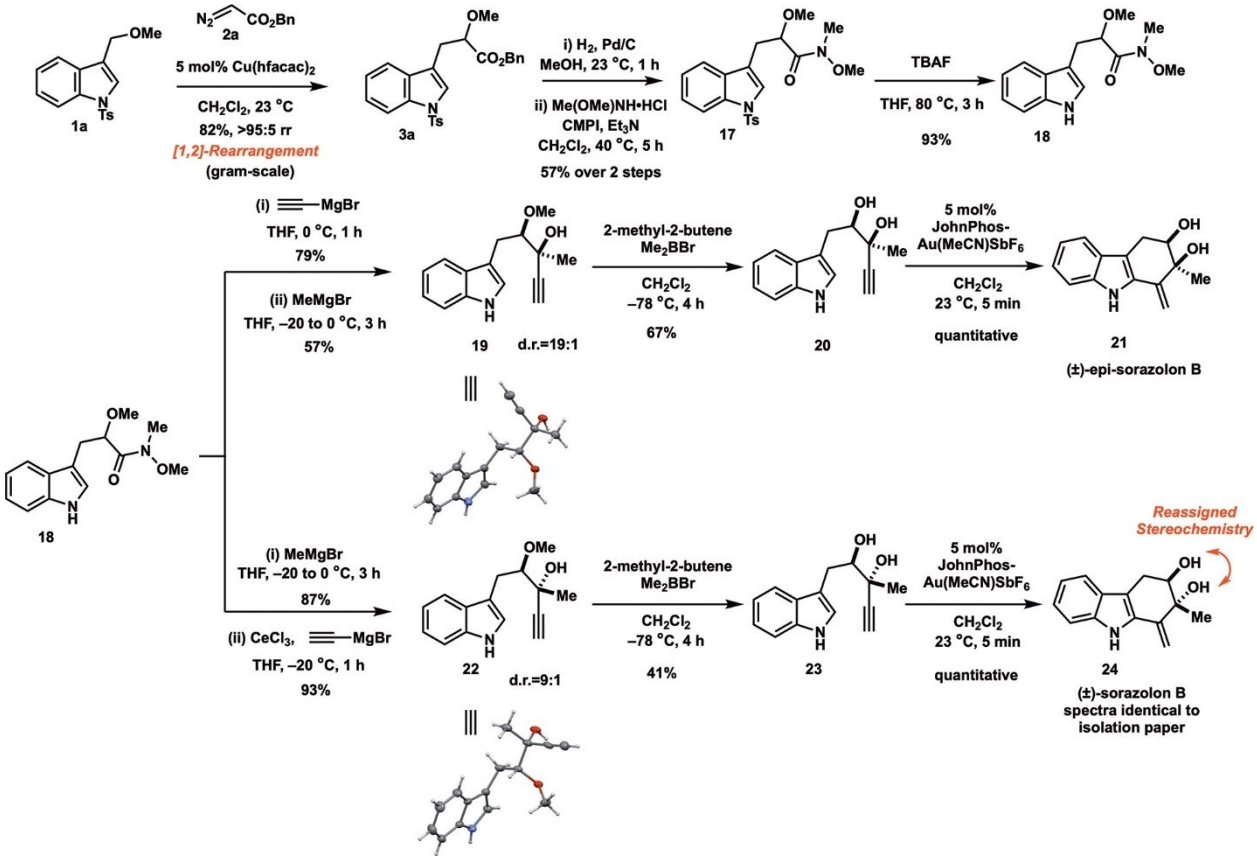

4.4 Conclusion

We developed catalyst-controlled regiodivergent rearrangements of onium-ylides derived from indole methyl ethers and diazoesters. While a copper catalyst promotes a regioselective [1,2]-rearrangement, a rhodium catalyst facilitates a regioselective and diastereoselective [2,3]-rearrangement. We present experimental and computational studies that support divergent mechanistic pathways for the two rearrangement processes. We also describe the synthetic utility of the two rearrangements by demonstrating the functional group tolerance and scope of the reactions as well as the transformation of the rearrangement products to several indole-containing products. Finally, we applied the copper-catalyzed [1,2]-

rearrangement in the first total synthesis of the indole alkaloid sorazolon B, which enabled the stereochemical reassignment of the natural product.

4.5 Acknowledgements

Financial support was provided to U.K.T by W. W. Caruth, Jr. Endowed Scholarship, Welch Foundation (I-1748), National Institutes of Health (R01GM102604), American Chemical Society Petroleum Research Fund (59177-ND1), Teva Pharmaceuticals Marc A. Goshko Memorial Grant (60011-TEV), and Sloan Research Fellowship. Financial support was provided to V.N.N by Sarah and Frank McKnight Fund Graduate Fellowship. Support from the National Science Foundation (CHE-1856416 and XSEDE via CHE-030089) to D.J.T. is gratefully acknowledged. We acknowledge Dr. Vincent Lynch (Manager of the X-ray Diffraction Lab at UT Austin) for the X-ray structural analysis and Dr. Hamid Baniasadi (Director of the UT Southwestern Metabolomics Core Facility) for the high resolution mass spectrometry. We also thank our diverse group of lab members for creating an environment that supports our scientific endeavors.

4.6 Supporting Information

The supporting information is available free of charge at https://pubs.acs.org/doi/10.1021/jacs.1c00283.

Experimental details, characterization data, spectral data, and computational results (PDF)

4.7 References

(1) (a) Brückner, R. 2,3-Sigmatropic Rearrangements. In *Comprehensive Organic Synthesis*; Fleming, I., Ed.; Pergamon: Oxford, 1991; pp 873−908. (b) Ilardi, E. A.; Stivala, C. E.; Zakarian, A. [3,3]-Sigmatropic rearrangements: recent applications in the total synthesis of natural products. *Chem. Soc. Rev.* **2009**, *38*, 3133−3148. (c) Seashore-Ludlow, B.; Somfai, P. *Sigmatropic Rearrangements in Stereoselective Synthesis*; John Wiley & Sons: New York, 2013; pp 475−499. (d) Jones, A. C.; May, J. A.; Sarpong, R.; Stoltz, B. M. Toward a Symphony of Reactivity: Cascades Involving Catalysis and Sigmatropic Rearrangements. *Angew. Chem. Int. Ed.* **2014**, *53*, 2556−2591. (e) *Molecular Rearrangements in Organic Synthesis*; Rojas, C. M., Ed.; John Wiley & Sons: New York, 2016.

(2) Reviews on catalytic onium ylide rearrangements: (a) Murphy, G. K.; Stewart, C.; West, F. G. Intramolecular generation and rearrangement of oxonium ylides: methodology studies and their application in synthesis. *Tetrahedron* **2013**, *69*, 2667−2686. (b) Hodgson, D. M.; Pierard, F. Y. T. M.; Stupple, P. A. Catalytic enantioselective rearrangements and cycloadditions involving ylides from diazo compounds. *Chem. Soc. Rev.* **2001**, *30*, 50−61. (c) West, T. H.; Spoehrle, S. S. M.;

Kasten, K.; Taylor, J. E.; Smith, A. D. Catalytic Stereoselective [2,3]-Rearrangement Reactions. *ACS Catal.* **2015**, *5*, 7446−7479. (d) Murphy, G. K.; West, F. G. In *Molecular Rearrangements in Organic Synthesis*; Rojas, C., Ed.; John Wiley Sons: Hoboken, NJ, 2015; pp 497−538. (e) Sheng, Z.; Zhang, Z. K.; Chu, C.; Zhang, Y.; Wang, J. Transition metal-catalyzed [2,3]-sigmatropic rearrangements of ylides: An update of the most recent advances. *Tetrahedron* **2017**, *73*, 4011−4022.

(3) (a) Books and reviews on classical non-catalytic onium ylide rearrangements: Pine, S. H. In *Organic Reactions*; Dauben, W. G., Ed.; Wiley: New York, 1970; Vol. 18 pp 403−464. (b) Nakai, T.; Mikami, K. [2,3]-Wittig sigmatropic rearrangements in organic synthesis. *Chem. Rev.* **1986**, *86*, 885-902. (c) Sweeney, J. B. Sigmatropic rearrangements of 'onium' ylides. *Chem. Soc. Rev.* **2009**, *38*, 1027-1038.

(4) Examples of catalytic oxonium ylide rearrangements of aliphatic systems: (a) Doyle, M. P.; Tamblyn, W. H.; Bagheri, V. Highly Effective Catalytic Methods for Ylide Generation from Diazo Compounds. Mechanism of the Rhodium- and Copper-Catalyzed Reactions with Allylic Compounds. *J. Org. Chem.* **1981**, *46*, 5094-5102. (b) Roskamp, E. J.; Johnson, C. R. Generation and Rearrangements of Oxonium Ylides. *J. Am. Chem. Soc.* **1986**, *108*, 6062-6063. (c) Pirrung, M. C.; Werner, J. A. Intramolecular Generation and [2,3]-Sigmatropic Rearrangement of Oxonium Ylides. *J. Am. Chem. Soc.* **1986**, *108*, 6060−6062. (d) Doyle, M. P.; Bagheri, V.; Harn, N. K. Facile catalytic methods for intermolecular generation of allylic oxonium ylides and their stereoselective [2,3]-sigmatropic rearrangement. *Tetrahedron Lett.* **1988**, *29*, 5119-5122. (e) Eberlein, T. H.; West, F. G.; Tester, R. W. The Stevens [1,2]-Shift of Oxonium Ylides: A Route to Substituted Tetrahydrofuranones. *J. Org. Chem.* **1992**, *57*, 3479-3482. (f) Clark, J. S. Diastereoselective Synthesis of 2,5-Dialkyl Tetrahydrofuran-3-ones by a Copper-Catalysed Tandem Carbenoid Insertion and Ylide Rearrangement Reaction. *Tetrahedron Lett.* **1992**, *33*, 6193−6196. (g) Clark, J. S.; Krowiak, S. A.; Street, L. J. Synthesis of Cyclic Ethers from Copper Carbenoids by Formation and Rearrangement of Oxonium Ylides. *Tetrahedron Lett.* **1993**, *34*, 4385-4388. (h) West, F. G.; Eberlein, T. H.; Tester, R. W. O-Bridged Medium Sized Rings via Bicyclic Oxonium Ylides. *J. Chem. Soc., Perkin Trans. 1* **1993**, 2857-2859. (i) West, F. G.; Naidu, B. N.; Tester, R. W. Profound Catalyst Effects in the Generation and Reactivity of Carbenoid-Derived Cyclic Ylides. *J. Org. Chem.* **1994**, *59*, 6892-6894. (j) Doyle, M. P.; Ene, D. G.; Forbes, D. C.; Tedrow, J. S. Highly Enantioselective Oxonium Ylide Formation and Stevens Rearrangement Catalyzed by Chiral Dirhodium (II) Carboxamidates. *Tetrahedron Lett.* **1997**, *38*, 4367-4370. (k) Li, Z.; Davies, H. M. L. Enantioselective C-C Bond Formation by Rhodium-Catalyzed Tandem Ylide Formation/[2,3]-Sigmatropic Rearrangement between Donor/Acceptor Carbenoids and Allylic Alcohols. *J. Am. Chem. Soc.* **2010**, *132*, 396-401. (l) Li, Z.; Parr, B. T.; Davies, H. M. L. Highly Stereoselective C-C Bond Formation by Rhodium-Catalyzed Tandem Ylide Formation/[2,3]-Sigmatropic Rearrangement between Donor/Acceptor Carbenoids and Chiral Allylic Alcohols. *J. Am. Chem. Soc.* **2012**, *134*, 10942-10946. (m) Doyle, M. P.; Forbes, D. C.; Vasbinder, M. M.; Peterson, C. S. Enantiocontrol in the Generation and Diastereoselective Reactions of Catalytically Generated Oxonium and Iodonium Ylides. Metal-Stabilized Ylides as Reaction Intermediates. *J. Am. Chem. Soc.* **1998**, *120*, 7653-7654. (n) Li, Z.; Boyarskikh, V.; Hansen, J. H.; Autschbach, J.; Musaev, D. G.; Davies, H. M. L. Scope and Mechanistic Analysis of the Enantioselective Synthesis of Allenes by Rhodium-Catalyzed Tandem Ylide Formation/[2,3]-Sigmatropic Rearrangement between Donor/Acceptor Carbenoids and Propargylic Alcohols. *J. Am. Chem. Soc.* **2012**, *134*, 15497-15504.

(5) Examples of catalytic ammonium, sulfonium, and iodonium ylide rearrangements of aliphatic systems: (I) *Ammonium (X = N) ylides*: (a) West, F. G.; Glaeske, K. W.; Naidu, B. N. One-Step Synthesis of Tertiary α-Amino Ketones And α-Amino Esters from Amines and Diazocarbonyl Compounds. *Synthesis* **1993**, *1993*, 977−980. (b) West, F. G.; Naidu, B. N. New Route to Substituted Piperidines via the Stevens [1,2]-Shift of Ammonium Ylides. *J. Am. Chem. Soc.* **1993**, *115*, 1177-1178. (c) Clark, J. S.; Hodgson, P. B. Intramolecular Generation and Rearrangement of Ammonium

Ylides from Copper Carbenoids: A General Method for the Synthesis of Cyclic Amines. *J. Chem. Soc., Chem. Commun.* **1994**, 2701-2702. (d) West, F. G.; Naidu, B. N. Piperidines via Ammonium Ylide [1,2]-Shifts: A Concise, Enantioselective Route to (−)-Epilupinine From Proline Ester. *J. Am. Chem. Soc.* **1994**, *116*, 8420-8421. (e) Clark, J. S.; Hodgson, P. B.; Goldsmith, M. D.; Street, L. J. Rearrangement of ammonium ylides produced by intramolecular reaction of catalytically generated metal carbenoids. Part 1. Synthesis of cyclic amines. *J. Chem. Soc., Perkin Trans. 1* **2001**, 3312-3324. (f) Clark, J. S.; Hodgson, P. B.; Goldsmith, M. D.; Blake, A. J.; Cooke, P. A.; Street, L. J. Rearrangement of ammonium ylides produced by intramolecular reaction of catalytically generated metal carbenoids. Part 2. Stereoselective synthesis of bicyclic amines. *J. Chem. Soc., Perkin Trans. 1* **2001**, 3325-3337. (g) Clark, J. S.; Middleton, M. D. Synthesis of Novel α-Substituted and α,α-Disubstituted Amino Acids by Rearrangement of Ammonium Ylides Generated from Metal Carbenoids. *Org. Lett.* **2002**, *4*, 765−768. (h) Heath, P.; Roberts, E.; Sweeney, J. B.; Wessel, H. P.; Workman, J. A. Copper(II)- Catalyzed [2,3]-Sigmatropic Rearrangement of N-Methyltetrahydropyridinium Ylides. *J. Org. Chem.* **2003**, *68*, 4083−4086. (i) Sançon, J.; Sweeney, J. B. Probing the Effect of Allylic Substitution on Cyclic Ammonium Ylid Rearrangements. *Synlett* **2010**, *2010*, 664-666 Sulfonium (X = S) ylides. (j) Doyle, M. P.; Griffin, J. H.; Chinn, M. S.; van Leusen, D. Rearrangements of Ylides Generated from Reactions of Diazo Compounds with Allyl Acetals and Thioketals by Catalytic Methods. Heteroatom Acceleration of the [2,3]-Sigmatropic Rearrangement. *J. Org. Chem.* **1984**, *49*, 1917−1925. (k) Aggarwal, V. K.; Ferrara, M.; Hainz, R.; Spey, S. E. [2,3]-Sigmatropic rearrangement of allylic sulfur ylides derived from trimethylsilyldiazomethane (TMSD). *Tetrahedron Lett.* **1999**, *40*, 8923-8927. (l) Carter, D. S.; Van Vranken, D. L. Metal-Catalyzed Ylide Formation and [2,3] Sigmatropic Rearrangement of Allyl Sulfides with Trimethylsilyldiazomethane. *Tetrahedron Lett.* **1999**, *40*, 1617−1620. (m) Hock, K. J.; Mertens, L.; Hommelsheim, R.; Spitzner, R.; Koenigs, R. M. Enabling iron catalyzed Doyle-Kirmse rearrangement reactions with *in situ* generated diazo compounds. *Chem. Commun.* **2017**, *53*, 6577-6580 (III) Iodonium (X = I) ylides:. (n) Xu, B.; Tambar, U. K. Ligand-Controlled Regiodivergence in the Copper-Catalyzed [2,3]- and [1,2]-Rearrangements of Iodonium Ylides. *J. Am. Chem. Soc.* **2016**, *138*, 12073-12076. (o) Xu, B.; Gartman, J. A.; Tambar, U. K. Copper-catalyzed [1,2]-rearrangements of allylic iodides and aryl α-diazoacetates. *Tetrahedron* **2017**, *73*, 4150-4159. (p) Xu, B.; Tambar, U. K. Copper-Catalyzed Enantio-, Diastereo-, and Regioselective [2,3]-Rearrangements of Iodonium Ylides. *Angew. Chem. Int. Ed.* **2017**, *56*, 9868-9871.

(6) Catalytic aromatic rearrangements with *sulfonium* (X = S) ylides: (a) Kennedy, A. R.; Taday, M. H.; Rainier, J. D. The Use of Sulfur Ylides in the Synthesis of Substituted Indoles. *Org. Lett.* **2001**, *3*, 2407-2409. (b) Novikov, A. V.; Kennedy, A. R.; Rainier, J. D. Sulfur Ylide-Initiated Thio-Claisen Rearrangements. The Synthesis of Highly Substituted Indolines. *J. Org. Chem.* **2003**, *68*, 993-996. (c) Liao, M.; Peng, L.; Wang, J. Rh(II)-Catalyzed Sommelet-Hauser Rearrangement. *Org. Lett.* **2008**, *10*, 693-696. (d) Boyarskikh, V.; Nyong, A.; Rainier, J. D. Highly Diastereoselective Sulfonium Ylide Rearrangements to Quaternary Substituted Indolines. *Angew. Chem. Int. Ed.* **2008**, *47*, 5374−5377. (e) Li, Y.; Shi, Y.; Huang, Z.; Wu, X.; Xu, P.; Wang, J.; Zhang, Y. Catalytic Thia-Sommelet-Hauser Rearrangement: Application to the Synthesis of Oxindoles. *Org. Lett.* **2011**, *13*, 1210-1213. (f) Li, S.-S.; Wang, J. Cu(I)/Chiral Bisoxazoline-Catalyzed Enantioselective Sommelet-Hauser Rearrangement of Sulfonium Ylides. *J. Org. Chem.* **2020**, *85*, 12343-12358 Catalytic aromatic rearrangements with *ammonium* (X = N) ylides:. (g) Pan, C.; Guo, W.; Gu, Z. Unusual biaryl torsional strain promotes reactivity in Cucatalyzed Sommelet-Hauser rearrangement. *Chem. Sci.* **2018**, *9*, 5850-5854.

(7) (a) Hansen, H. J.; Schmid, H. Aromatic Sigmatropic Rearrangements. *Chem. Br.* **1969**, *5*, 111-116. (b) Murray, A. W. Molecular rearrangements. *Org. React. Mech.* **2002**, 487-615. (c) Snape, T. J. In *Aromatic Rearrangements in Which the Migrating Group Migrates to the Aromatic Nucleus: An Overview*; John Wiley & Sons, Inc.: 2015; pp 485-510.

(8) (a) Xu, X.; Li, C.; Xiong, M.; Tao, Z.; Pan, Y. Hemin-catalyzed sulfonium ylide formation and

subsequently reactant-controlled chemoselective rearrangements. *Chem. Commun.* **2017**, *53*, 6219-6222. (b) Yang, Z.; Guo, Y.; Koenigs, R. M. Solvent-dependent, rhodium catalyzed rearrangement reactions of sulfur ylides. *Chem. Commun.* **2019**, *55*, 8410-8413.

(9) Wang, J. In *Comprehensive Organometallic Chemistry III*; Crabtree, R. H.; Mingos, D. M. P., Eds.; Elsevier: Oxford, U.K., 2007; Vol. *11*, pp 151-178.

(10) (a) Kochanowska-Karamyan, A. J.; Hamann, M. T. Marine Indole Alkaloids: Potential New Drug Leads for the Control of Depression and Anxiety. *Chem. Rev.* **2010**, *110*, 4489-4497. (b) Kaushik, N.; Kaushik, N.; Attri, P.; Kumar, N.; Kim, C.; Verma, A.; Choi, E. Biomedical Importance of Indoles. *Molecules* **2013**, *18*, 6620−6662. (c) Vitaku, E.; Smith, D. T.; Njardarson, J. T. Analysis of the Structural Diversity, Substitution Patterns, and Frequency of Nitrogen Heterocycles Among U. S. FDA Approved Pharmaceuticals. *J. Med. Chem.* **2014**, *57*, 10257-10274.

(11) (a) Doyle, M. P. Catalytic Methods for Metal Carbene Transformations. *Chem. Rev.* **1986**, *86*, 919-939. (b) Liu, L.; Zhang, J. Gold-catalyzed transformations of α-diazocarbonyl compounds: selectivity and diversity. *Chem. Soc. Rev.* **2016**, *45*, 506-516. (c) DeAngelis, A.; Panish, R.; Fox, J. M. Rh-Catalyzed Intermolecular Reactions of *α*-Alkyl-*α*-Diazo Carbonyl Compounds with Selectivity Over β-Hydride Migration. *Acc. Chem. Res.* **2016**, *49*, 115-127. (d) Zhao, X.; Zhang, Y.; Wang, J. Recent developments in copper-catalyzed reactions of diazo compounds. *Chem. Commun.* **2012**, *48*, 10162-10173.

(12) (a) Doyle, M. P. Metal Carbene Reactions from Dirhodium (II) Catalysts. *Top. Organomet. Chem.* **2004**, *13*, 203-222. (b) Davies, H. M. L.; Parr, B. T. Rhodium Carbenes. *Wiley Ser. React. Intermed. Chem. Biol.* **2013**, *7*, 363-403.

(13) Select examples for the synthesis of 3-methyleneindolines: (a) Burns, B.; Grigg, R.; Sridharan, V.; Worakun, T. Palladium catalyzed tandem cyclisation-anion capture processes. Hydride ion capture by vinylpalladium species. *Tetrahedron Lett.* **1988**, *29*, 4325-4328. (b) Zenner, J. M.; Larock, R. C. Palladium-Catalyzed, Asymmetric Hetero- and Carboannulation of Allenes Using Functionally Substituted Aryl and Vinylic Iodides. *J. Org. Chem.* **1999**, *64*, 7312−7322. (c) Font, M.; Cendón, B.; Seoane, A.; Mascareñas, J. L.; Gulías, M. Rhodium (III)-Catalyzed Annulation of 2-Alkenyl Anilides with Alkynes Through C-H Activation: Direct Access to 2-Substituted Indolines. *Angew. Chem. Int. Ed.* **2018**, *57*, 8255-8259. (d) Kondoh, A.; Terada, M. Brønsted Base-Catalyzed Umpolung Intramolecular Cyclization of Alkynyl Imines. *Chem. - Eur. J.* **2018**, *24*, 3998-4001. (e) Li, X.; Zhou, B.; Yang, R.-Z.; Yang, F.-M.; Liang, R.-X.; Liu, R.-R.; Jia, Y.-X. Palladium-Catalyzed Enantioselective Intramolecular Dearomative Heck Reaction. *J. Am. Chem. Soc.* **2018**, *140*, 13945-13951.

(14) When subjected to the [2,3]-rearrangement conditions, indole **3f** proceeded to give a mixture of [2,3]:[1,2] rearrangement products. We presume that the 2-methyl substituent hinders the [2,3]-rearrangement that forms the fully substituted carbon center and increases the propensity for the ylide to dissociate and generate the competitive [1,2]-rearrangement product (see SI for details).

(15) (a) Becke, A. D. Density-Functional Thermochemistry. III. The Role of Exact Exchange. *J. Chem. Phys.* **1993**, *98*, 5648-5652. (b) Lee, C.; Yang, W.; Parr, R. G. Development of the Colle-Salvetti Correlation-Energy Formula into a Functional of the Electron Density. *Phys. Rev. B: Condens. Matter Mater. Phys.* **1988**, *37*, 785-789. (c) Grimme, S.; Ehrlich, S.; Goerigk, L. Effect of the Damping Function in Dispersion Corrected Density Functional Theory. *J. Comput. Chem.* **2011**, *32*, 1456-1465. (d) Hariharan, P. C.; Pople, J. A. The Influence of Polarization Functions on Molecular Orbital Hydrogenation Energies. *Theor. Chim. Acta* **1973**, *28*, 213-222. (e) Igel-Mann, G.; Stoll, H.; Preuss, H. Pseudopotentials for Main Group Elements (IIIa through VIIa). *Mol. Phys.* **1988**, *65*, 1321-1328. (f) Hay, P. J.; Wadt, W. R. Ab Initio Effective Core Potentials for Molecular Calculations. Potentials for the Transition Metal Atoms Sc to Hg. *J. Chem. Phys.* **1985**, *82*, 270-283. (g) Goerigk, L.; Grimme, S. Efficient and Accurate Double-Hybrid-Meta-GGA Density Functionals−Evaluation with the Extended GMTKN30 Database for General Main Group Thermochemistry, Kinetics, and Noncovalent Interactions. *J. Chem. Theory Comput.* **2011**, *7*, 291-

309. (h) Weigend, F.; Ahlrichs, R. Balanced basis sets of split valence, triple zeta valence and quadruple zeta valence quality for H to Rn: Design and assessment of accuracy. *Phys. Chem. Chem. Phys.* **2005**, *7*, 3297-3305. (i) Weigend, F. Accurate Coulomb-fitting basis sets for H to Rn. *Phys. Chem. Chem. Phys.* **2006**, *8*, 1057-1065. (j) Hellweg, A.; Hättig, C.; Höfener, S.; Klopper, W. Optimized Accurate Auxiliary Basis Sets for RI-MP2 and RI-CC2 Calculations for the Atoms Rb to Rn. *Theor. Chem. Acc.* **2007**, *117*, 587-597. (k) Chmela, J.; Harding, M. E. Optimized Auxiliary Basis Sets for Density Fitted Post-Hartree-Fock Calculations of Lanthanide Containing Molecules. *Mol. Phys.* **2018**, *116*, 1523-1538.

(16) (a) Hock, K. J.; Koenigs, R. M. Enantioselective [2,3]-Sigmatropic Rearrangements: Metal-Bound or Free Ylides as Reaction Intermediates? *Angew. Chem. Int. Ed.* **2017**, *56*, 13566-13568. (b) Zhang, Z.; Sheng, Z.; Yu, W.; Wu, G.; Zhang, R.; Chu, W.-D.; Zhang, Y.; Wang, J. Catalytic asymmetric trifluoromethylation via enantioselective [2,3]-sigmatropic rearrangement of sulfonium ylides. *Nat. Chem.* **2017**, *9*, 970-976. (c) Harrison, J. G.; Gutierrez, O.; Jana, N.; Driver, T. G.; Tantillo, D. J. Mechanism of Rh_2(II)-Catalyzed Indole Formation: The Catalyst Does Not Control Product Selectivity. *J. Am. Chem. Soc.* **2016**, *138*, 487-490. (d) Nickerson, L. A.; Bergstrom, B. D.; Gao, M.; Shiue, Y.-S.; Laconsay, C. J.; Culberson, M. R.; Knauss, W. A.; Fettinger, J. C.; Shaw, J. T.; Tantillo, D. J. Enantioselective synthesis of isochromans and tetrahydroisoquinolines by C-H insertion of donor/donor carbenes. *Chem. Sci.* **2020**, *11*, 494-498. (e) Laconsay, C. J.; Tantillo, D. J. Metal Bound or Free Ylides as Reaction Intermediates in Metal-Catalyzed [2,3]-Sigmatropic Rearrangements? It Depends. *ACS Catal.* **2021**, *11*, 829-839. (f) Li, F.; Pei, C.; Koenigs, R. M. Rhodium-catalyzed cascade reactions of triazoles with organoselenium compounds - a combined experimental and mechanistic study. *Chem. Sci.* **2021**, *12*, 6362-6369.

(17) In addition, when two distinct substrates were simultaneously subjected to the [2,3]-rearrangement conditions, no crossover products were detected (see SI for details). These observations are consistent with a metal-free symmetry-allowed, concerted, and unimolecular process.

(18) Other stepwise mechanisms were considered and cannot be definitively ruled out, including a fragmentation/recombination pathway (see SI).

(19) (a) Ollis, W. D.; Rey, M.; Sutherland, I. O.; Closs, G. L. The Mechanism of Stevens Rearrangement. *J. Chem. Soc., Chem. Commun.* **1975**, 543-545. (b) Chantrapromma, K.; Ollis, W. D.; Sutherland, I. O. Radical-coupling Products Derived from Ammonium Ylides. Competing [1,2], [1,3], and [1,4] Anionic Rearrangements. *J. Chem. Soc., Chem. Commun.* **1978**, 670-671. (c) Heard, G. L.; Frankcombe, K. E.; Yates, B. F. A. Theoretical Study of the Stevens Rearrangement of Methylammonium Methylide and Methylammonium Formylmethylide. *Aust. J. Chem.* **1993**, *46*, 1375-1388. (d) Liu, Z.; Jin, X.; Dang, Y. Mechanistic Studies of Copper(I)-Catalyzed Stereoselective [2,3]- Sigmatropic Rearrangements of Diazoesters with Allylic Iodides/ Sulfides. *ACS Catal.* **2021**, *11*, 691-702.

(20) (a) Hogen-Esch, T. E.; Smid, J. Studies of Contact and Solvent-Separated Ion Pairs of Carbanions. I. Effect of Temperature, and Solvent. *J. Am. Chem. Soc.* **1966**, *88*, 307-318. (b) Roy, S.; Baer, M. D.; Mundy, C. J.; Schenter, G. K. Marcus Theory of Ion-Pairing. *J. Chem. Theory Comput.* **2017**, *13*, 3470-3477. (c) Macchioni, A. Ion Pairing in Transition-Metal Organometallic Chemistry. *Chem. Rev.* **2005**, *105*, 2039-2073. (d) Brak, K.; Jacobsen, E. N. Asymmetric Ion-Pairing Catalysis. *Angew. Chem. Int. Ed.* **2013**, *52*, 534-561. (e) Chen, Y.; Liu, Y.; Li, Z.; Dong, S.; Liu, X.; Feng, X. Tandem Insertion-[1,3]-Rearrangement: Highly Enantioselective Construction of α-Aminoketones. *Angew. Chem.* **2020**, *132*, 8129-8133. (f) Yao, L.; Ishihara, K. Enantioselective [1,3] O-to-C Rearrangement: Dearomatization of Alkyl 2-Allyloxy/Benzyloxy-1/3-Naphthoates Catalyzed by a Chiral π-Cu(II) Complex. *Chem. Sci.* **2019**, *10*, 2259-2263. (g) Tsuji, Y.; Richard, J. P. Reactions of Ion-Pair Intermediates of Solvolysis. *Chem. Rec.* **2005**, *5*, 94-106.

(21) Bowry, V. W.; Lusztyk, J.; Ingold, K. U. Calibration of a New Horology of Fast Radical "Clocks". Ring-Opening Rates for Ringand α-Alkyl-Substituted Cyclopropylcarbinyl Radicals and for the Bicyclo[2.1.0]pent-2-yl Radical. *J. Am. Chem. Soc.* **1991**, *113*, 5687-5698.

(22) We do note, however, that some ion-pairs appear to have diradical character (see SI).

(23) Computed relative free energies of ion-pairs **12a-12e** with respect to the reactants were calculated using PWPB95-D3(BJ)/def2-QZVPP//IEFPCM(CH2Cl2)-B3LYP/6-31G(d),SDD, which is used to more accurately capture dispersion effects, but the accuracy of the computed energies is limited because explicit solvent was not included.

(24) de Azambuja, F.; Yang, M. H.; Feoktistova, T.; Selvaraju, M.; Brueckner, A. C.; Grove, M. A.; Koley, S.; Cheong, P. H. Y.; Altman, R. A. Connecting remote C-H bond functionalization and decarboxylative coupling using simple amines. *Nat. Chem.* **2020**, *12*, 489-496.

(25) (a) Fang, Y.; Powell, J. A.; Li, E.; Wang, Q.; Perry, Z.; Kirchon, A.; Yang, X.; Xiao, Z.; Zhu, C.; Zhang, L.; Huang, F.; Zhou, H.-C. Catalytic Reactions within the Cavity of Coordination Cages. *Chem. Soc. Rev.* **2019**, *48*, 4707-4730. (b) Stelson, A. C.; Hong, C. M.; Groenenboom, M. C.; Little, C. A. E.; Booth, J. C.; Orloff, N. D.; Bergman, R. G.; Raymond, K. N.; Schwarz, K. A.; Toste, F. D.; Long, C. J. Measuring ion-pairing and hydration in variable charge supramolecular cages with microwave microfluidics. *Commun. Chem.* **2019**, *2*, 54.

(26) Karwehl, S.; Jansen, R.; Huch, V.; Stadler, M. Sorazolons, Carbazole Alkaloids from Sorangium cellulosum Strain Soce375. *J. Nat. Prod.* **2016**, *79*, 369-375.

(27) (a) Cram, D. J.; Elhafez, F. A. A. Studies in Stereochemistry. X. The Rule of ‘ Steric Control of Asymmetric Induction” in the Syntheses of Acyclic Systems. *J. Am. Chem. Soc.* **1952**, *74*, 5828-5835. (b) Reetz, M. T. Chelation or Non-Chelation Control in Addition Reactions of Chiral α- and β- Alkoxy Carbonyl Compounds [New Synthetic Methods (44)]. *Angew. Chem. Int. Ed.* **1984**, *23*, 556-569. (c) Mengel, A.; Reiser, O. Around and beyond Cram’s Rule. *Chem. Rev.* **1999**, *99*, 1191-1223.

(28) Ferrer, C.; Echavarren, A. M. Gold-Catalyzed Intramolecular Reaction of Indoles with Alkynes: Facile Formation of Eight-Membered Rings and an Unexpected Allenylation. *Angew. Chem. Int. Ed.* **2006**, *45*, 1105-1109.

Chapter 5. Exploiting the Potential of Meroterpenoid Cyclases to Expand the Chemical Space of Fungal Meroterpenoids

This chapter is adapted with slight modifications with permission from Mitsuhashi, T.[#]; Barra, L.[#]; Powers, Z.[#]; Kojasoy, V.[#]; Cheng, A.; Yang, F.; Taniguchi, Y.; Kikuchi, T.; Fujita, M.; Tantillo, D. J.; Porco, J. A., Jr.; Abe, I. Exploiting the Potential of Meroterpenoid Cyclases to Expand the Chemical Space of Fungal Meroterpenoids. *Angew. Chem. Int. Ed.* **2020**, *59*, 23772-23781 ([#] equal contribution). Copyright 2020 John Wiley & Sons, Inc. Takaaki Mitsuhashi and Lena Barra (of Prof. Ikuro Abe's group) completed the experiments for the enzyme reactions. Zachary Powers, Andrea Cheng and Feng Yang (of Prof. John A. Porco Jr.'s group) completed the experiments for the chemical synthesis of the substrates for the enzyme reactions. Yoshimasa Taniguchi and Takashi Kikuchi (of Prof. Makoto Fujita's group) completed the crystalline sponge method analysis of enzyme products.

5.1 Abstract

Fungal meroterpenoids are a diverse group of hybrid natural products with impressive structural complexity and high potential as drug candidates. In this work, we evaluate the promiscuity of the early structure diversity-generating step in fungal meroterpenoid biosynthetic pathways: the multiband-forming polyene cyclizations catalyzed by the yet poorly understood family of fungal meroterpenoid cyclases. In total, 12 unnatural meroterpenoids were accessed chemoenzymatically using synthetic substrates. Their complex structures were determined by 2D NMR studies as well as crystalline-sponge-based X-ray diffraction analyses. The results obtained revealed a high degree of enzyme promiscuity and experimental results which together with quantum chemical calculations provided a deeper insight into the catalytic activity of this new family of non-canonical, terpene cyclases. The knowledge obtained paves the way to design and engineer artificial pathways towards second generation meroterpenoids with valuable bioactivities based on combinatorial biosynthetic strategies.

5.2 Introduction

Fungal meroterpenoids have earned significant interest from the scientific community as well as from the pharmaceutical and chemical industry due to their remarkable structural architectures and potent bioactivities.[1] Pyripyropene A (**1**), isolated from *Aspergillus fumigatus*, is the strongest known inhibitor of acyl-CoA:cholesterol acyltransferase and is being developed for the treatment of atherosclerosis.[2] Additionally, **1** exhibits insecticidal properties and a commercial insecticide based on the pyripyropene core structure has been recently marketed.[3] Derivatives of mycophenolic acid (**2**), isolated from *Penicillium* sp., are clinically used immunosuppressant drugs and inhibit inosine 5'-monophosphate dehydrogenase.[4] Andrastin A (**3**) from *Penicillium albocoremium* is an inhibitor of protein farnesyl transferase and a potent anti-cancer agent,[5] whereas tropolactone D (**4**) from *Aspergillus* sp. is a cytotoxic agent against human colon carcinoma (Figure 5.1A).[6] The genetic basis for fungal meroterpenoid biosynthesis has only been elucidated in recent years, with the first biosynthetic gene cluster reported for pyripyropene A in 2010.[7]

Since then, the discovery of several related gene clusters revealed a common modular assembly logic for all meroterpenoid pathways, composed of i) building block generation (polyketide synthase, oligoprenyl synthase), ii) assembly of building blocks (prenyltransferase), iii) early structural diversification by an epoxidase enzyme followed by action of a novel family of terpene cyclases and iv) late stage diversification by tailoring enzymes such as cytochrome P450 monooxygenases and α-ketoglutarate-dependent dioxygenases.[8] Their strong biological activities as well as the conserved modular logic of their biosynthetic pathways make meroterpenoids attractive targets for artificial pathway engineering to generate novel structures with new and improved activities. Herein, we set out to evaluate the potential of meroterpenoid cyclases to generate novel scaffolds by employing natural and unnatural synthetic substrate analogues. The results obtained provide valuable information on matching pathway combinations regarding the interchangeability of employed meroterpenoid cyclases. At the same time, chemoenzymatic access to eight new scaffolds, thus far unprecedented from natural sources or chemical, biomimetic polyene cyclizations, could be achieved.

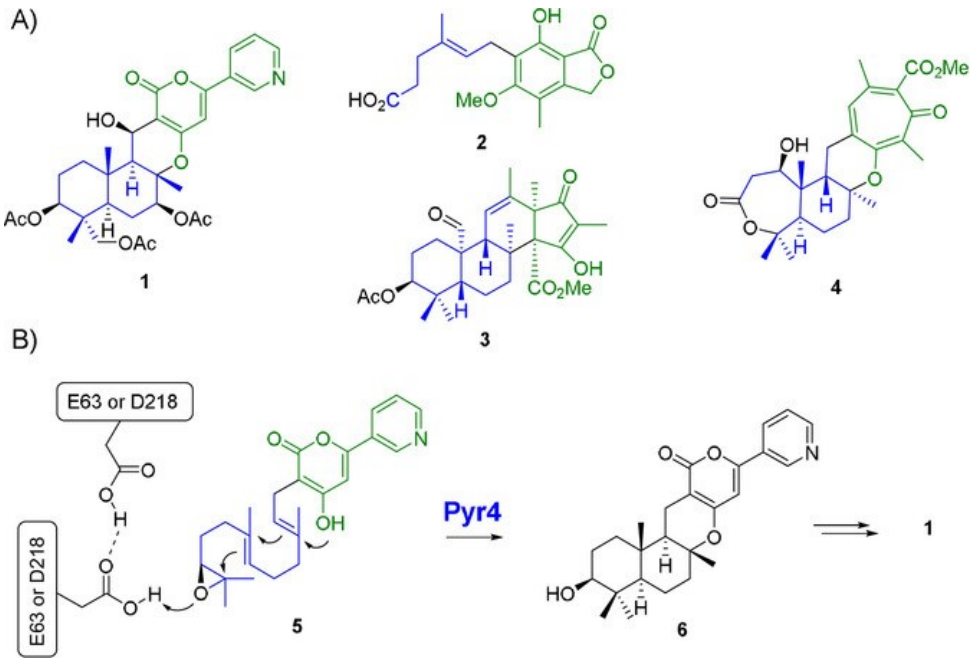

Figure 5.1. A) Selected examples of fungal meroterpenoids. B) Proposed catalytic mechanism of meroterpenoid cyclases exemplified by Pyr4-mediated reaction of epoxyfarnesyl-HPPO (**5**) to deacetyl pyripyropene E (**6**). The polyketide portion is shown in green, terpenoid in blue.

5.3 Results and Discussion

5.3.1 Targeted Enzymes and Synthesis of Substrates

Non-canonical terpene cyclases involved in meroterpenoid biosynthesis are integral membrane proteins of compact size (ca. 25 kDa).[7, 8] Mutagenesis studies on the model cyclase Pyr4 involved in the pyripyropene biogenesis revealed two highly conserved acidic amino acid residues (Glu63 and Asp218) crucial for enzyme function which are proposed to initiate polyene cyclization by protonation of the terminal epoxide function of the substrate thereby triggering subsequent polyene cyclization (Figure 5.1B). The mechanism resembles that of type-II terpene synthases of the 2,3-oxidosqualene-lanosterol cyclase type; however, protein structural data to evaluate the mechanism of meroterpenoid cyclases is still lacking.[7–9] Phylogenetic analysis of characterized meroterpenoid cyclases shows a close relation to the group of Pyr4-like synthases involved in fungal indole diterpene biosynthesis (LtmB, AtmB, and PaxB) and a distant relation to the bacterial enzymes XiaE and DmtA1 (Figure 5.2).[10] The protein sequence alignment for selected enzymes is shown in the SI.

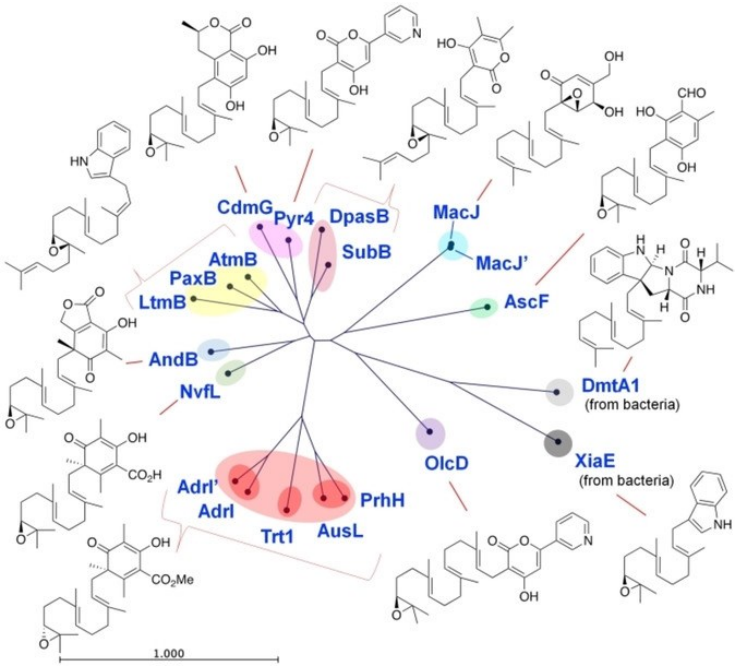

Figure 5.2. Phylogenetic analysis of reported meroterpenoid cyclases and their respective native substrates.

The substrates of known meroterpenoid cyclases are composed of a linear epoxyoligoprenyl chain, in most cases derived from farnesyl diphosphate (FPP) and a distinct nonterpenoid portion usually generated by a designated polyketide synthase (Figure 5.2). These biosynthetic intermediates are difficult to obtain from enzymatic reactions, since typically low concentrations are observed and the frequently employed heterologous expression host *Aspergillus oryzae* contains endogenous hydrolases producing high amounts of a shunt diol product.[7] To overcome this limitation, we recently developed a modular synthesis of the widespread 3,5-dimethylorsellinic acid (DMOA)-containing substrate family. The methodology involves base-mediated, regioselective dearomatization of DMOA with farnesyl electrophiles.[11] We expanded the synthetic scope by employing enantiopure (10R)- and (10S)-epoxyfarnesyl building blocks in this reaction to obtain the naturally occurring substrates (10R)- and (10S)-(2E,6E)-5'-DMOA methyl ester (**7a**, **7b**), as well as (10R)- and (10S)-(2E,6E)-3'-DMOA methyl ester (**8a**, **8b**). Additionally, we also accessed unnatural substrates including the (2Z,6E)-epoxyfarnesyl congeners (10R)- and (10S)-(2Z,6E)-5'-DMOA methyl ester (**9a**, **9b**) and (10R)- and (10S)-(2Z,6E)-3'-DMOA methyl ester (**10a**, **10b**) using the same strategy (Figure 5.3; see SI for details). As dearomative alkylation of DMOA leads to formation of two inseparable diastereoisomers with respect to 3' and 5' dearomatization, the substrates obtained were used as diastereomeric mixtures, with fixed stereochemistry for the epoxide moiety (88–98% *ee*). With these substrates in hand, we targeted nine reported meroterpenoid cyclases: Pyr4,[7] CdmG,[12] AndB,[13] AdrI',[14] NvfL,[15] PrhH,[16] Trt1,[17] AscF,[18] and MacJ.[19]

As we did not gain access to the MacJ producer strain, we cloned the homologous protein MacJ' from *Penicillium chrysogenum* MT-12 (96% identity). The intron-free genes were expressed in the heterologous host *Saccharomyces cerevisiae* INVSc1 and cell free extracts were prepared and utilized for in vitro reactions with synthetic substrates **7a**/**7b**–**10a**/**10b**. Monitoring of the reactions by HPLC revealed a surprisingly high degree of promiscuity as several new products were detected (Table 5.1; see SI for details).

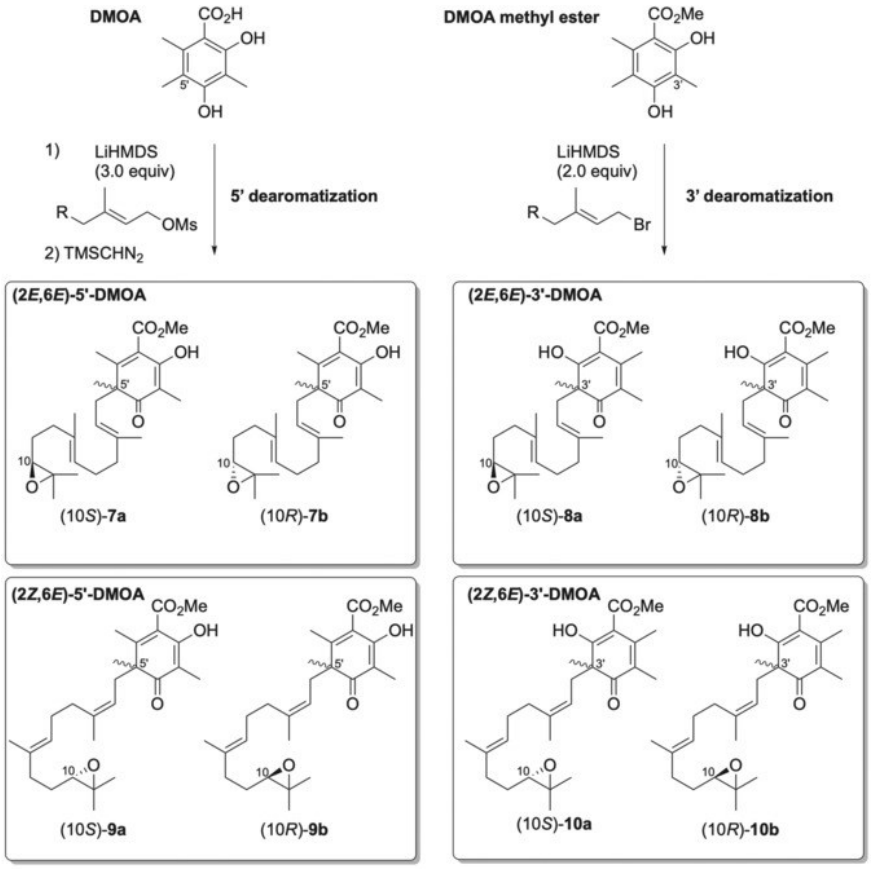

Figure 5.3. Synthetic approach and structures of obtained and tested DMOA substrates (**7a**/**7b**–**10a**/**10b**).

Table 5.1. Overview on productive enzyme substrate combinations.

	(2*E*,6*E*)-5′-DMOA	(2*E*,6*E*)-3′-DMOA	(2*Z*,6*E*)-5′-DMOA	(2*Z*,6*E*)-3′-DMOA
Pyr4	(10*S*)-**7a**	(10*S*)-**8a**	–	(10*S*)-**10a**
MacJ′	(10*S*)-**7a**	(10*S*)-**8a**	–	(10*S*)-**10a**
CdmG	(10*S*)-**7a**	(10*S*)-**8a**	(10*S*)-**9a**	(10*S*)-**10a**
AndB	(10*S*)-**7a**	(10*S*)-**8a**	(10*S*)-**9a**	–
Trt1	(10*S*)-**7a** (10*R*)-**7b**[a]	–	(10*R*)-**9b**	–
AdrI′	(10*S*)-**7a** (10*R*)-**7b**[a]	–	(10*R*)-**9b**	–
PrhH	(10*R*)-**7b**[a]	–	–	–
NvfL	–	–	–	–
AscF	–	–	–	(10*S*)-**10a**

[a] Native enzyme substrate combination.

5.3.2 Substrate Scope of Pyr4 and MacJ'

Pyr4, a cyclase which naturally utilizes the (10S)-configured epoxide **5** (Figure 5.1B), was found to accept the substrates (10S)-(2E,6E)-5'-DMOA (**7a**), (10S)-(2E,6E)-3'-DMOA (**8a**) as well as (10S)-(2Z,6E)-3'-DMOA (**10a**) based on the detection of newly formed peaks in the HPLC chromatogram (Table 5.1; see SI for details). To elucidate the structures of the putative new enzyme products, we carried out preparative scale transformations in which case reaction of Pyr4 with substrate **7a** led to the isolation of compounds **11** and **12** (Scheme 5.1A).

Both products exhibit a chair-chair conformation for the A/B ring system, as is also found for the natural cyclization to form pyripyropene E (**6**). However, the terminating cation quenching step differs for both products, leading to **11** after C–O bond formation and **12** after C–C bond formation.

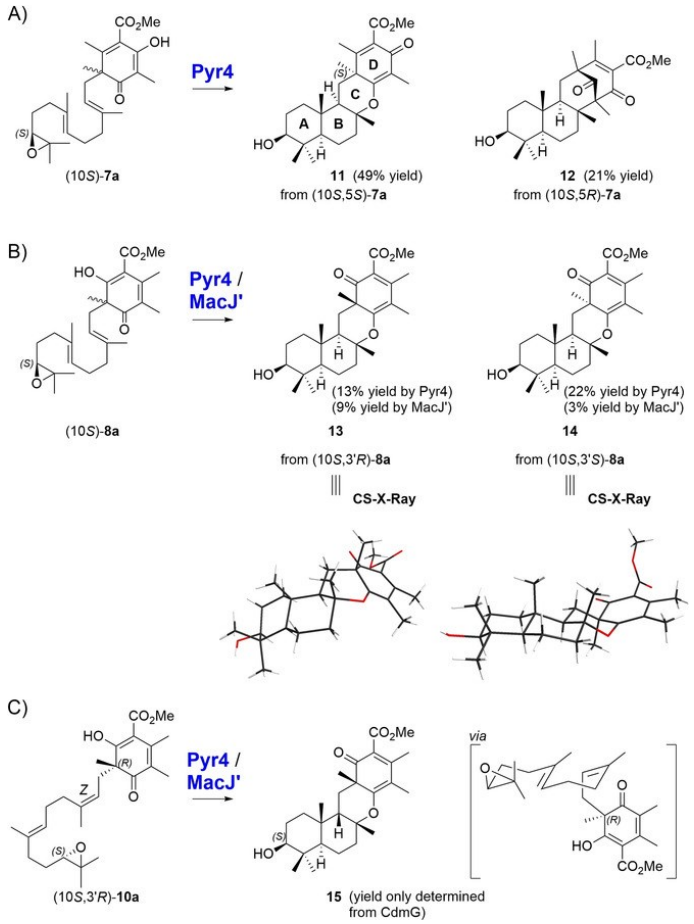

Scheme 5.1. Structures of isolated meroterpenoids obtained from Pyr4- and MacJ'-mediated reactions with A) (10S)-**7a**; B) (10S)-**8a**; C) (10S,3'R)-**10a**.

These products were also recently identified from chemical cyclization of *rac*-**7** by using $EtAlCl_2$/Et_2AlCl as Lewis acid promoter.[11] The [3.3.1] bridged structure in **12** is also found in asperterpenes A and B, recently isolated and potent BACE1 inhibitors from *Aspergillus terreus*.[20] As can be delineated from the configuration of position 5', Pyr4 is able to accept both diastereomers, (10S,5'S)-**7a** and (10S,5'R)-**7a**, to form **11** and **12**, respectively. The findings suggest that Pyr4, which usually accepts the bulkier substrate **5**, exhibits some degree of promiscuity towards changes in the polyketide portion. This is further demonstrated by the successful conversion of (10S,3'R)-**8a** to **13**, as well as (10S,3'S)-**8a** to **14**. Substrate **8a** carries the epoxyfarnesyl chain connected to the 3'-position of the DMOA-building block instead of the 5'-position as found in **7a**. Products **13** and **14** are also accessed from chair-chair substrate conformations, as observed for the natural reaction of Pyr4 towards the chair-chair product **6**. These findings indicate that the enzyme active site cavity provides a template for precise arrangement of substrate conformation and guidance of a stereochemically distinct polyene cyclization (Scheme 5.1B). Their structures were determined by 1D and 2D NMR analyses, and further confirmed by the recently developed crystalline sponge (CS) method which enables "crystallization-free" X-ray crystallography. The method makes use of crystalline porous metal complexes that can absorb and orient a compound of interest. The neat alignment of compounds in the pores of the complex makes them observable by conventional X-ray structure analysis without the need for prior crystallization.[21]

We were also interested in the flexibility of Pyr4 towards changes in the farnesyl chain and therefore subjected substrate analogues **9a**/**9b** and **10a**/**10b** to Pyr4. Indeed, Pyr4 was able to convert (10S,3'R)-**10a** to the new meroterpenoid **15** bearing a cis-fused B/C ring system, presumably derived from a chair-chair substrate conformation (Scheme 5.1C). The natural substrate of Pyr4 contains an (S)-configured epoxide functionality. Interestingly, all productive enzyme substrate combinations were restricted to the (10S)-series of substrates, as none of the analogous (10R)-epoxy substrates (10R)-**7b**,

(10R)-**8b**, (10R)-**9b** or (10R)-**10b** were accepted. This finding indicates a strict recognition of the epoxide within the substrate binding site of the enzyme. In addition, we found that MacJ' can also produce products **13** and **14** from (10S)-**8a** and **15** from (10S,3'R)-**10a** (Scheme 5.1B/C). MacJ, naturally involved in the biosynthesis of the drimane meroterpenoid macrophorin A, is one of two known Pyr4-like cyclases which do not require substrate activation by epoxidation. Instead, MacJ is able to directly protonate the terminal double bond to initiate cyclization (Figure 5.2; see SI for details). It is therefore interesting to note that MacJ' also exhibits a clear preference for the (10S)-stereoisomers of epoxide substrates evaluated (Table 5.1; see SI for details).

5.3.3 Substrate Scope of CdmG and AscF

A meroterpenoid cyclase which is phylogenetically closely related to Pyr4 is CdmG (Figure 5.2), utilized in the biosynthetic pathway towards chrodrimanins from *Penicillium verruculosum*.[12] Chrodrimanins exhibit strong inhibitory activities against protein tyrosine phosphatase 1B (PTP1B) and are potential drug candidates for the treatment of type 2 diabetes and obesity.[22] CdmG naturally catalyzes the formation of 3-hydroxypentacecilide A (**17**) from (S)-configured epoxide **16**. In contrast to Pyr4, CdmG controls the substrate conformation in a chair-boat manner, leading to an inverted stereochemical outcome for the trans-configured B/C ring system (Scheme 5.2A). With this apparent change in conformational control, we were interested in determining the substrate promiscuity of CdmG and the putative differences in product formation.

When CdmG was incubated with synthetic substrates, a high degree of promiscuity was also observed as **7a**, **8a**, **9a**, and **10a** were accepted by CdmG and led to the production of new products (Table 5.1; see SI for details). Whereas products from substrate (10S)-**7a** were found to be too unstable for structural characterization, products from substrates **8a**, **9a**, and **10a** were successfully isolated and structurally characterized. Reaction with (2E,6E)-configured substrate (10S)-**8a** led to formation of compound **18** derived from the (10S,3'S)-**8a** isomer. The structure of **18** was determined by 2D NMR analysis and was further supported by X-ray-CS-diffraction data. The stereochemical outcome of the

cyclization indeed demonstrated a conserved chair-boat conformational control of the substrate by the enzyme (Scheme 5.2B).

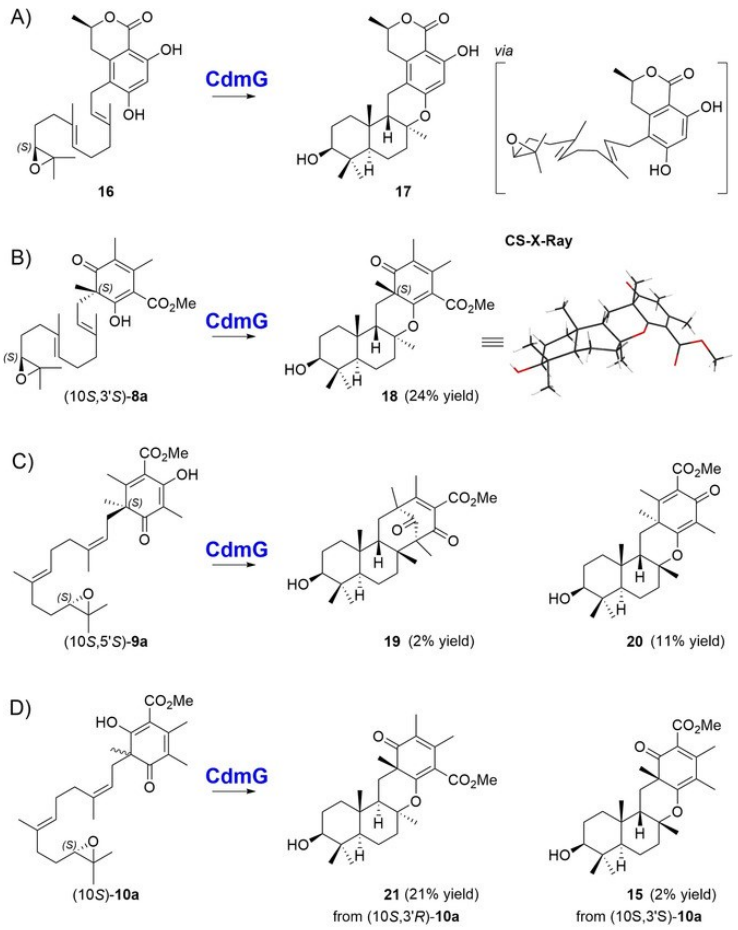

Scheme 5.2. A) Natural Reaction of CdmG and isolated meroterpenoids obtained from CdmG-mediated reactions with B) (10S,3'S)-**8a**; C) (10S,5'S)-**9a**; D) (10S)-**10a**.

Reaction of CdmG with (10S)-**9a** represents the only case where the two products found were derived from one substrate stereoisomer, in this case (10S,5'S)-**9a**, leading to the isolation of **19** and **20**. Whereas **19** is produced from a C–O bond forming event, product **20** is derived from C–C bond formation.

In both cases, the same *trans-cis* configuration is observed for the A/B/C-ring system (Scheme 5.2C). Compounds **19** and **20** have also recently been identified from chemical cyclization where it was

further shown that **20** can be rearranged to **19** by formic acid treatment.[11] To confirm the enzymatic origin of **19**, **20** was incubated under enzyme reaction conditions (KPP pH 7.4, 16 h, 30 °C) but was found to not interconvert to **19**. Reaction of CdmG with (2Z,6E)-configured substrate **10a** produced the new meroterpenoids **21** and **15**, derived from a chair-boat substrate conformation (major) and a chair-chair substrate conformation (minor), respectively. As observed for the promiscuity of Pyr4, CdmG also had a strict preference for the epoxide stereoconfiguration, as none of the (10R)-epoxides were accepted by CdmG.

AscF from the ascochlorin pathway (see SI for details) was found to also produce **21** and small amounts of **15** from (10S)-**10a** as the only accepted substrate (Table 5.1; see SI for details) and thus represents a meroterpenoid cyclase with very low tolerance towards alternative substrates.

5.3.4 Substrate Scope of AndB

The meroterpenoid cyclase AndB from the anditomin pathway[13] utilizes DMOA-derived substrate **22** with an (S)-configured epoxide to produce preandiloid A (**23**) with a chair-boat conformation (Scheme 5.3). In contrast to the results discussed for CdmG, which also controls the conformation in a chair-boat manner, AndB was found to exhibit a differing selectivity based on the 3'- and 5'-stereocenters and therefore was found to produce different products (Table 5.1; see SI for details). Specifically, AndB was found to accept (10S,3'R)-**8a** to produce the novel meroterpenoid **24** (Scheme 5.3B). Similar to CdmG and Pyr4, the native conformational control of the prenyl chain was conserved, as a chair-boat substrate arrangement was evident leading to **24**. AndB also accepted the (2Z,6E)-configured substrate (10S,5'R)-**9a** leading to the isolation of meroterpenoid **25**. The structure elucidation for **25** was challenging as 2D NMR analysis did not clearly reveal the connectivity between the terpenoid and non-terpenoid portions. Additionally, the relative configuration between the A/B and C/D ring systems were difficult to determine due to ambiguous NOESY correlations. However, we were able to fully establish the structure of **25** using crystalline sponge-X-ray analysis which revealed the presence of an unprecedented 6-5-ring system connected to a 5–6 ring system via a single C–C bond (Scheme 5.3C).

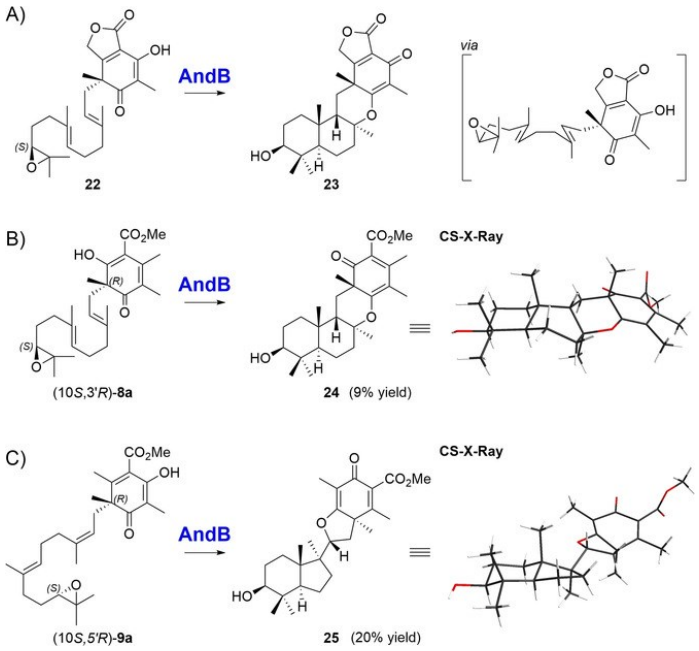

Scheme 5.3. A) Natural reaction of AndB and structures of isolated meroterpenoids obtained from AndB-mediated reactions with B) (10S,3'R)-**8a**; C) (10S,5'R)-**9a**.

5.3.5 DFT Calculations for the Formation of 25, 20, CC, and 19

The latter finding was surprising, as all reactions in this study lead to the formation of 6-6-ring systems for the A/B rings and also no natural cyclization towards 6-5-ring systems has been reported thus far. To gain further insight into the cyclization mechanism for the formation of **25** from (10S,5'R)-**9a** by AndB, we conducted computational studies using density functional theory (DFT) at the B3LYP-D3(BJ)/6-31G(d,p)//B3LYP/6-31G(d,p) and CPCM(H_2O)-B3LYP-D3(BJ)/6-31G(d,p)//B3LYP/6-31G(d,p) levels[23] (see SI for details). The results (Figure 5.4) revealed that the first intermediate in the reaction cascade (modelled here in the absence of enzyme) is the monocyclic tertiary cation **A**, generated by an endergonic process via transition state **9a-TS**. **A** is then converted to **25**-H^+ by an exergonic concerted process consisting of formation of the 5-membered B-ring in tandem with nucleophilic attack of the adjacent oxygen functionality via transition state **A-TS**. Inclusion of implicit solvent (CPCM(H_2O), in parentheses; single point calculations on previously optimized geometries in gas phase) led to lower barriers (Figure 5.4).[24, 25]

With either a nonpolar (gas phase) or polar (water) surroundings, the barrier for initial cyclization is high for a biological reaction,[26] however, in the absence of enzyme, reactant (10S,5'R)-**9a**-H^+ relaxes to a non-productive conformation with an internal hydrogen-bond between the alcohol and epoxide; consequently, conformational preorganization by the enzyme should lower the barrier and this could be assisted by specific oriented noncovalent interactions with the transition state structure. An alternative mechanism for formation of the second ring could involve Markovnikov addition to form a 6-6 intermediate, followed by ring-contraction in concert with tetrahydrofuran ring formation. We find, however, that Markovnikov addition leads directly to a "6-6-6-6" product (**C**) that is not experimentally observed. We were able to optimize tertiary carbocation **B** as a minimum and this species can then undergo ring contraction to yield **25**-H^+, but accessing **B** would require escape from the deep energy well associated with **C** and a large conformational change. The enzyme would, however, have to distinguish between **A-TS** and **A'-TS**, again by conformational biasing and/or well-placed noncovalent interactions with the transition state structure.

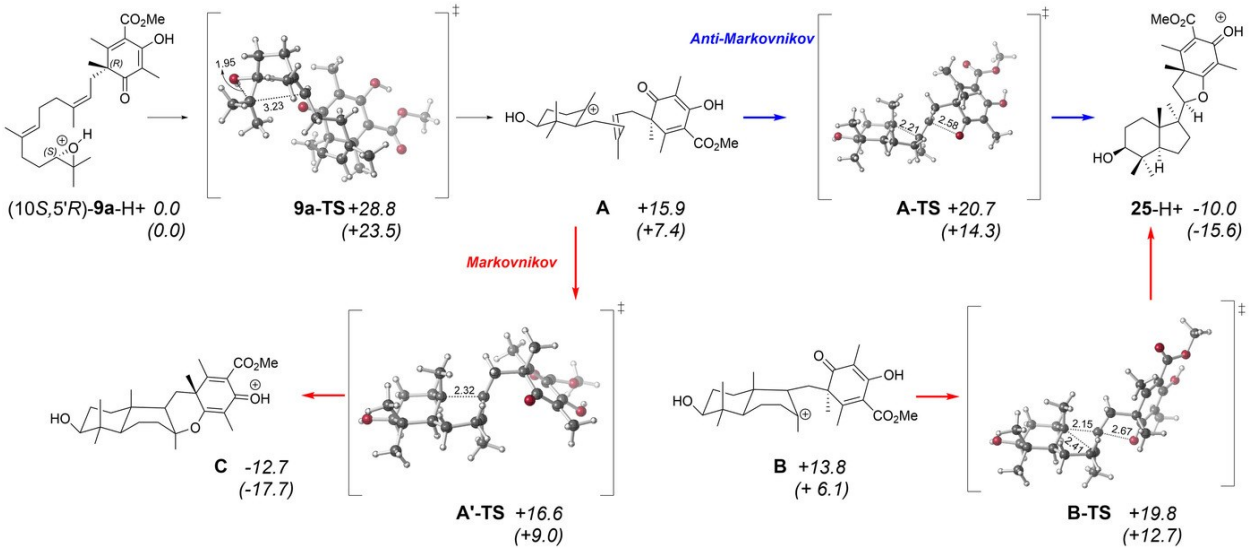

Figure 5.4. DFT calculations for the cyclization mechanism of (10S,5'R)-**9a** towards **25** by AndB. Two conformers of **A** were located, one connected to **9a-TS** and another connected to **A-TS**, which differ in energy by 0–3 kcal mol^{-1}, depending on the level of theory; see SI for details. Computed (B3LYP-D3(BJ)/6-31G(d,p)//B3LYP/6-31G(d,p) in black (top), CPCM(H_2O)-B3LYP-D3(BJ)/6-31G(d,p)//B3LYP/6-

31G(d,p) in parentheses (bottom)) relative free energies (kcal mol^{-1}, *italics*) for minima and transition state structures (TSSs) involved in formation of compound **25**. Bond distances are in Angstroms [Å].

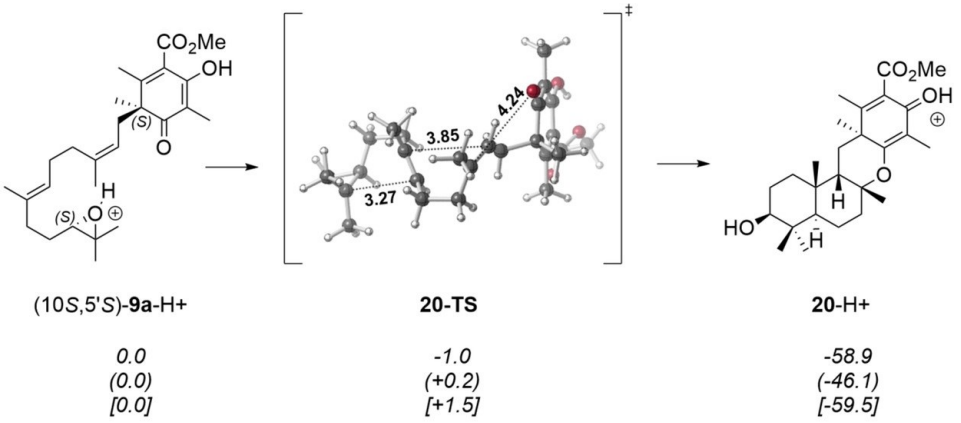

(10*S*,5'*S*)-**9a**-H+	**20-TS**	**20**-H+
0.0	*-1.0*	*-58.9*
(0.0)	*(+0.2)*	*(-46.1)*
[0.0]	*[+1.5]*	*[-59.5]*

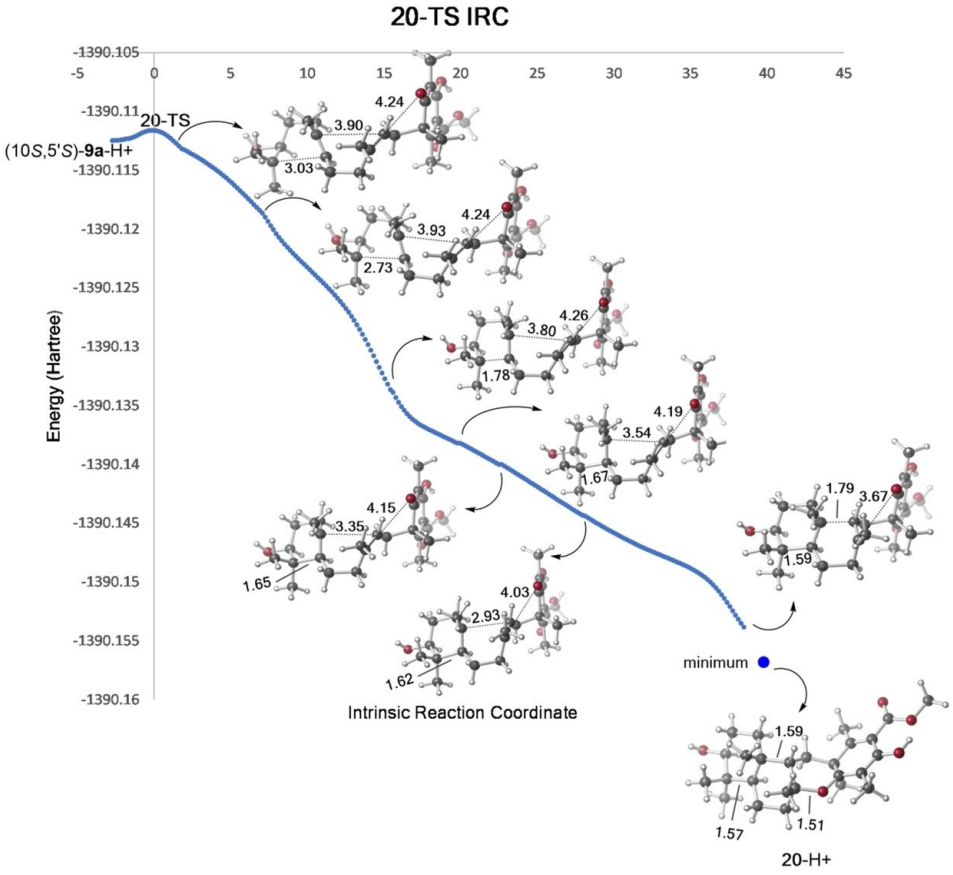

Figure 5.5. DFT calculations for the cyclization mechanism for the formation of **20**. Computed (B3LYP-D3(BJ)/6-31G(d,p)//B3LYP/6-31G(d,p) (on top), CPCM(H_2O)-B3LYP-D3(BJ)/6-31G(d,p)//B3LYP/6-

31G(d,p) (in parentheses) and MPW1PW91/6-31G(d,p)//B3LYP/6-31G(d,p) [in brackets]) relative free energies (kcalmol^{-1}, *italics*) for minima and transition state structures (TSSs) and IRC traces for the respective TSSs. Bond distances are in Angstroms [Å].

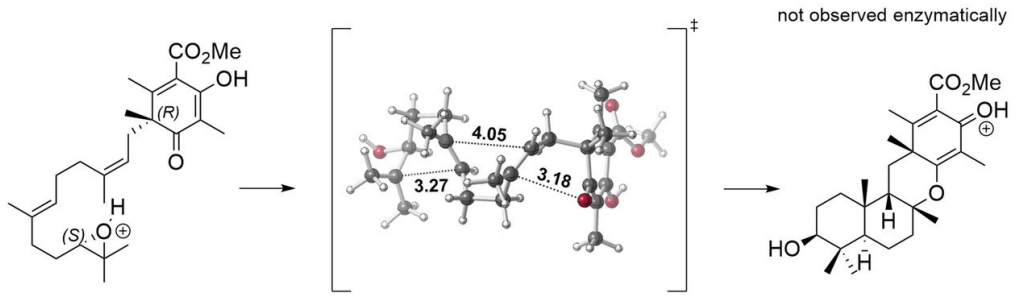

(10*S*,5'*R*)-**9a**-H+	**CC-TS**	**CC**-H+
0.0	*-0.8*	*-62.1*
(0.0)	*(+0.4)*	*(-49.0)*
[0.0]	*[+1.5]*	*[-63.7]*

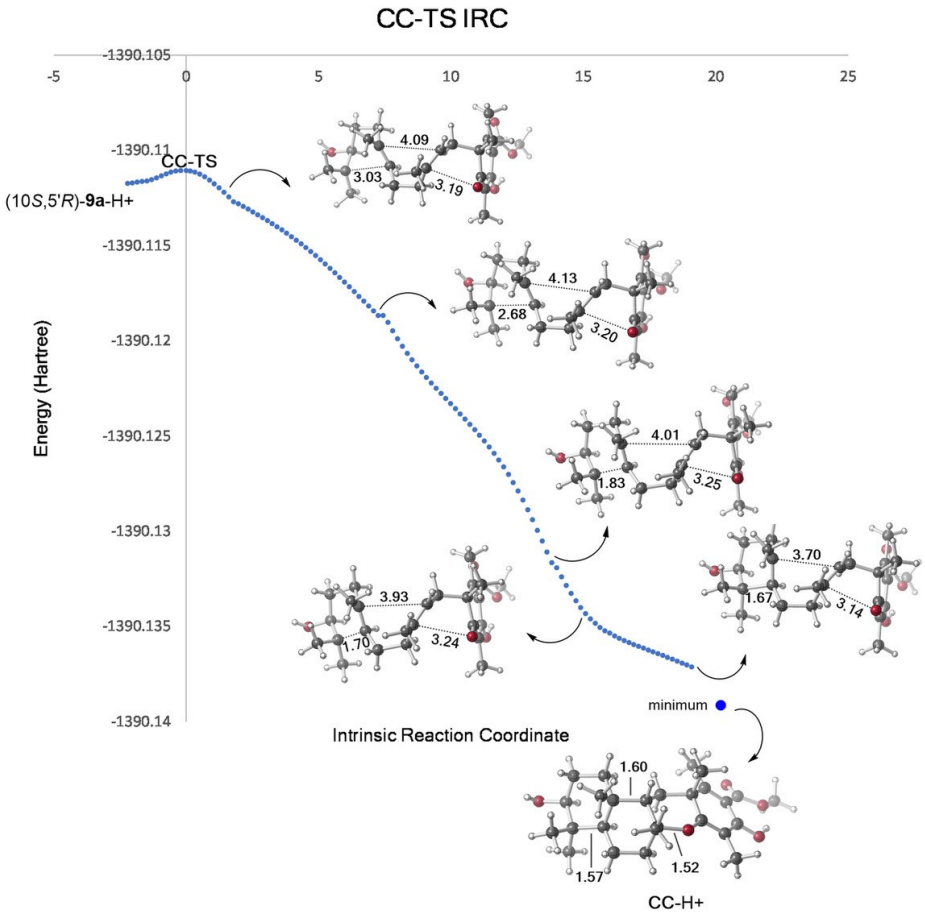

Figure 5.6. DFT calculations for the cyclization mechanism for the formation of **CC**. Computed (B3LYP-D3(BJ)/6-31G(d,p)//B3LYP/6-31G(d,p) (on top), CPCM(H_2O)-B3LYP-D3(BJ)/6-31G(d,p)//B3LYP/6-31G(d,p) (in parentheses) and MPW1PW91/6-31G(d,p)//B3LYP/6-31G(d,p) [in brackets]) relative free energies (kcalmol^{-1}, *italics*) for minima and transition state structures (TSSs) and IRC traces for the respective TSSs. Bond distances are in Angstroms [Å].

Mechanisms for formation of **20** (Figure 5.5) and **CC** (Figure 5.6) from protonated stereoisomers of **9a** were also subjected to computational analysis. For both reactions, we found highly asynchronous but concerted pathways in which no discrete carbocationic intermediates are formed. Similar concerted polycyclizations have been reported for related systems.[27] Both reactions also are predicted to be essentially barrierless once productive reactant conformations are attained, suggesting that preorganization controls which product is formed by a given enzyme. Conversion of **20**-H$^+$ to **19**-H$^+$ is predicted to be an endergonic process (Figure 5.7; neutral **19** is predicted to be several kcal mol^{-1} lower in energy than neutral **20**, however[11]), but an appropriately positioned base in a restricted enzyme active site could selectively deprotonate **19**-H$^+$. The barrier for the **20**-H$^+$ to **19**-H$^+$ interconversion is also less certain than others described above, since this reaction involves asynchronous bond-breaking, C–C bond rotation, and bond-making that leads to a "loose" transition state for which entropy and the effects of externally-imposed conformational constraints are difficult to estimate.

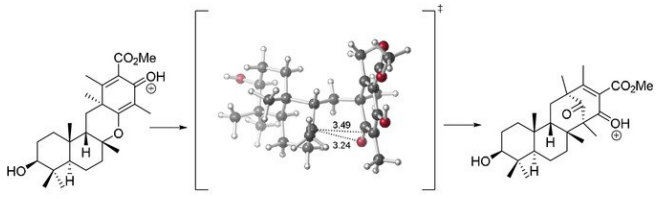

20-H+	**19-TS**	**19**-H+
0.0	*+25.3*	*+12.5*
(0.0)	*(+21.0)*	*(+8.4)*
[0.0]	*[+30.1]*	*[+15.2]*

Figure 5.7. DFT calculations for the interconversion of **20**-H$^+$ to **19**-H$^+$. Computed (B3LYP-D3(BJ)/6-31G(d,p)//B3LYP/6-31G(d,p) (on top), CPCM(H_2O)-B3LYP-D3(BJ)/6-31G(d,p)//B3LYP/6-31G(d,p) (in

parentheses) and MPW1PW91/6-31G(d,p)//B3LYP/6-31G(d,p) [in brackets]) relative free energies (kcalmol^{-1}, *italics*) for minima and transition state structures (TSSs). Bond distances are in Angstroms [Å].

5.3.6 Substrate Scope of Trt1, AdrI', PrhH, and NvfL

Another phylogenetic clade is formed by Trt1, AdrI, AdrI', AusL, and PrhH (Figure 5.2). These enzymes share the DMOA substrate (10R,5'R)-**7b**, but differ with regard to their product specificity. Trt1 catalyzes the formation of preterretonin (**27**) via a chair-chair-chair substrate conformation forming intermediary cation **26**, followed by Wagner–Meerwein rearrangement and a terminating deprotonation of H_a. AdrI shares the intermediary cation **26** and rearrangement but differs in the terminating deprotonation side (H_b) producing andrastin E (**28**). AusL and PrhH both catalyze the formation of protoaustinoid A (**29**) from **26** after direct deprotonation of H_c (Scheme 5.4A). NvfL from the novofumigatonin pathway utilizes a highly similar substrate as Trt1, AdrI, AusL, and PrhH, carrying a free carboxylic acid instead of the methyl ester in the DMOA-unit. The free acid is crucial for enzyme function and the protein catalyzes formation of a spiro-center (see SI for details).

Consistent with the obvious tight recognition of the polyketide portion necessary to achieve these sophisticated and distinct reactions, a comparable low promiscuity for this group of integral membrane-bound enzymes was observed. Whereas PrhH and NvfL did not accept any of the tested unnatural substrates, both Trt1 and AdrI' accepted (2Z,6E)-**9b**, with the natural 5'-substitution pattern in the polyketide portion (Table 5.1; see SI for details).

However, for these cases products were found to be too unstable for structure determination. To our surprise, we found that Trt1 as well as AdrI' were able to convert (10S)-**7a**, the native substrate with inverted stereochemistry with respect to the epoxide functionality. We succeeded in the isolation of the Trt1-mediated product from (10S,5'R)-**7a** and the structure was determined to be 3-*epi*-preterretonin (**30**). The formation of this product can be envisioned to occur via a boat-chair substrate conformation (Scheme 5.4B).[28]

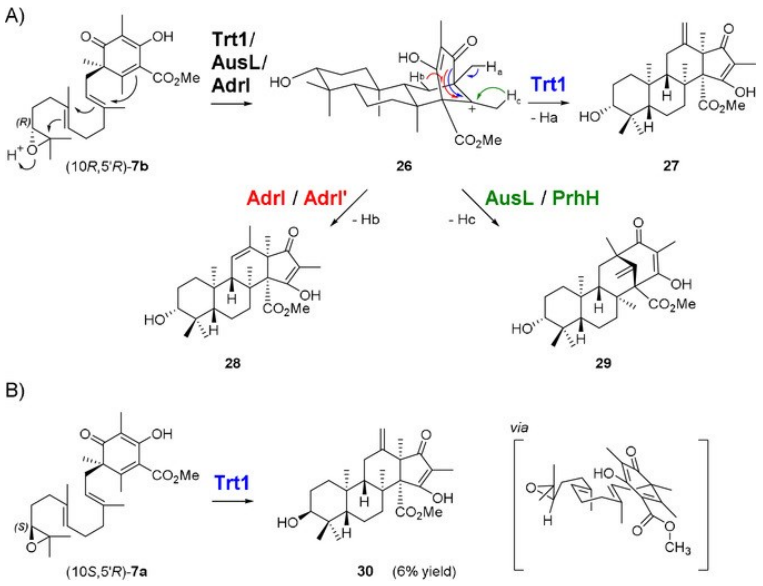

Scheme 5.4. A) Natural reaction of Trt1, AdrI/AdrI' and AusL/PrhH. B) Isolated meroterpenoids obtained from Trt1-mediated reactions with (10S,5'R)-**7a**.

5.3.7 Enzyme Kinetics of Trt1

To shed additional light on the substrate promiscuity of meroterpenoid cyclases, we were interested in the comparison of the K_M values of the natural substrate to unnatural substrate analogous. Synthetic (10R,5'R)-**7b** is the natural substrate of Trt1, which was also found to accept unnatural (10S,5'R)-**7a**, and (10R)-**9b**. Since Trt1 and other meroterpenoid cyclases cannot be purified, the integral membrane bound enzyme was used as a crude enzyme preparation. To ensure comparable reaction conditions, Trt1 was freshly prepared and used for all kinetic assays on the same day. The results revealed an apparent K_M value of 34 µM for the natural substrate **7b**, whereas a 3-fold (95 µM) and 5-fold (144 µM) higher value was found for substrates **7a** and **9b**, respectively. The V_{max} values were determined as 22 µM min^{-1}, 7 µM min^{-1} and 0.5 µM min^{-1}, for **7b**, **7a** and **9b**, respectively. These findings indicate that the unnatural substrates have a lower affinity for the enzyme, but the values are of the same order of magnitude and thus further demonstrate the promiscuity observed for this enzyme class.

5.4 Conclusion

In summary, we have demonstrated chemoenzymatic access to twelve complex, unnatural DMOA-derived meroterpenoids of which eight represent novel compounds by exploiting the surprisingly high promiscuity of fungal meroterpenoid cyclases.

Synthetic 3,5-dimethylorsellinic acid (DMOA)-containing substrates were prepared using de-aromative alkylation and evaluated against nine meroterpenoid cyclases. The results demonstrate tight recognition of the epoxide functionality by the cyclase panel, but tolerance towards the polyketide portion. The conserved cyclization mechanism initiated by epoxide protonation and rigid control of the substrate conformation in the cyclase active site cavity led to the formation of several variations of naturally occurring meroterpenoid scaffolds, as well as generation of a completely new scaffold, although the number of cyclization steps that are concatenated into concerted processes appears to be system-dependent. The challenging structure elucidation and determination of relative and absolute configurations for the obtained enzyme products was solved by combining 2D NMR data analysis with the recently developed method of crystalline-sponge-X-ray diffraction analysis. This method allowed us to access the crystallographic data of non-crystalline enzyme products such as **25** for unambiguous structure determination and thus represents a powerful technique in combination with second generation natural product discovery.

The knowledge obtained in this study can be used for the design of artificial pathways by recombining biosynthetic genes in a suitable heterologous production host. Whereas productive enzyme combinations with naturally occurring substrates such as **7a** and **7b** provide a straightforward access by reconstituting known pathways towards these substrates and interchanging the introduced meroterpenoid cyclase, access to (2Z,6E)-configured prenyl substrates require further engineering efforts, for example, by employing a known bacterial (2Z,6E)-selective FPP synthase from Mycobacterium[29] and optimization of downstream enzymes towards substrates like **9a** and **9b**. Furthermore, the new meroterpenoids obtained can be evaluated as substrates for downstream tailoring enzymes such as a-ketoglutarate-dependent dioxygenases. Since several protein crystal structures have been reported in recent years, protein

engineering by either rational strategies or directed evolution represents an exciting opportunity to create novel "unnatural" meroterpenoids with valuable biological properties.[30]

5.5 Acknowledgements

We thank the National Institutes of Health (R35 GM-118173, J.A.P., Jr.), a Grant-in-Aid for Scientific Research from the Ministry of Education, Culture, Sports, Science and Technology, Japan (JSPS KAKENHI Grant Number JP16H06443 and JP20H00490 to I.A.; JP19H05461 to M.F.), and the MEXT Nanotechnology Platform Program (Molecule and Material Synthesis) promoted at IMS for research funding. We also thank the Deutsche Forschungsgemeinschaft (DFG BA 6870/1-1) for a postdoctoral research fellowship to L.B. Computational work was supported by the National Science Foundation (CHE-1856416 and supercomputing resources from the XSEDE program via CHE-030089).

5.6 Supporting Information

Supporting information of this article can be found under: https://doi.org/10.1002/anie.202011171.

5.7 References

(1) (a) Cornforth, J. W. Terpenoid Biosynthesis. *Chem. Br.* **1968**, *4*, 102–106. (b) Geris, R.; Simpson, T. J. Meroterpenoids Produced by Fungi. *Nat. Prod. Rep.* **2009**, *26*, 1063–1094. (c) Kaysser, L.; Bernhardt, P.; Nam, S. J.; Loesgen, S.; Ruby, J. G.; Skewes-Cox, P.; Jensen, P. R.; Fenical, W.; Moore, B. S. Merochlorins A-D, Cyclic Meroterpenoid Antibiotics Biosynthesized in Divergent Pathways with Vanadium-Dependent Chloroperoxidases. *J. Am. Chem. Soc.* **2012**, *134*, 11988–11991. (d) Peng, X.; Qiu, M. Meroterpenoids from Ganoderma Species: A Review of Last Five Years. *Nat. Products Bioprospect.* **2018**, *8*, 137–149.

(2) (a) Ōmura, S.; Tomoda, H.; Kim, Y. K.; Nishida, H. Pyripyropenes, Highly Potent Inhibitors Of Acyl-Coa: Cholesterol Acyltransferase Produced By Aspergillus Fumigatus. *J. Antibiot.* **1993**, *46*, 1168–1169. (b) Tomoda, H.; Kim, Y. K.; Nishida, H.; Masuma, R.; Ōmura, S. Pyripyropenes, Novel Inhibitors Of Acyl-Coa: Cholesterol Acyltransferase Produced By Aspergillus Fumigatus I. Production, Isolation, And Biological Properties. *J. Antibiot.* **1994**, *47*, 148–153. (c) Das, A.; Davis, M. A.; Tomoda, H.; Ōmura, S.; Rudel, L. L. Identification of the Interaction Site within Acyl-CoA:Cholesterol Acyltransferase 2 for the Isoform-Specific Inhibitor Pyripyropene A. *J. Biol. Chem.* **2008**, *283*, 10453–10460.

(3) (a) Horikoshi, R.; Goto, K.; Mitomi, M.; Oyama, K.; Sunazuka, T.; Omura, S. Identification of Pyripyropene A as a Promising Insecticidal Compound in a Microbial Metabolite Screening. *J. Antibiot.* **2017**, *70*, 272–276. (b) Dieleman, C.; Knieriem, T.; Krapp, M.; Kierkus, P. C.; Xu, W.; Benton, K. Patent WO 2012/035010 A1, **2012**.

(4) (a) Sintchak, M. D.; Fleming, M. A.; Futer, O.; Raybuck, S. A.; Chambers, S. P.; Caron, P. R.; Murcko, M. A.; Wilson, K. P. Structure and Mechanism of Inosine Monophosphate Dehydrogenase

in Complex with the Immunosuppressant Mycophenolic Acid. *Cell* **1996**, *85*, 921–930. (b) Clutterbuck, P. W.; Oxford, A. E.; Raistrick, H.; Smith, G. Studies in the Biochemistry of Micro-Organisms: The Metabolic Products of the Penicillium Brevi-Compactum Series. *Biochem. J.* **1932**, *26*, 1441–1458. (c) Canonica, L.; Kroszczynski, W.; Ranzi, B. M.; Rindone, B.; Scolastico, C. The Biosynthesis of Mycophenolic Acid. *J. Chem. Soc. D* **1970**, *6*, 2639–2643. (d) Shaw, L. M.; Nowak, I. Mycophenolic Acid: Measurement and Relationship to Pharmacologic Effects. *Ther. Drug Monit.* **1995**, *17*, 685–689.

(5) (a) Ōmura, S.; Inokoshi, J.; Uchida, R.; Shiomi, K.; Masuma, R.; Kawakubo, T.; Tanaka, H.; Iwai, Y.; Kosemura, S.; Yamamura, S. Andrastins A-C, New Protein Farnesyltransferase Inhibitors Produced by Penicillium Sp. FO-3929. I. Producing Strain, Fermentation, Isolation, and Biological Activities. *J. Antibiot.* **1996**, *49*, 414–417. (b) Uchida, R.; Shiomi, K.; Inokoshi, J.; Sunazuka, T.; Tanaka, H.; Iwai, Y.; Takayanagi, H.; Omura, S. Andrastins A-C, New Protein Farnesyltransferase Inhibitors Produced by Penicillium Sp. FO-3929. II. Structure Elucidation and Biosynthesis. *J. Antibiot. (Tokyo).* **1996**, *49*, 418–424.

(6) Cueto, M.; MacMillan, J. B.; Jensen, P. R.; Fenical, W. Tropolactones A-D, Four Meroterpenoids from a Marine-Derived Fungus of the Genus Aspergillus. *Phytochemistry* **2006**, *67*, 1826–1831.

(7) Itoh, T.; Tokunaga, K.; Matsuda, Y.; Fujii, I.; Abe, I.; Ebizuka, Y.; Kushiro, T. Reconstitution of a Fungal Meroterpenoid Biosynthesis Reveals the Involvement of a Novel Family of Terpene Cyclases. *Nat. Chem.* **2010**, *2*, 858–864.

(8) (a) Matsuda, Y.; Abe, I. Biosynthesis of Fungal Meroterpenoids. *Nat. Prod. Rep.* **2016**, *33*, 26–53. (b) Barra, L.; Abe, I. Chemistry of Fungal Meroterpenoid Cyclases. *Nat. Prod. Rep.* **2021**, *38*, 566–585. (c) Matsuda, Y.; Awakawa, T.; Mori, T.; Abe, I. Unusual Chemistries in Fungal Meroterpenoid Biosynthesis. *Curr. Opin. Chem. Biol.* **2016**, *31*, 1–7.

(9) Rudolf, J. D.; Chang, C. Y. Terpene Synthases in Disguise: Enzymology, Structure, and Opportunities of Non-Canonical Terpene Synthases. *Nat. Prod. Rep.* **2020**, *37*, 425–463.

(10) (a) Young, C. A.; Bryant, M. K.; Christensen, M. J.; Tapper, B. A.; Bryan, G. T.; Scott, B. Molecular Cloning and Genetic Analysis of a Symbiosis-Expressed Gene Cluster for Lolitrem Biosynthesis from a Mutualistic Endophyte of Perennial Ryegrass. *Mol. Genet. Genomics* **2005**, *274*, 13–29. (b) Nicholson, M. J.; Koulman, A.; Monahan, B. J.; Pritchard, B. L.; Payne, G. A.; Scott, B. Identification of Two Aflatrem Biosynthesis Gene Loci in Aspergillus Flavus and Metabolic Engineering of Penicillium Paxilli to Elucidate Their Function. *Appl. Environ. Microbiol.* **2009**, *75*, 7469–7481. (c) Tagami, K.; Liu, C.; Minami, A.; Noike, M.; Isaka, T.; Fueki, S.; Shichijo, Y.; Toshima, H.; Gomi, K.; Dairi, T.; Oikawa, H. Reconstitution of Biosynthetic Machinery for Indole-Diterpene Paxilline in Aspergillus Oryzae. *J. Am. Chem. Soc.* **2013**, *135*, 1260–1263. (d) Kato, H.; Tsunematsu, Y.; Yamamoto, T.; Namiki, T.; Kishimoto, S.; Noguchi, H.; Watanabe, K. New Natural Products Isolated from Metarhizium Robertsii ARSEF 23 by Chemical Screening and Identification of the Gene Cluster through Engineered Biosynthesis in Aspergillus Nidulans A1145. *J. Antibiot.* **2016**, *69*, 561–566. (e) Yao, T.; Liu, J.; Liu, Z.; Li, T.; Li, H.; Che, Q.; Zhu, T.; Li, D.; Gu, Q.; Li, W. Genome Mining of Cyclodipeptide Synthases Unravels Unusual TRNA-Dependent Diketopiperazine-Terpene Biosynthetic Machinery. *Nat. Commun.* **2018**, *9*. (f) Tsukada, K.; Shinki, S.; Kaneko, A.; Murakami, K.; Irie, K.; Murai, M.; Miyoshi, H.; Dan, S.; Kawaji, K.; Hayashi, H.; Kodama, E. N.; Hori, A.; Salim, E.; Kuraishi, T.; Hirata, N.; Kanda, Y.; Asai, T. Synthetic Biology Based Construction of Biological Activity-Related Library of Fungal Decalin-Containing Diterpenoid Pyrones. *Nat. Commun.* **2020**, *11*. (g) Li, H.; Sun, Y.; Zhang, Q.; Zhu, Y.; Li, S. M.; Li, A.; Zhang, C. Elucidating the Cyclization Cascades in Xiamycin Biosynthesis by Substrate Synthesis and Enzyme Characterizations. *Org. Lett.* **2015**, *17*, 306–309. (h) Yaegashi, J.; Romsdahl, J.; Chiang, Y. M.; Wang, C. C. C. Genome Mining and Molecular Characterization of the Biosynthetic Gene Cluster of a Diterpenic Meroterpenoid, 15-Deoxyoxalicine B, in Penicillium Canescens. *Chem. Sci.* **2015**, *6*, 6537–6544.

(11) Powers, Z.; Scharf, A.; Cheng, A.; Yang, F.; Himmelbauer, M.; Mitsuhashi, T.; Barra, L.; Taniguchi, Y.; Kikuchi, T.; Fujita, M.; Abe, I.; Porco, J. A. Biomimetic Synthesis of Meroterpenoids by

Dearomatization-Driven Polycyclization. *Angew. Chem. Int. Ed.* **2019**, *58*, 16141–16146.

(12) Bai, T.; Quan, Z.; Zhai, R.; Awakawa, T.; Matsuda, Y.; Abe, I. Elucidation and Heterologous Reconstitution of Chrodrimanin B Biosynthesis. *Org. Lett.* **2018**, *20*, 7504–7508.

(13) (a) Matsuda, Y.; Wakimoto, T.; Mori, T.; Awakawa, T.; Abe, I. Complete Biosynthetic Pathway of Anditomin: Nature's Sophisticated Synthetic Route to a Complex Fungal Meroterpenoid. *J. Am. Chem. Soc.* **2014**, *136*, 15326–15336. (b) Nakashima, Y.; Mitsuhashi, T.; Matsuda, Y.; Senda, M.; Sato, H.; Yamazaki, M.; Uchiyama, M.; Senda, T.; Abe, I. Structural and Computational Bases for Dramatic Skeletal Rearrangement in Anditomin Biosynthesis. *J. Am. Chem. Soc.* **2018**, *140*, 9743–9750.

(14) (a) Matsuda, Y.; Awakawa, T.; Abe, I. Reconstituted Biosynthesis of Fungal Meroterpenoid Andrastin A. *Tetrahedron* **2013**, *69*, 8199–8204. (b) Matsuda, Y.; Quan, Z.; Mitsuhashi, T.; Li, C.; Abe, I. Cytochrome P450 for Citreohybridonol Synthesis: Oxidative Derivatization of the Andrastin Scaffold. *Org. Lett.* **2016**, *18*, 296–299.

(15) Matsuda, Y.; Bai, T.; Phippen, C. B. W.; Nødvig, C. S.; Kjærbølling, I.; Vesth, T. C.; Andersen, M. R.; Mortensen, U. H.; Gotfredsen, C. H.; Abe, I.; Larsen, T. O. Novofumigatonin Biosynthesis Involves a Non-Heme Iron-Dependent Endoperoxide Isomerase for Orthoester Formation. *Nat. Commun.* **2018**, *9,* 2587.

(16) (a) Matsuda, Y.; Iwabuchi, T.; Fujimoto, T.; Awakawa, T.; Nakashima, Y.; Mori, T.; Zhang, H.; Hayashi, F.; Abe, I. Discovery of Key Dioxygenases That Diverged the Paraherquonin and Acetoxydehydroaustin Pathways in Penicillium Brasilianum. *J. Am. Chem. Soc.* **2016**, *138*, 12671–12677. (b) Zhang, T.; Wan, J.; Zhan, Z.; Bai, J.; Liu, B.; Hu, Y. Activation of an Unconventional Meroterpenoid Gene Cluster in Neosartorya Glabra Leads to the Production of New Berkeleyacetals. *Acta Pharm. Sin. B* **2018**, *8*, 478–487.

(17) (a) Itoh, T.; Tokunaga, K.; Radhakrishnan, E. K.; Fujii, I.; Abe, I.; Ebizuka, Y.; Kushiro, T. Identification of a Key Prenyltransferase Involved in Biosynthesis of the Most Abundant Fungal Meroterpenoids Derived from 3,5-Dimethylorsellinic Acid. *ChemBioChem* **2012**, *13*, 1132–1135. (b) Matsuda, Y.; Awakawa, T.; Itoh, T.; Wakimoto, T.; Kushiro, T.; Fujii, I.; Ebizuka, Y.; Abe, I. Terretonin Biosynthesis Requires Methylation as Essential Step for Cyclization. *ChemBioChem* **2012**, *13*, 1738–1741. (c) Guo, C. J.; Knox, B. P.; Chiang, Y. M.; Lo, H. C.; Sanchez, J. F.; Lee, K. H.; Oakley, B. R.; Bruno, K. S.; Wang, C. C. C. Molecular Genetic Characterization of a Cluster in A. Terreus for Biosynthesis of the Meroterpenoid Terretonin. *Org. Lett.* **2012**, *14*, 5684–5687. (d) Matsuda, Y.; Iwabuchi, T.; Wakimoto, T.; Awakawa, T.; Abe, I. Uncovering the Unusual D-Ring Construction in Terretonin Biosynthesis by Collaboration of a Multifunctional Cytochrome P450 and a Unique Isomerase. *J. Am. Chem. Soc.* **2015**, *137*, 3393–3401.

(18) (a) Araki, Y.; Awakawa, T.; Matsuzaki, M.; Cho, R.; Matsuda, Y.; Hoshino, S.; Shinohara, Y.; Yamamoto, M.; Kido, Y.; Inaoka, D. K.; Nagamune, K.; Ito, K.; Abe, I.; Kita, K. Complete Biosynthetic Pathways of Ascofuranone and Ascochlorin in Acremonium Egyptiacum. *Proc. Natl. Acad. Sci. USA* **2019**, *116*, 8269–8274. (b) Quan, Z.; Awakawa, T.; Wang, D.; Hu, Y.; Abe, I. Multidomain P450 Epoxidase and a Terpene Cyclase from the Ascochlorin Biosynthetic Pathway in Fusarium Sp. *Org. Lett.* **2019**, *21*, 2330–2334.

(19) Tang, M. C.; Cui, X.; He, X.; Ding, Z.; Zhu, T.; Tang, Y.; Li, D. Late-Stage Terpene Cyclization by an Integral Membrane Cyclase in the Biosynthesis of Isoprenoid Epoxycyclohexenone Natural Products. *Org. Lett.* **2017**, *19*, 5376–5379.

(20) Qi, C.; Bao, J.; Wang, J.; Zhu, H.; Xue, Y.; Wang, X.; Li, H.; Sun, W.; Gao, W.; Lai, Y.; Chen, J. G.; Zhang, Y. Asperterpenes A and B, Two Unprecedented Meroterpenoids from Aspergillus Terreus with BACE1 Inhibitory Activities. *Chem. Sci.* **2016**, *7*, 6563–6572.

(21) (a) Inokuma, Y.; Yoshioka, S.; Ariyoshi, J.; Arai, T.; Hitora, Y.; Takada, K.; Matsunaga, S.; Rissanen, K.; Fujita, M. X-Ray Analysis on the Nanogram to Microgram Scale Using Porous Complexes. *Nature* **2013**, *495*, 461–466. (b) Hoshino, M.; Khutia, A.; Xing, H.; Inokuma, Y.; Fujita, M. The Crystalline Sponge Method Updated. *IUCrJ* **2016**, *3*, 139–151.

(22) Yamazaki, H.; Nakayama, W.; Takahashi, O.; Kirikoshi, R.; Izumikawa, Y.; Iwasaki, K.; Toraiwa,

K.; Ukai, K.; Rotinsulu, H.; Wewengkang, D. S.; Sumilat, D. A.; Mangindaan, R. E. P.; Namikoshi, M. Verruculides A and B, Two New Protein Tyrosine Phosphatase 1B Inhibitors from an Indonesian Ascidian-Derived Penicillium Verruculosum. *Bioorg. Med. Chem. Lett.* **2015**, *25*, 3087–3090.

(23) (a) Miehlich, B.; Savin, A.; Stoll, H.; Preuss, H. Results Obtained with the Correlation Energy Density Functionals of Becke and Lee, Yang and Parr. *Chem. Phys. Lett.* **1989**, *157*, 200–206. (b) Lee, C.; Yang, W.; Parr, R. G. Development of the Colle-Salvetti Correlation-Energy Formula into a Functional of the Electron Density. *Phys. Rev. B* **1988**, *37*, 785–789. (c) Becke, A. D. Density-functional Thermochemistry. III. The Role of Exact Exchange. *J. Chem. Phys.* **1993**, *98*, 5648–5652. (d) Grimme, S.; Ehrlich, S.; Goerigk, L. Effect of the Damping Function in Dispersion Corrected Density Functional Theory. *J. Comput. Chem.* **2011**, *32*, 1456–1465. (e) Takano, Y.; Houk, K. N. Benchmarking the Conductor-like Polarizable Continuum Model (CPCM) for Aqueous Solvation Free Energies of Neutral and Ionic Organic Molecules. *J. Chem. Theory Comput.* **2005**, *1*, 70–77.

(24) We benchmarked our system using a variety of methods: CPCM(DCM)-B3LYP-D3(BJ)/6-31G(d,p)//B3LYP/6-31G(d,p), CPCM(MEOH)-B3LYP-D3(BJ)/6-31G(d,p)//B3LYP/6-31G-(d,p), mPW1PW91/6-31G(d,p)//B3LYP/6-31G(d,p) and CPCM-(MEOH)- mPW1PW91/6-31G(d,p)//B3LYP/6-31G(d,p). See SI for details. Matsuda, S. P. T.; Wilson, W. K.; Xiong, Q. Mechanistic Insights into Triterpene Synthesis from Quantum Mechanical Calculations. Detection of Systematic Errors in B3LYP Cyclization Energies. *Org. Biomol. Chem.* **2006**, *4*, 530–543.

(25) **9a** is the conformer obtained from reverse **9a-TS** intrinsic reaction coordinate (IRC) analysis. **9a-TS** forward IRC product undergoes a conformational change to form **A** which is the reverse IRC product of **A-TS**. See SI for details. (a) Gonzalez, C.; Schlegel, H. B. Reaction Path Following in Mass-Weighted Internal Coordinates. *J. Phys. Chem.* **1990**, *94*, 5523–5527. (b) Fukui, K. The Path of Chemical Reactions - the IRC Approach. *Acc. Chem. Res.* **1981**, *14*, 363–368. (c) Maeda, S.; Harabuchi, Y.; Ono, Y.; Taketsugu, T.; Morokuma, K. Intrinsic Reaction Coordinate: Calculation, Bifurcation, and Automated Search. *Int. J. Quantum Chem.* **2015**, *115*, 258–269.

(26) Wang, S. C.; Tantillo, D. J. Theoretical Studies on Synthetic and Biosynthetic Oxidopyrylium-Alkene Cycloadditions: Pericyclic Pathways to Intricarene. *J. Org. Chem.* **2008**, *73*, 1516–1523.

(27) (a) Tantillo, D. J. Recent Excursions to the Borderlands between the Realms of Concerted and Stepwise: Carbocation Cascades in Natural Products Biosynthesis. *J. Phys. Org. Chem.* **2008**, *21*, 561–570. (b) Smentek, L.; Hess, B. A. Compelling Computational Evidence for the Concerted Cyclization of the ABC Rings of Hopene from Protonated Squalene. *J. Am. Chem. Soc.* **2010**, *132*, 17111–17117. (c) McCulley, C. H.; Geier, M. J.; Hudson, B. M.; Gagné, M. R.; Tantillo, D. J. Biomimetic Platinum-Promoted Polyene Polycyclizations: Influence of Alkene Substitution and Pre-Cyclization Conformations. *J. Am. Chem. Soc.* **2017**, *139*, 11158–11164.

(28) Abe, I.; Rohmer, M. Enzymic Cyclization of 2,3-Dihydrosqualene and Squalene 2,3-Epoxide by Squalene Cyclases: From Pentacyclic to Tetracyclic Triterpenes. *J. Chem. Soc. Perkin Trans. 1* **1994**, 783–791.

(29) (a) Schulbach, M. C.; Brennan, P. J.; Crick, D. C. Identification of a Short (C15) Chain Z-Isoprenyl Diphosphate Synthase and a Homologous Long (C50) Chain Isoprenyl Diphosphate Synthase in Mycobacterium Tuberculosis. *J. Biol. Chem.* **2000**, *275*, 22876–22881. (b) Schulbach, M. C.; Mahapatra, S.; Macchia, M.; Barontini, S.; Papi, C.; Minutolo, F.; Bertini, S.; Brennan, P. J.; Crick, D. C. Purification, Enzymatic Characterization, and Inhibition of the Z-Farnesyl Diphosphate Synthase from Mycobacterium Tuberculosis. *J. Biol. Chem.* **2001**, *276*, 11624–11630.

(30) (a) Nakashima, Y.; Mori, T.; Nakamura, H.; Awakawa, T.; Hoshino, S.; Senda, M.; Senda, T.; Abe, I. Structure Function and Engineering of Multifunctional Non-Heme Iron Dependent Oxygenases in Fungal Meroterpenoid Biosynthesis. *Nat. Commun.* **2018**, *9,* 104–114. (b) Nakamura, H.; Matsuda, Y.; Abe, I. Unique Chemistry of Non-Heme Iron Enzymes in Fungal Biosynthetic Pathways. *Nat. Prod. Rep.* **2018**, *35*, 633–645.